PYROCHLORE SPIN ICE $DY_2TI_2O_7$: INVESTIGATING A PLATFORM FOR MAGNETIC MONOPOLAR QUASIPARTICLES

BY

KENNETH WILLIAM SCHLAX

DISSERTATION

Submitted in partial fulfillment of the requirements
for the degree of Doctor of Philosophy in Physics
in the Graduate College of the
University of Illinois at Urbana-Champaign, 2019

Urbana, Illinois

Doctoral Committee:

Professor Gregory MacDougall, Chair
Professor Dale Van Harlingen, Director of Research
Professor Karin Dahmen
Professor Virginia Lorenz

Abstract

Spin ice is a frustrated magnetic state exhibiting a residual entropy in the magnetic degrees of freedom down to the lowest experimentally measured temperatures. The pyrochlore oxide dysprosium titanate ($Dy_2Ti_2O_7$) supports a spin ice state on its tetrahedral sublattice of dysprosium spins at low temperatures. Such tetrahedral arrangements of Ising spins yield have drawn interest from the scientific community not only for its unusual persistent low temperature frustrated state but also for exotic magnetic ordered states and transitions when oriented along different crystal axes in an external magnetic field, including the transition from a three-dimensional spin ice state to a two-dimensional kagome ice state. More recently, interest has expanded upon the proposal that $Dy_2Ti_2O_7$ supports emergent fractionalized magnetic monopole quasiparticles as a consequence of defects in the spin ice symmetry.

This work sought to probe the existence, statics, and dynamics of these monopole quasiparticles, and what factors affect their density and mobility. At the beginning of study, there were two significant confounding issues in the field of study of monopole quasiparticles: competing effects of oxygen vacancy defect sites in bulk crystal, and effects of strains and surfaces in real spin ice systems. Investigation of these issues began with collaborating on the growth of $Dy_2Ti_2O_7$ crystals in a range of oxygen environments, and of $Dy_2Ti_2O_7$ thin films of varying thickness in a pulsed laser deposition system. After determining spin ice quality, a supeconducting quantum interference device ("SQUID")-based magnetometer in a dilution refrigerator was used to search for signatures of monopole excitations in spin ice.

From this work, structural, thermal, and magnetic trends were measured in spin ice

crystals grown under varying oxygen conditions, and the large effect of oxygen content on the statistical mechanics and electromagnetism of spin ice has been demonstrated. The structural and thermal trends of varying thicknesses of thin films of spin ice have been probed by similar methods to demonstrate the impact of reduced dimensionality on a three-dimensional magnetically ordered state. Finally, an experimental probe of the monopolar quasiparticle behavior using SQUID magnetometry has been created.

To Laura.

Acknowledgments

The "Urbana style" of doing physics is first and foremost collaborative and inquisitive. Prof. Nigel Goldenfeld may have said it best as "not forgetting the science, nor forgetting to have fun."

I feel that I took full advantage of all the benefits of the "Urbana style" of doing physics during the pursuit of my doctorate. Thanks to the tremendously driven and insightful people in the Physics Department at the University of Illinois, Urbana-Champaign, not only was I able to be immersed in the dynamic environment of pushing the frontiers of science, but I had fun doing it!

In particular, I would like to acknowledge my advisor, Prof. Dale Van Harlingen, who taught me how to do science effectively and efficiently and how to work together towards scientific goals. He was never without a new physics question, nor an idea for an experiment to answer it. The DVH group members similarly were universally helpful and encouraging. I would like to thank all the postdocs: Guang Yue, Aaron Finck, Cihan Kurter, Martin Stehno, and Vlad Orlyanchik for their leadership and resourcefulness. To all my fellow grad students in the DVH lab, David Hamilton, Erik Huemiller, Adam Weis, Chris Nugroho, Juan Atkinson, Gilbert Arias, and Jessica Montone, thank you for all the late nights, the hard work, the good spirits, the interesting problems, the clever solutions, and the great times we had inside and outside of lab. Also, I appreciate the opportunity I had to mentor and work with a group of amazing undergraduate researchers, Kyle Sendgikoski, Laura Troyer, and David Friedman, who all helped to grow, characterize, and analyze the thin films in this project. Thank you for all your efforts, questions, and time. Finally in the DVH lab, I must

acknowledge Tony Banks, whose boundless knowledge and technical expertise could only be matched by his enthusiasm for research.

This research would not have been possible without the generous efforts of our collaborators. First, I would like to thank Prof. Greg MacDougall, in whose group postdoc Alex Thaler grew, oriented, and cut the range of bulk crystals used in our experiments, and undergraduate researcher Suchisman Gangopadhyay helped analyze the structural trends of the bulk crystals. Gregs enthusiasm and expertise made sure that the work got done and done well. Second, I would like to recognize the efforts of my preliminary exam and thesis defense committee members Prof. Karin Dahmen and Prof. Virginia Lorenz, whose feedback and inquiry helped ensure that both I and this work were headed the right way. Finally, I would like to acknowledge the inspiration for and benefactor of this work, Prof. Peter Schiffer, and his postdocs Jarrett Moyer and Joseph Sklenar, as well as graduate students Brian Le and Maria Matthews, whose experience and openness ensured I had an outlet to tackle even the toughest problems.

The "Urbana style" of doing physics would not happen without a wonderful place to do physics. I thank the MRL and Physics Staff, including Mauro Sardela, Ernest Northen, James Lee, Tim Spila, and Scott MacLaren, whose generosity in sharing their time and talents greatly expanded our range of research.

And finally, to all the friends and family who supported me along this journey: To my brilliant, unique, and beautiful wife Laura, for all your advice and encouragement since well before this doctorate started, and for all the excitement to come. To my mom and dad, Donald and Jeanne Schlax, whose endless support I could always rely on. To Nan and Pop, Florence and Henry Hertwig, who always believed in their "Kenny Boy". To Grandma and Grandpa, Leone and William Schlax, and all the Schlax side of the family, thank you for all your enthusiasm. To my brothers Chris, Kevin, and Steven, my in-laws Joe and Josie Divel, and my sisters-in-law Sarah and Mary, thanks for all the ongoing fun and adventures!

A long overdue thanks to all the teachers, professors, and mentors who helped me to

even get to the start of this process, especially my undergraduate advisor Prof. Umesh Garg at Notre Dame and my summer advisor at Argonne National Lab, Dr. Bingxin Yang.

To all the Wild Bohrs Physics Softball Team: Kristen, Zach, Andrew, Barbara, Adi, Rob, Patrick, Michelle, John, Billy, and the rest: Go Bohrs! And to the rest of my friends and colleagues in Champaign and Urbana - Thank you all!

This work was supported in part by the National Science Foundation under grant DMR-1341793 and was carried out in part in the Materials Research Laboratory Central Research Facilities, University of Illinois.

Table of Contents

List of Tables

List of Figures

List of Abbreviations

DSIM	Dipolar Spin Ice Model
DTO	Dysprosium Titanate
PLD	Pulsed Laser Deposition
SQUID	Superconducting Quantum Interference Device
YSZ	Yttria-stabilized Zirconia
PID	Proportional, Integral, Derivative (Control)
XRD	X-ray Diffraction
XRR	X-ray Reflectivity
XRF	X-ray Fluorescence
JJ	Josephson Junction

List of Symbols

μ_B	Bohr Magneton
ρ	Monopole Density
ϕ	Superconducting phase
C	Heat Capacity
S	Entropy
H	Hamiltonian
J_{ex}^{nn}	Nearest neighbor exchange interaction strength
τ	Characteristic time scale
β	1/T, Inverse Temperature

Chapter 1

Introduction

This thesis focuses on three main experimental areas: various oxygen growth condition effects on single crystal spin ice pyrochlores, dimensionality-reduction effects on the 3-dimensional spin ice state in pyrochlore thin films, and SQUID probes of monopole quasiparticles in spin ice pyrochlores. These areas emerged out of a combination of open questions in the field and our capabilities. The open questions in the field will be described below, and our capabilities will be introduced in detail after the next chapter containing the theoretical foundation for spin ice research. Our capabilities arose out of the experience and resources of three research groups here at UIUC: Professor Peter Schiffer's group, with a strong background in spin ice methodology and characterization; Professor Gregory MacDougall's group with a strong background in crystal growth and characterization; and Professor Dale Van Harlingen's group, with a strong background in SQUID measurements and thin film growth. Results from the three experimental areas will be presented and discussed in the three chapters following the explanation of capabilities, and finally a concluding chapter will describe the impact and outlook of this work.

1.1 Motivation and Questions

One mantra of condensed matter physics, coined by P.W. Anderson, is "more is different". [1] Condensed matter physics seeks to discover how the laws of physics in collections of particles change, behaving as if they have properties of an entirely different particle altogether. [2] These 'quasi-particle' excitations can transform fundamental properties and symmetries of

the constituent particles into behavior of unlike systems. For a well-studied example, two fermionic electrons enter into a bosonic bound state, called a Cooper pair, thus avoiding Pauli exclusion and permitting any number of quasi-particle pairs into the same state, the result of which is Type I superconductivity. [3] A more recent example of a quasi-particle investigation is the evolving study of Majorana fermions as a fractionalized electron state bound to a vortex in topological insulators. [4] These auto-anti-quasi-particles possess non-Abelian exchange statistics, and have not yet been found as a free particle in the universe. [5, 6]

The spin ice state is a geometrically frustrated magnetic state emerging from anti-ferromagnetic order on a tetrahedral lattice. Rare earth pyrochlores with large local easy-axis anisotropy on the magnetic sublattice were discovered to exhibit ice-type behavior at low temperatures and low magnetic fields in the 1990s through neutron scattering measurements [7], and soon afterwards using heat capacity measurements. [8] Later, in 2008 [9], these spin ice materials were theorized to support quasi-particle excitations resembling Dirac monopoles arising out of defects in the spin ice pattern. The existence, behavior, and dynamics of these excitations has since been an open area of research, leading to questions specifically about the effects of stoichiometric and structural defects [10], anomalous spin density and mobility slowing or pinning [11], and spin statistics under applied fields and temperatures [12].

1.2 State of the Field

To clarify the above, and to get a sense of how the following research fits into the broader effort to understand spin ice materials and emergent monopole behavior, it is good to understand the preexisting literature and questions, as well as the major developments made alongside our own research.

The field of spin ice experiments got its start with neutron scattering studies [7], and with heat capacity measurements made by A.P. Ramirez, et al. [8, 13] which indicated that

down to lowest measured temperatures, a residual Pauling entropy associated with ice-like configurations persisted. The nature of the lowest temperature states of the measured pyrochlores, originally Holmium Titanate [14], and later Dysprosium Titanate [8] as classical pyrochlore spin ices, became and is still an active area of research. [15] This polycrystalline powder measurement was supplemented by single crystal heat capacity measurements [16], both of which further explored the changes in behavior as a function of temperature and applied field, discovering for example the plateau structure of the magnetic moment of spin ice under an applied [111] direction field [17]. In the ensuing decade or so, theorists such as Bramwell [18] and Gingras [19] advanced the spin ice state as the explanation for the residual entropy and other behavior seen in these magnetic pyrochlores.

In 2008, Castelnovo [9] proposed that the spin ice state could support an effective fractionalized magnetic monopole quasiparticle on the pyrochlore lattice. This theory of fractionalized magnetic charges generated tremendous interest as a platform for understanding and exploiting an electrodynamics with magnetic monopoles connected by Dirac strings, all within the context of treating each set of four spins as a single "north" or "south" charge. So, although the magnetic dipole is fractionalized effectively, the quasiparticle nature of these monopolar excitations means that four spins collectively act as just one quasi-monopole, as shown in Figure 2.6.

The first measurements of this behavior was done via neutron scattering to probe directly the Dirac strings [20]. These measurements relied on pinch point signatures in the neutron scattering to directly reveal the atomic behavior and the behavior of spin ice defects. Once seen via neutron scattering, it remained a question if the excitation would retain the statics and dynamics associated with the thermal and magnetic properties of a monopole charge.

Other proposals, as will be described below in the section on SQUIDs, sought to follow the approaches of searches for real monopole charges, such as that of Blas Cabrera in 1982 [21], who claimed to have discovered a free monopole just by monitoring a sensitive flux magnetometer and waiting for a monopole to pass through it. Such investigations for real

monopoles are still ongoing today, with the MoEDAL experiment at the LHC [22], for example. These experiments began earlier, and have been developed in parallel to the field of spin ice, and so often researchers interested in real monopoles will branch out to effective monopoles found in spin ices crystals in condensed matter systems (as in this work) or in ultracold atoms in laser and Bose Einstein condensate systems [23, 24].

As the field has progressed further, the original ground state interests and the monopole investigations have encountered the same obstacles, arising from two areas: first, the dynamics of the spins exhibit a dramatic slowing, or "freezing out", as the system is cooled below 1K [11]; and second, from uncertainty as to the effect of non-idealities within the crystal: from things as simple as the effect of boundaries on the spin ice state [25] or dimensionality constraints in thin films [26] to more complicated matters such as the effect of crystalline defects on relaxation time [10] and pair pinning and generation [27].

Some attempts to overcome these obstacles have included long time thermal measurements [28] and clever magnetic avalanche behavior [12], both of which met with some success, but other investigations such as a long time neutron scattering measurement [29] and variations on the nuclear isotopes of Dysprosium have failed to indicate the origin of dynamical slowing. Commonly [30], researchers have attributed this behavior to oxygen off-stoichiometry, with only a brief and a related effort in Yttrium Titanate yielding some promising clues [10]. This unresolved open question formed the basis of our first area of experimental interest.

Several parallel efforts have arisen in the field of spin ice as well, namely: artificial spin ice [31], quantum spin ice [32, 33], and thin film spin ice [34, 35] . The latter of these will be explored in depth in this thesis as a platform for investigating monopoles in spin ice as our second area of experimental interest. At the start of our research, two papers [34, 35] had emerged providing competing pictures of the behavior of thin film spin ice, and each had different answers as to how the reduced dimensionality and increased strain of thin film pyrochlores affect the spin ice state. We undertook to resolve this endeavor, and while other

groups has begun looking at similar systematics (e.g. [36]), this question was otherwise only addressed in this work.

Other views of spin ice have emerged as well. Experiments done by J.C. Seamus Davis at Cornell using toroids of spin ice material [37] have probed the dynamics of magnetism in spin ice and concluded that the entrance into the spin ice state resembles more a transition into a supercooled spin liquid. A prominent muon spin resonance probe of monopolar dynamics [38] was largely refuted when it was revealed that the signatures seen in the sample could also be explained by signatures arising from well-understood behavior in the substrate [39].

At this point it is also worth mentioning parallel efforts in two very closely related fields: artifical spin ice and quantum spin ice. Artificial spin ices are arrays of nanomagnets arranged such that the ice rules are obey by configurations of macroscopic dipolar magnetic islands. These engineered systems can be probed and controlled at room temperature and under accessible magnetic fields. [31] Quantum spin ices are materials, such as $Pr_2Zr_2O_7$ as claimed by [32] whose monopolar excitations ("spin flips") can tunnel quantum mechanically, as opposed to the "classical" spin ice where defects act diffusively and flip only via thermal or applied field processes.

Finally, looking ahead to future endeavors in the field of spin ice, the monopole probe approach described earlier has been broadened with the addition of diamond nitrogen vacancy probes, from the Amir Yacoby group at Harvard [40], and scanning SQUID microscopes, from the K. Moler group at Stanford [41].

1.3 Guide to the Thesis

This thesis will follow the organic structure of the research conducted. The initial goal was to answer the questions above by using SQUID magnetometry to measure the dynamics and magnetic effects of the monopole quasiparticles under experimental conditions designed to elucidate the monopolar contribution from other magnetic effects. When this work in the

field of spin ice research began, there existed several open questions, specifically about the effect of oxygen vacancies in the spin ice lattice on measurement time scales and monopole dynamics, as well as conflicting reports about the persistence of the spin ice state in thin films. Along the way, as appropriate experiments to run for the SQUID magnetometry measurements were examined, these existing obstacles and questions in the field could also be overcome and resolved. To that end, a range of oxygen-grown crystals as well as thin films were characterized to probe dimensional effects and also to measure a known volume of spin ice free from screening effects seen in the bulk. This thesis will review those significant results we obtained along the way, before looking at the status and prospects for the SQUID magnetometry experiment designs described. Careful measurement of precise magnetic flux and flux noise using the SQUID can give us the necessary tools to undertake a unique view of the creation, annihilation, dynamics, and emergence of the monopole-like excitations in spin ice systems, and we look to resolve several open questions, including: How can we correlate the different thermal and magnetic properties of monopole-like excitations, to pin down their exact nature and confirm the monopole quasiparticle theory? How do the excitations move and interact with the spin ice magnetic landscape? and How does crystal quality or reduced dimensionality affect the existence and dynamics of monopole quasiparticles?

The thesis will begin with a review of the theories behind the spin ice state and emergent monopole quasiparticles in the **Theory** chapter. Methodology behind the growth of bulk crystals and thin films, characterization procedures, and SQUID magnetometry experimental design will be described in **Techniques and Equipment**. The systematics seen in structural, thermal, and magnetic probes of the series of oxygen-grown bulk crystals will be described in **Crystalline $Dy_2Ti_2O_7$ Oxygen Effects**. Thin film trends and results will be summarized in **Thin Film $Dy_2Ti_2O_7$**. Finally, efforts to answer the above questions using SQUID magnetometry will be explained in **Superconducting Quantum Interference Device Magnetometry**.

Chapter 2

Theory

The theoretical background will introduce essential components of magnetism and frustration, and then show how these can be combined in the rare earth pyrochlore Dysprosium Titanate to support a spin ice state with Ising spins along the center-crossing axes on a tetrahedral lattice. The dipolar spin ice model (DSIM) predicts spin-flip defects to yield pairs of fractionalized magnetic monopole quasiparticles, whose dynamics in a two-component charged fluid are briefly reviewed, before a couple of notes on practical considerations are presented.

2.1 Magnetism and Magnetic Charges

In 1931 [42], Paul Dirac showed that electric charge must be quantized if even one magnetic monopole particle exists. To date, this statement has been supported extensively by measurements demonstrating the quantization of electric charge [43, 44], yet the magnetic monopole(s) remain(s) unobserved, despite unverified claims [21] and extensive searches [22].

In a system with magnetic monopolar charges, Maxwell's equations can be re-written to include a magnetic charge q_m analogously to the usual electronic charge q. Relativistic and quantum mechanical electromagnetic equations similarly expand upon the consideration of the existence of a magnetic charge, and so if such a charge or its analogue were to be found, we could attempt to search for it in ways that similarly measure electronic charges, including the Hall effect [45].

In all known materials, however, magnetism arises from two sources: spins and mov-

ing electric charges. [46] These both result in dipole magnetic fields, and so all magnetic landscapes are built from these components.

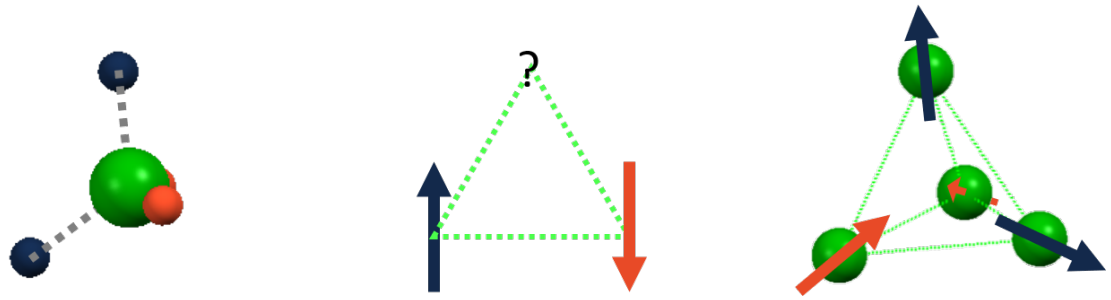

Figure 2.1: A geometrically frustrated magnetic state arises when the arrangement of spins in a crystal lattice inhibits classical ground state ordering. In the two-dimensional triangular antiferromagnetic Ising spin example, depicted at center, adjacent spins will anti-align, but a third such spin equidistant between the other two has no preferred direction, and so a residual degree of freedom persists. In the three-dimensional tetrahedral case, at right, Ising spins constrained to point either towards or away from the center minimize energy in a two-in, two-out pattern. However, because any two can point in or out locally, there remains a similar degree of freedom. The residual entropy in this case is identical to that which emerges in water ice, at left, where for each oxygen atom in the lattice, two hydrogen atoms bond closely and two more distantly in tetrahedral bond directions throughout the lattice. Hence, by analogy the antiferromagnetic tetrahedral Ising spin state is called the "spin ice" state.

2.2 Frustration

A system is geometrically frustrated when the local interactions between cannot be minimized while maintaining current locations. [47, 48] As an example in the case of three interacting Ising spins on a triangular lattice in Figure 2.1, antiferromagnetic interaction yields two anti-aligned spins, while the third spin cannot interact antiferromagnetically with both other spins simultaneously. Moreover, there is nothing special about which interaction fails to be antiferromagnetic, and so the entire system can be said to be frustrated.

As an important caveat [18], if the quantum effects are non-negligible on the energy scale of the spin, then a superposition of states could result in a single definite quantum ground state and eliminate the system's degree of freedom due to frustration. A procedure like this is crucial for the restoration of the Third Law of Thermodynamics in ideal low temperature geometrically frustrated magnets because a system would be expected to exhibit zero entropy at zero temperature. [49]

2.2.1 Generalized Schottky Anomaly and the Ising Model on Polyhedra

Frustration can also exist in three dimensions, as in a geometrically frustrated spin state consisting of antiferromagnetic Ising-like spins on a tetrahedral lattice, relevant to the pyrochlore structure discussed below. A thorough study of the Ising model on various polyhedra was undertaken [50], though due to the crystal geometry we need first concern ourselves only with the tetrahedron case.

The important trends as seen in Figure 2.2 are described by the generalized Schottky Anomaly equation:

$$\frac{C_m}{k_B} = \frac{(g_1/g_0)(\beta\Delta)^2}{(e^{\beta\Delta/2} + (g_1/g_0)e^{-\beta\Delta/2})^2} \tag{2.1}$$

where the heat capacity, C_m is equal to a peak dependent on the relative degeneracy between the ground and first excited states, g_0 and g_1, which in the case of a tetrahedron represent the two-in, two-out state we will discuss below and a 'defect' three-in, one-out or three-out, one-in state and the energy between the states, in our case a Kramers doublet of $|J = 15/2\rangle$, Δ as calculated in [51] or [52]. This low temperature Schottky peak is a hallmark of spin ice systems, and an integration of this magnetic contribution to the heat capacity is one of the revealing factors for spin ice behavior.

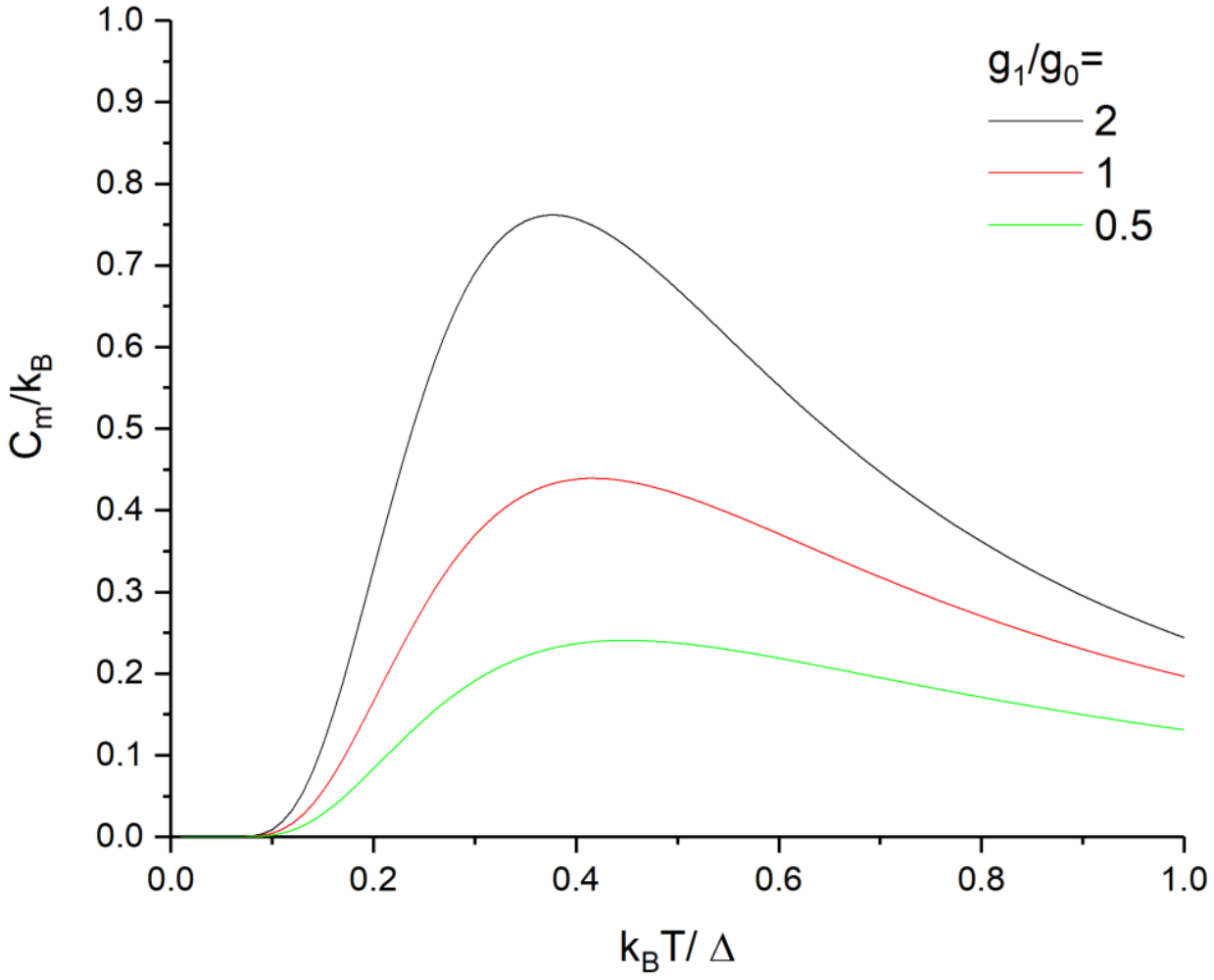

Figure 2.2: Changing the relative degeneracy between ground and first excited states modifies the shape of the Schottky peak in the heat capacity. Both the peak heat capacity value and peak temperature change with degeneracy. [50]

2.3 Rare Earth Pyrochlore Oxides

The rare earth pyrochlore oxides consists of a class of materials with interpenetrating tetrahedral lattices of two species of atoms, with the chemical form $A_2B_2O_7$. The oxygen atoms are located among these two lattices such that magnetic atoms on the A sites and non-magnetic atoms on the B-sites can yield a wide range of magnetic short-range ordered states such as spin glasses, spin liquids, and spin ices. [53] The particular magnetic ordering depends often on complex factors not only of the particular atoms at each site but also the interactions

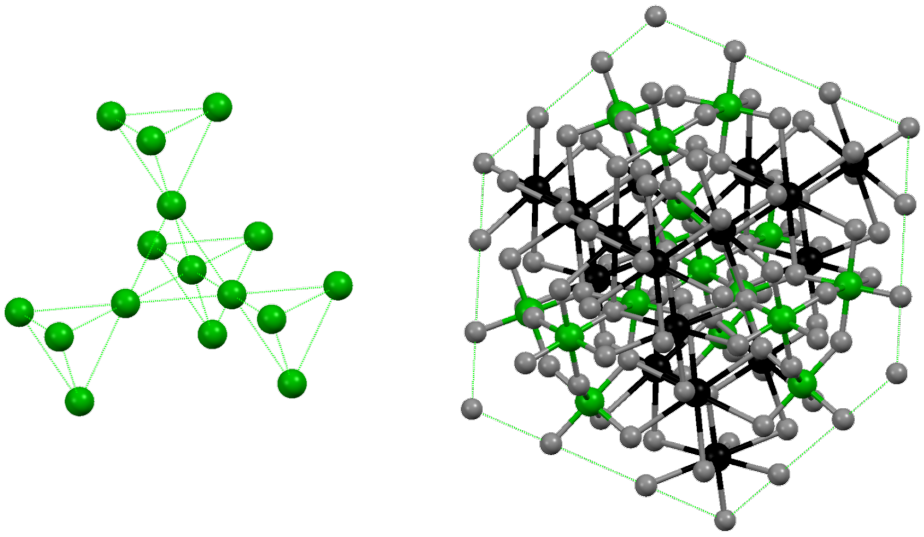

Figure 2.3: A dysprosium titanate cubic pyrochlore unit cell contains 88 atoms and consists of two interpenetrating tetrahedral lattices of dysprosium (green spheres, and extracted at left) and titanium (black spheres). Oxygen atoms (gray smaller spheres) bond (solid two-color cylinders) to the titanium and dysprosium atoms in such a way as to create an easy axis anisotropy for the magnetic dysprosium sublattice. With $J_{Dy} = |\pm 15/2\rangle$, the local Dy interaction is ferromagnetic, but a global antiferromagnetic order emerges below the spin ice transition temperature and fields.

between magnetic atoms and strong sensivity to disorder [54] and vacancy defects. [10]

The relevant pyrochlore oxides to the study of spin ice (see definition, in Section 2.4) are Dysprosium Titanate and Holmium Titanate, two pyrochlores characterized by magnetic sites with very strong dipole magnitudes, as well as interesting low temperature behaviors especially with regard to spin freezing and slow dynamics at lowest temperature. The process by which this magnetic configuration reaches the ground state has been a subject of study for about 20 years. [7]

2.4 Dipolar Spin Ice Model

The antiferromagnetic tetrahedral spin lattice with two low lying Ising states aligned along or against a center-pointing axis ("easy-axis anisotropy") yields a state with the following

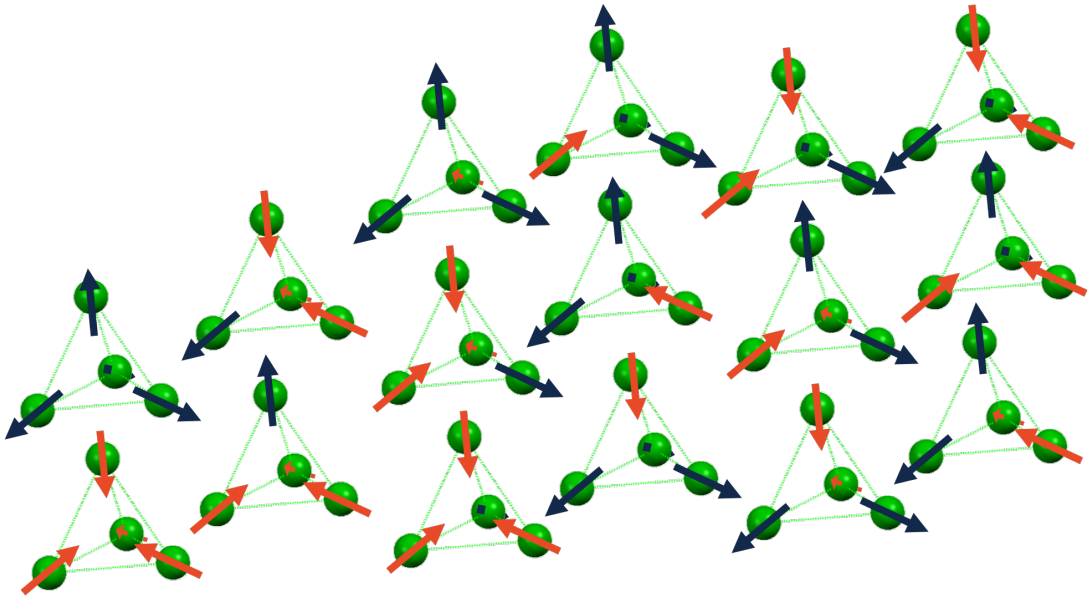

Figure 2.4: Ising spins pointing toward the center of a tetrahedral lattice can assume any of the above 16 configurations, ignoring interactions. With interactions enforcing the ice rules, the spins will end up in one of the six two-in, two-out configurations at right. The sixfold ground state degeneracy is characteristic of residual Pauling entropy. The 3-in 1-out or 3-in 1-out configurations configurations can arise via defects or in the kagome ice state, where 2d planes emerge creating parallel 2d magnetic manifolds from a 3d magnetic state. Finally, the two all-in or all-out states emerge under double defect or saturated states.

properties:

A spin ice derives its name from the similar arrangement of hydrogen and oxygen atoms bonded in water ice crystals, as shown in Figure 2.1. In water ice, oxygen atoms freeze in a tetrahedral lattice with two hydrogen atoms nearer and two hydrogen atoms further along each of the four tetrahedral bonds. This "two-in, two-out" configurations yields a geometrically frustrated state defined as an "ice", and systems exhibiting this state are said to follow the "ice rules" [55], as determined by Linus Pauling in 1935 [56]. The frustration in the ice state lies in the freedom of which two bonds of the tetrahedron hold the "in" and "out" components.

For the case of easy-axis antiferromagnetic Ising spins, as in water ice, each spin is equally

likely to be in either the "in" or "out" state, so there are $2^4 = 16$ total configurations. If the system is constrained to follow the ice rules, as interaction strengths require in dysprosium titanate [57] at low temperatures, then there are just 6 of the 16 configurations available in the ice state, yielding a residual Pauling entropy of $(1/2)\log(3/2)$ solely from the remaining freedom of configuration. This situation arises in dysprosium titanate due to the competition between pyrochlore bond length and spin interaction strength. The easy-axis anisotropy arises from the interaction between oxygen atoms and dysprosium atoms on the lattice. So although the spin ice system may be affected by more variables than the water system - just a positional frustration versus a magnetic frustration - nevertheless, the important result of ice-type frustration is exhibited: residual entropy and configurational degrees of freedom at very low temperatures. Predicted by PW Anderson in 1956 [58], the model for spin ice is that of easy-axis antiferromagnetic Ising spins on a tetrahedral lattice, and it is observed in the rare earth pyrochlores Dysprosium Titanate ($Dy_2Ti_2O_7$, "DTO") and Holmium Titanate ($Ho_2Ti_2O_7$, "HTO"), among other candidates. The hallmark then for determining a spin ice is to look at the entropy at very low temperature. The entropy can be calculated by integrating the magnetic heat capacity of a similar form to that shown in Figure 2.2, via:

$$S(T) = \int_0^T C_m/T dT \tag{2.2}$$

If the entropy integrated from the heat capacity then matches the expected ordered entropy less the Pauling Entropy, the system is in an ice state. Further, applying a magnetic field to the spin ice state in various directions yields complex magnetic landscapes at low temperatures, as shown in Figure 2.5 [59].

The theory for how the spin ice state was originally suggested to be captured entirely by antiferromagnetic nearest neighbor interactions [63], but later models included next-nearest neighbor interactions. [9] These later models predicted fractionalized monopole excitations as defects on the spin ice lattice as we will describe here. We will see in the next section

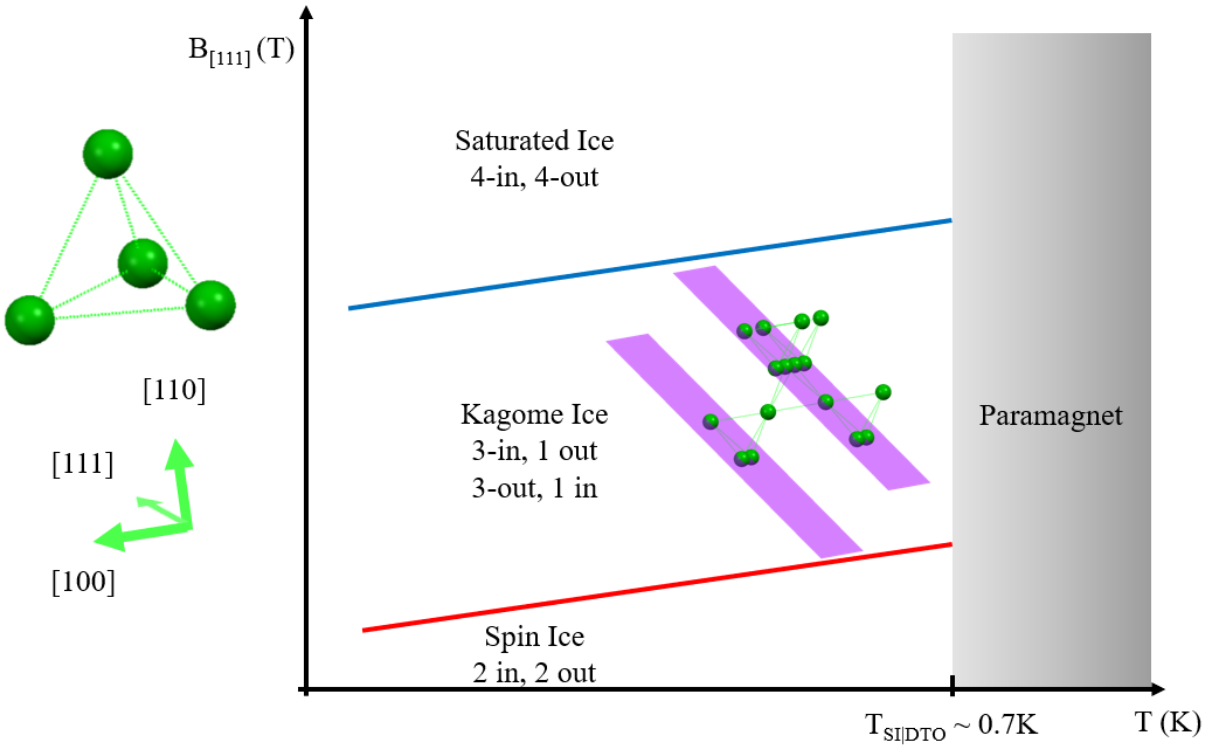

Figure 2.5: Frustrated states are proposed to arise as field is increased in the [111] direction, from 3d spin ice to parallel planes 2d kagome ice to a saturated state (purple planes), as shown. [60] [15] Applying fields along other crystal directions as in the arrows is proposed to yield chains of (anti-)ferromagnetic interactions arising in the [110] direction as both field and temperature are increased [61], and a half saturated state is proposed to occur in the [100] direction as field is varied even slightly, since the field is pointing directly along a crystal axis. [62]

how this theory better accounted for the observed spin ice behavior better.

2.5 Fractionalized Monopole Quasiparticle Excitations

2.5.1 Statics: Dumbbell Model

Single spin flip excitations of the spin ice lattice are theorized to behave like monopole quasiparticles with a magnetic charge of about ten times the Bohr magneton magnitude

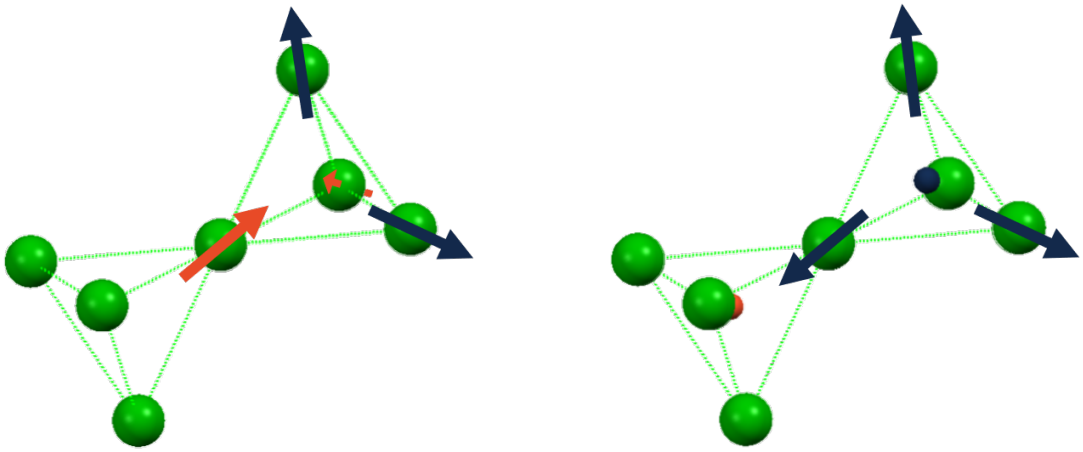

Figure 2.6: A spin flip defect manifest as magnetic charge fractionalization. A three-in, one-out and three-out, one-in pair yields effective free magnetic monopole quasi-particles at the center of each tetrahedron. A chain of spin flips acts as the tensionless Dirac string. Once separated, the defect is equally likely to propagate by flipping a spin in any direction, hence free.

($\mu_{Dy} \approx 10\mu_B$), as follows, and as shown in Figure 2.6. The theory is based on the fractionalization of the spins on the magnetic sublattice. The magnetic landscape can be described by the Dipolar Spin Ice Model (DSIM) Hamiltonian [19]:

$$H = J_{ex}^{nn} \sum_{\langle ij \rangle} S_i \cdot S_j + \frac{\mu_0}{4\pi} \sum_{i<j} \left[\frac{S_i \cdot S_j}{r_i^3 j} - \frac{3(S_i \cdot r_{ij})(S_j \cdot r_{ij})}{r_i^5 j} \right] + \textbf{applied field term} \quad (2.3)$$

where the exchange interaction term J_{ex} and the dipolar term yield a gas of free magnetic charges on the lattice when on a relatively non-negligible energy scale. In the case of a dilute gas of monopoles, we can rewrite the DSIM Hamiltonian in terms of a Coulombic gas of two opposite species:

$$H = \frac{\mu_0}{4\pi} \sum_{i<j} \frac{q_i q_j}{r_i j} + \Delta \sum_i \left(\frac{q_i}{2\mu/a_d} \right)^2 \quad (2.4)$$

where $|q_{DTO}| = q_{Dirac}/7700 \approx 4.3e - 13$ J/Tm. [9] From this we can calculate a density of monopoles behaving as Dirac monopoles on the magnetic sublattice, including a compensating magnetic flux along the Dirac string between the monopole-like ends. In a system with a low density of defects, the theory finds that the effective magnetic charge for the separated spin flips are two distinct opposite-signed magnetic charges.

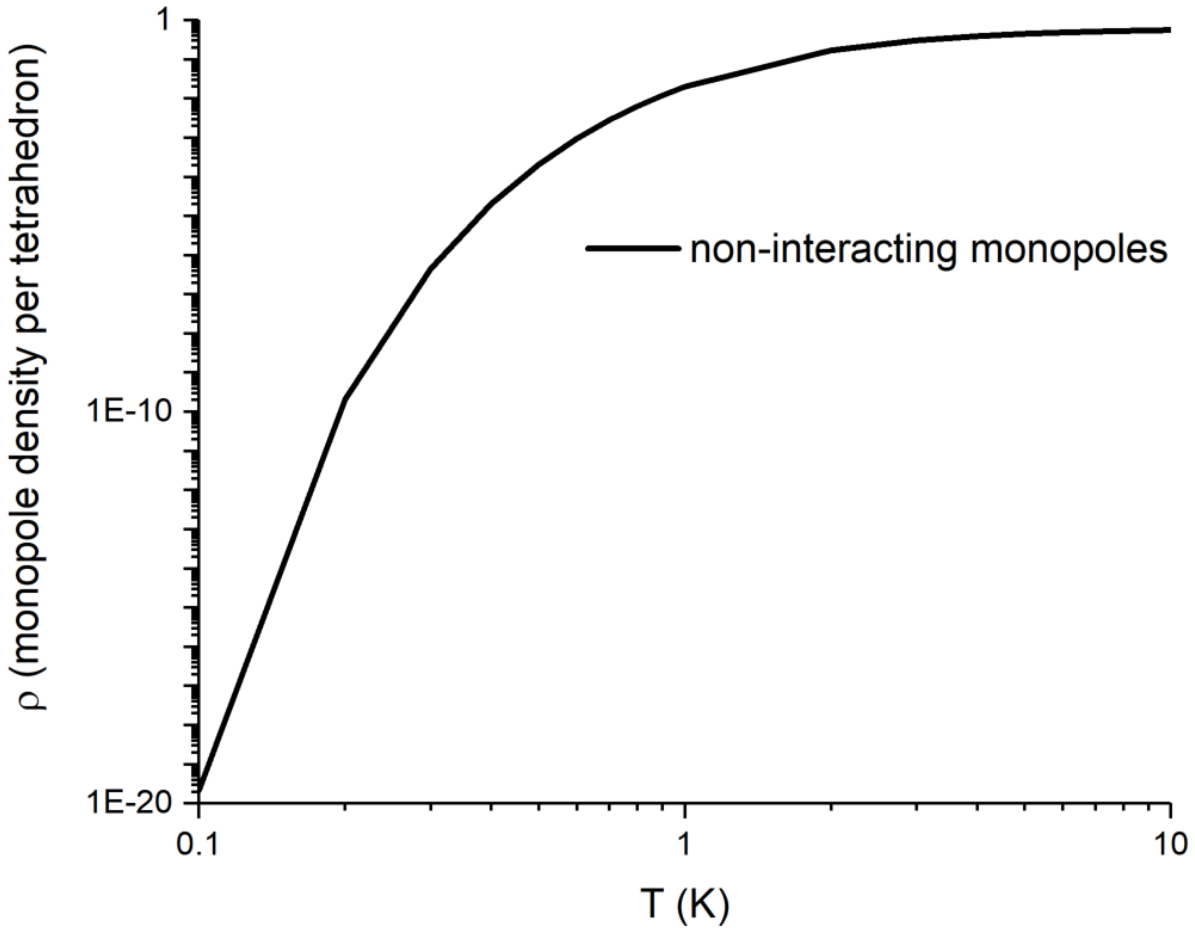

Figure 2.7: The monopole density versus temperature falls off super-exponentially in the non-interacting case, yielding a useful density tuning parameter in the temperature. [64] [65]

In Figure 2.7, we can see some predictions from the DSIM theory of fractionalized monopoles on the tetrahedral lattice. Notably, the superexponential decline of monopole density, ρ, with temperature is a useful and dramatic indicator of the presence of such defects. In Figure 2.8, we can see that the Debye screening length, $L_D = (k_B T/2\mu_0 q^2 \rho)^{1/2}$,

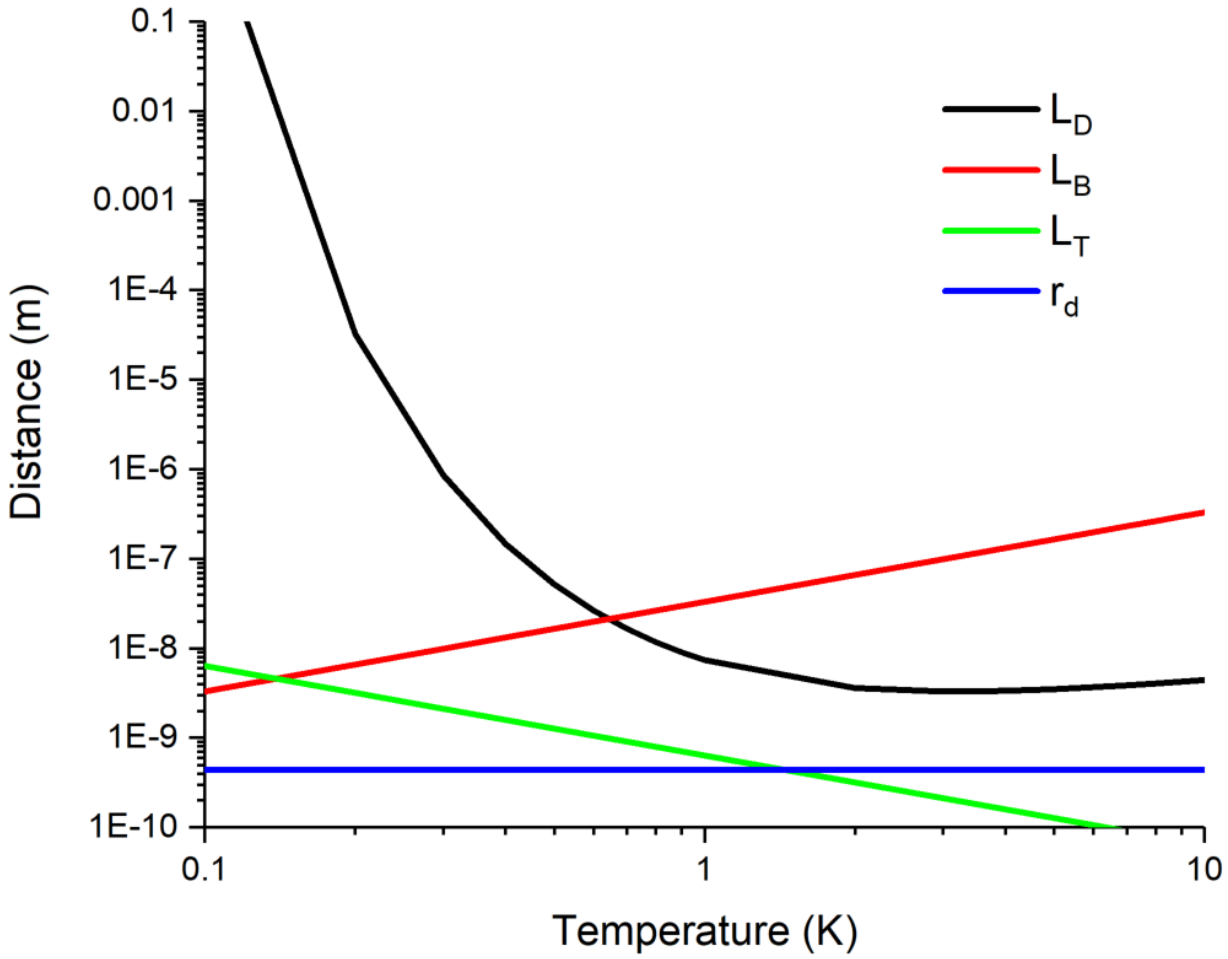

Figure 2.8: Various length scales (see text) compared to the tetrahedral bond length, r_d, relevant to the monopole picture vary with temperature in contrasting ways, from the summary of relevant lengthscale equations in [66] with [67].

above which monopoles are screened, increases dramatically at low temperatures. The discernable monopole drift length $L_B = k_B T/qB$ crosses over the maximum Coulomb binding length $L_T = \mu_0 q^2/8\pi k_B T$ near 100mK. Thus a magnetic probe which seeks spatial resolution of the statics of the monopole distribution has its best chance between about 100mK and 1K on the order of lengths up to even the millimeter scale.

2.5.2 Dynamics: Two-component Plasma and Debye-Huckel Magnetolytes

The defects created in the fractionalization process are able to propagate via single spin flip processes. These effectively decoupled magnetic charges then can propagate via any process that causes a spin to flip. However, since both a positive and negative charge are created, we must consider the dynamics of a two-component charged fluid on the pyrochlore lattice, with creation and destruction operators when new pairs are created via defect. [64] The equations that govern the dynamics of a dilute two-component gas are the Debye-Huckel Theory, which for our purposes helps to give an idea of the mobility of defects on the lattice. Ultimately, the key equation describes this behavior as a relaxation channel with a single characteristic relaxation time, τ, associated with a dressed monopole energy cost, Δ_d:

$$\tau = \tau_0 exp[\Delta_D(T)/T] \tag{2.5}$$

However, as was noted in the section above on the state of the field, the time scales associated with relaxation in the spin ice crystals have disagreed experimentally both with the theory and other experiments. [68] Moreover, the experimental data may indicate that there is not one but multiple relaxation channels, further complicating the simple DSIM fractionalized monopole picture. [69, 70]

Additionally, it has become apparent experimentally that certain other lattice defects can act as pinning sites for the spins, inhibiting their dynamics. [10] Also, some theorists have posited that slow dynamics may be due to the formation of double defects, essentially 4-in or 4-out sites where the energy cost to flip spins on that lattice site become much higher. [27]

2.6 Surface and Strain Effects

Furthermore, the spin ice investigations above have so far not considered finite size or strain effects explicitly. Theorists however have begun to look at the effects of these types of physical imperfections and the effect they have on the spin ice state and the various measurements we associate with spin ice. For example, it has been calculated in [71] that a spin ice lattice oriented in the [001] direction can generate a square ice ordering from the orphan bonds on the surface. Depending on the interaction strength and sign of the orphan bonds, the Schottky-like peak seen in the heat capacity measurement may have a modified shape or an additional low temperature peak. The surface ordering effects are seen as changes in even lower temperature peaks in very thin films below 0.35K, which we could not access experimentally.

On a similar note, the reduced dimensionality effects seen in a simulation from [26] shows how the combination of interaction strength and number of unit cells in thickness modify the heat capacity Schottky peak by adding a significant peak at certain values of orphan bond strength and very few (< 3) layers. These behaviors in can be compared to the effects of relative degeneracy in the Ising polyhedra seen earlier in that all three: ordering, dimensionality, and degeneracy have an effect on the Schottky anomaly. Notably, changes in degeneracy can be thought of as caused by pinning sites or defects or strain in the lattice, since spins which are no longer equally likely to flip as the others may be affected by this type of disorder.

2.7 Numerical Modeling

To get a better handle on what we might expect from thermal, magnetic, and structural measurements we have recently begun our own work on simulating our results seen later in the chapters on results. These efforts are just beginning but are valuable for understanding the exact causes for the trends we are seeing. For example, Monte Carlo simulations of

constrained films can be used to distinguish the effects of strain from the substrate versus reduced dimensionality effects as the relevant length scales shown for spin ice dynamics become smaller than the available dimension. [72] This work is ongoing but worth mentioning as it may provide more comprehensive conclusions to the trends we are seeing in the data in the following chapters.

Chapter 3

Techniques and Equipment

3.1 Sample Creation

In collaboration with Dr. Alex Thaler of Prof. Gregory MacDougall's group, crystals of $Dy_2Ti_2O_7$ via a floating zone furnace process and compressed powder targets for thin films of $Dy_2Ti_2O_7$ were created. For the crystals, the goal was to create high quality samples under varying oxygen atmospheres, to help resolve the open question of what effect the oxygen content of spin ice materials might have on the statics and dynamics of the magnetic landscape with the ultimate goal of facilitating SQUID measurements in low temperatures or quickly changing fields. For thin films grown via a pulsed laser deposition process, although the initial goal was to create a more workable probe for SQUID magnetometry via known thickness and wide uniform surface area, structural and thermal properties were measured also to probe the effects of dimensionality reduction, surface effects, and strain effects on an inherently three dimensional geometrically frustrated and fractionalized system.

3.1.1 Crystals: Floating Zone Furnace

A floating zone furnace is used to turn polycrystalline $Dy_2Ti_2O_7$ powder into a single crystal oriented along a crystal direction of a seed crystal via a slowly translating zone of high temperatures used to melt and recrystallize the material along the same axis.

The crystals were then oriented using a Laue x-ray machine along useful crystal axes: [100], [110], and [111]. These then were cut using a diamond wire saw to provide samples

small enough to fit within the magnetic measurement setups and to obtain heat capacity data from.

Figure 3.1: $Dy_2Ti_2O_7$ samples grown under 9.5 atm, 7.5 atm, 5 atm, 2.5 atm, and 1 atm oxygen atmosphere from left to right, showing color and transparency variations between and within sample growths.

There has been some debate [10] as to the significance of color or transparency variation between samples, and if color can be used as an indicator of sample quality or of any particular defects in the crystals. As seen in Figure 3.1, the color variations throughout the crystals is similar to the color variations between the crystals, and so it is not clear from our samples whether color is significant. Moreover, this agrees with other brief investigations of spin ice color and transparency [73], and so other measures of sample quality are more useful, such as x-ray diffraction.

3.1.2 Thin Films: Pulsed Laser Deposition

Pulsed laser deposition (PLD) allows for the creation of thin films of complex materials by ablating compressed powder targets in controlled environments and depositing target material in an ordered fashion by high temperature treatment on an oriented substrate. There are many types of thin film deposition systems, including physical deposition processes like PLD, chemical deposition, and molecular beam epitaxy. Each of these has advantages to grow different types of material, and PLD had been successfully used to grow thin films of spin ice materials. [34–36]

A PLD system consists of a repeatedly pulsed high power laser, a system of treating and focusing the beam, and a windowed vacuum chamber capable of precisely hosting a rotatable target mount, a high temperature substrate stage, and a well controlled gas environment. The art of the PLD system is to effectively deposit the target material plasma plume created by the laser ablation onto the substrate. The system in use will be described below:

In the setup, the laser is a 1 Watt Krypton Fluoride excimer laser, with a wavelength of 248 nm. The gas pressure is kept between 3300 mbar and 3500 mbar. The beam emerges with a circular spot size of about 1/2" in diameter. The laser is either computer-controlled, or operable manually by push-button. The frequency of laser pulses can be coordinated with the angular speed of rotational stages: 1) to induce even ablation on a single target; 2) to be timed to alternate between up to 6 targets in a multi-target system; or 3) to achieve varying levels of target heating as energy is deposited in the target. The laser is connected to the necessary mixtures of gases set to pressures as specified by the laser manufacturer. This gas handling system contains fluorine gas, and special precautions are taken to ensure fluorine gas is evacuated or detected. In this way the beam energy can be produced consistently within about 10 percent of a specified beam energy. Over the course of a typical growth (1000s of pulses) the beam average energy should be close to the set point.

Further reduction of the variation in beam energy can be achieved through the use of

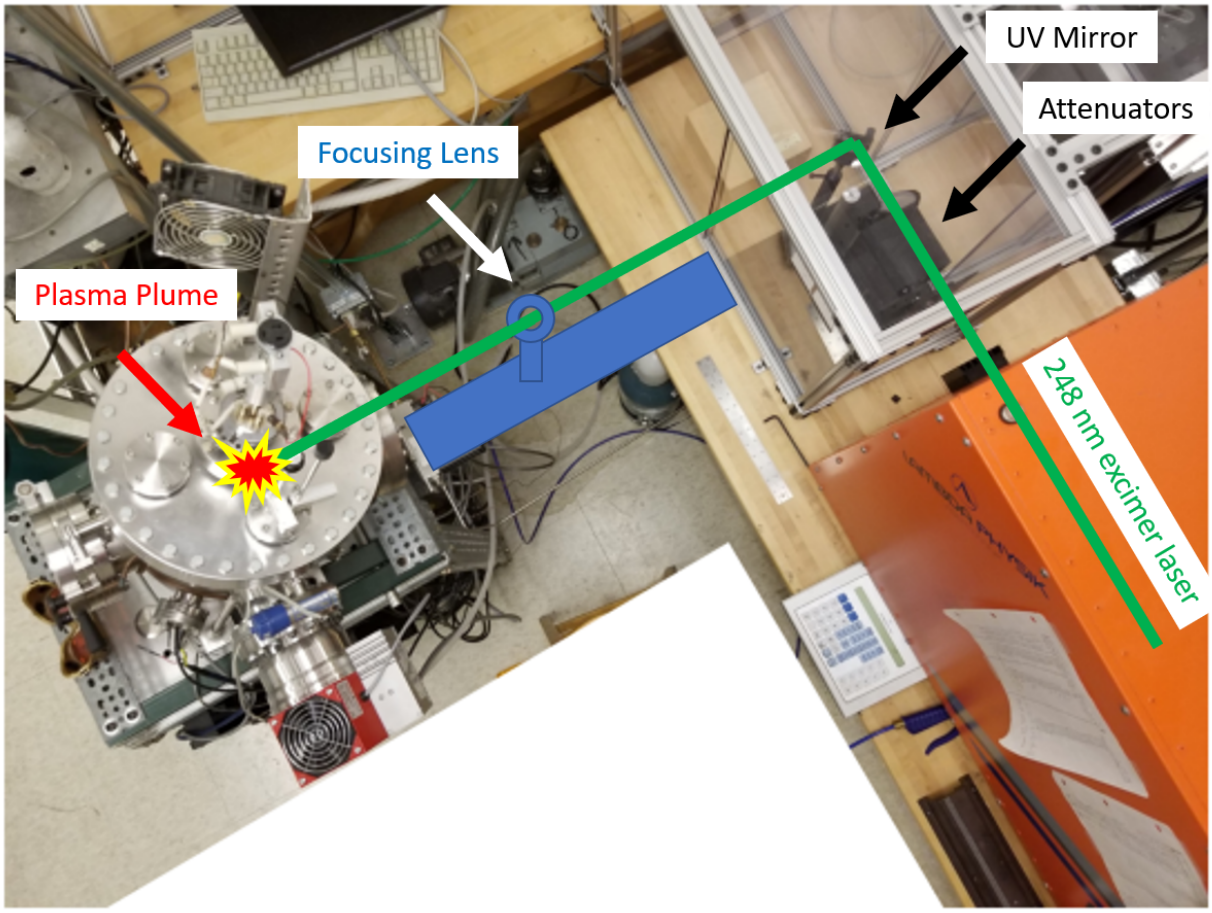

Figure 3.2: The pulsed laser deposition system we used. A computer-controlled krypton-fluorine excimer laser is aligned with three deposition chambers. The beampath first passes a rectangular beam slit, then several attenuators, then mirrors which direct the beam towards one of the three chambers. Each chamber then has a series of mirrors and lenses to direct and focus the beam onto the target within the chamber.

attenuators instead of adjusting the laser energy itself. Attenuators reduce both the beam energy and the variation in the energy density at the target proportionally, and so we can get a more consistent beam energy density at the target. This is important for growths with few pulses (very thin films) which may only have on the order of 100s of pulses. Varying the number of attenuators also changes the attenuation factor and allows deposition as the laser beam energy changes due to slow pressure changes in the laser system, preventing the need to constantly refill the laser gas.

The laser pulse can also be shaped to allow for more precise spot size control. For our particular setup, there is a rectangular slit between the laser exit and the attenuators, which allows us to ablate a mostly radial region on the target by centering the beam on a point halfway between the center of the target and the edge, then centrally rotating the target. With appropriate beam spot size, this creates a uniform annulus of ablated material, preventing over-ablation at the center (like in a kitchen microwave oven) as well as avoiding ablation of the mount material.

An optics table allows for the precise alignment and focusing of the beam into the chamber window and onto the target. For our setup, a UV mirror can be precisely aligned both vertically and horizontally using fine adjustment screws. The directing UV mirrors are mounted on foldable stands, to prevent the need to realign beamlines with every chamber change. Almost all of the optical equipment is contained within a UV-reflecting lexan box, to prevent errant beam scattering. A 20mm diameter lens is placed next in the beam path, which then focuses the beam through a UV-transparent chamber window onto the target in the depositon chamber. Alignment and positioning of the lens uses a ruler fixed parallel to the beam path between the mirror and the chamber window.

The deposition chamber, and the associated target and substrate mounts, are conveniently tilted at a 45 degree angle to allow for a clean incident beam and ejected plasma plume. While commercial chambers are made by such companies as Neocera, which provide multiple target stages rotatable and interchangable in-situ, the chamber we use is an

in-house system consisting of a purpose-built 45-degree tilted vacuum chamber with a single rotatable target mount centered facing a heated substrate mount with an adjustable separation. This chamber was originally designed by Ralph Schweinfurth, and further details of its construction can be found in his thesis. For our setup, the important features will be detailed below, including the atmosphere handling and monitoring system, the substrate mount and PID heater control, and the target mount and magnetically coupled rotor.

The deposition chamber is evacuated using a roughing pump and turbomolecular pump from Pfieffer, with an attached fan and control module. The turbo pumping rate at low pressures is further controlled by a manual shutter which can be rotated 90 degrees to change roughly and quickly the effective pumping power. Coupled to this is an oxygen gas mass flow control system, where a controlled pressure of oxygen can be maintained in the chamber to ensure stoichiometric deposition of films. The pressure is read using an ion gauge.

The substrate is mounted on a vacuum compatible heated platform hung from a KF connection. The platform contains a heating element and a thermometer, both connected to a PID control unit. This maintains the substrate at a desirable temperature throughout growth. The separation of the substrate from the target can be adjusted in 3 dimensions with a set screw and by rotation to adapt to the incident plume size and location.

The target is mounted on a solid copper block for thermal uniformity. The copper cylinder sits on a magnetically coupled rotor allowing for coordinated control of the target ablation distribution.

Substrate Selection

Prior to this work on thin films, two experimental studies of spin ice thin film materials had emerged. [34,35] Each study chose a different spin ice material and a different substrate material. Ultimately their results indicated that the choice of substrate may play a critical role in the persistence of the spin ice state under dimensional reduction. The reason given

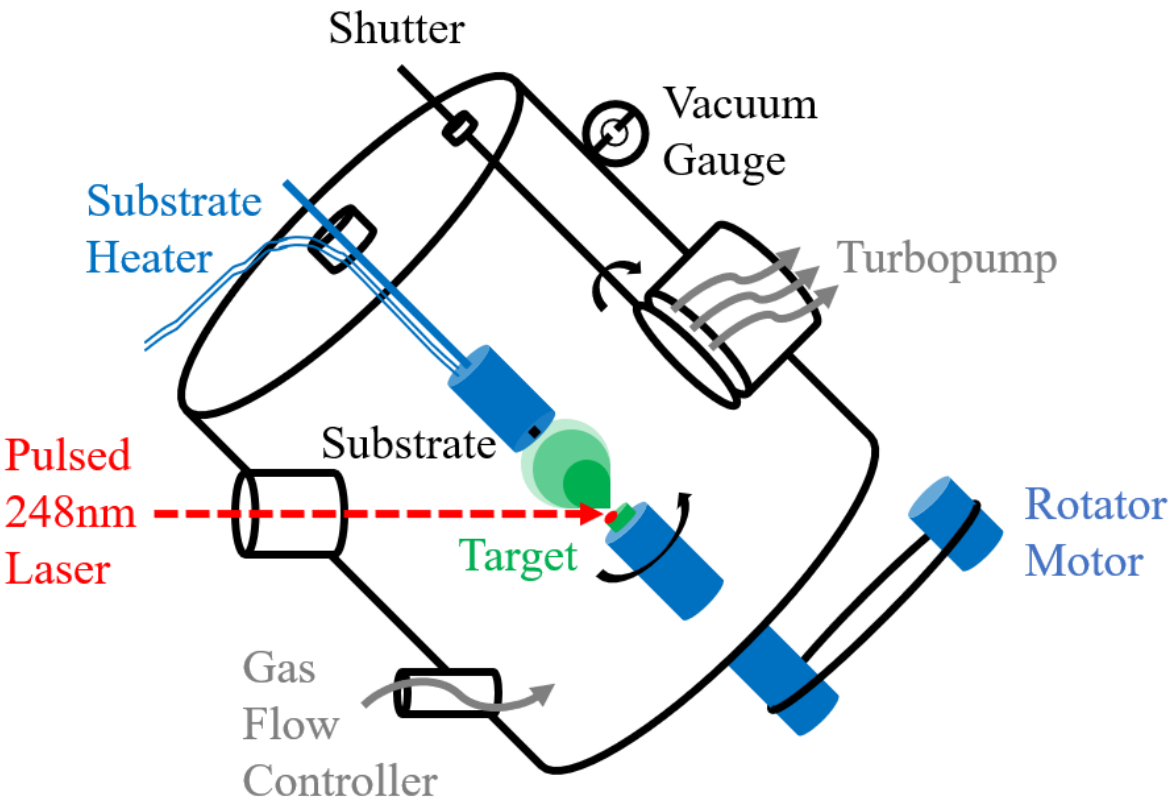

Figure 3.3: The vacuum chamber used contains a window for the laser to enter the chamber and ablate a plume of target material from the target at an angle. Above the rotating target is the substrate affixed to a heater. Gas inlets and careful pumping and pressure measurements allow for precise growth conditions.

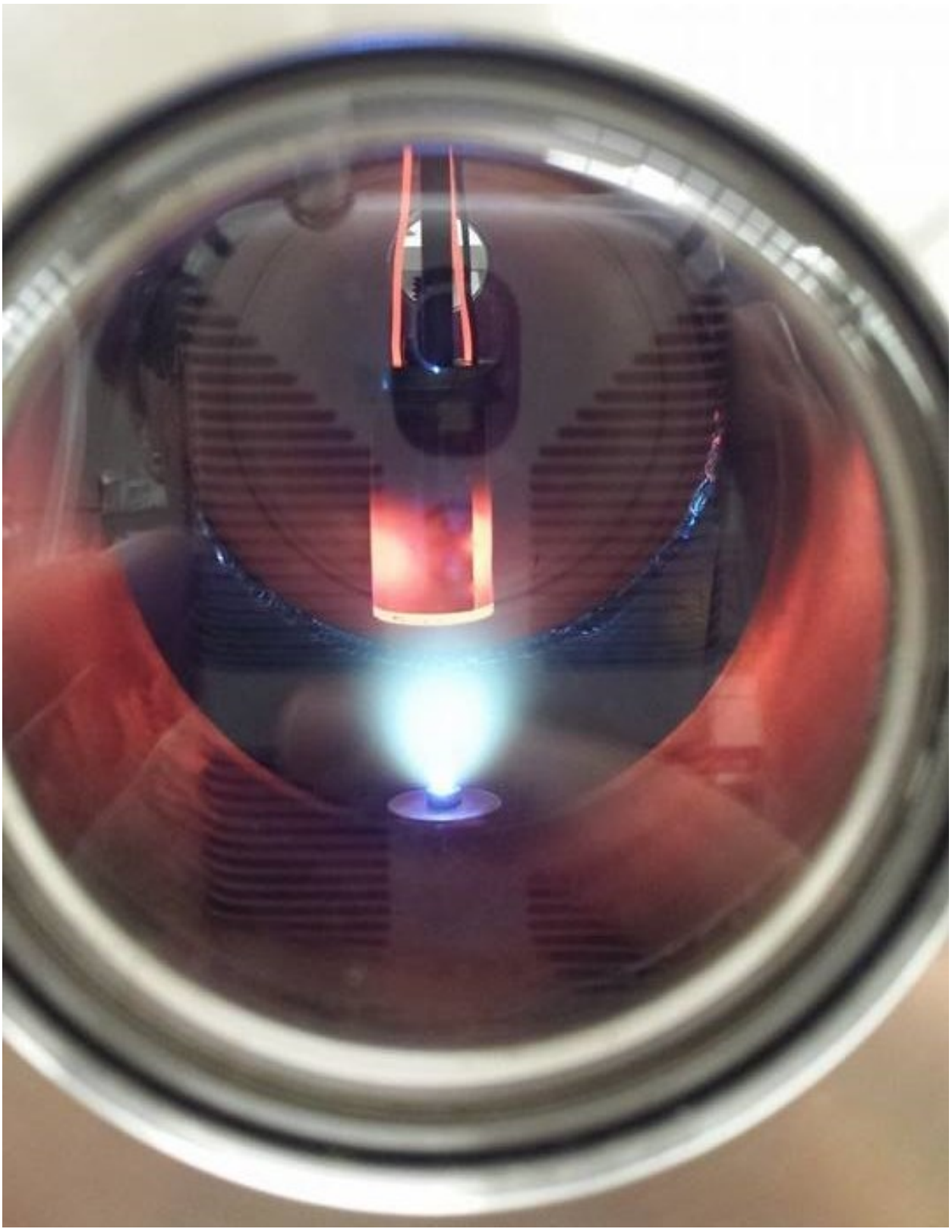

Figure 3.4: When ablated in the carefully controlled environment, a plume of ablated material transfers target material onto the heated substrate.

in one instance related to the existence of strain in the films caused by the mismatch of the lattice parameter of the thin film to the lattice parameter of the substrate. Although all film and substrate materials exhibit the same crystal structure, cubic, a mismatch between substrate and film lattice parameter means that at the interface the film will either be strained to match the substrate lattice parameter or else the bigger risk emerges of growing a non-oriented or mis-oriented film.

As noted in the theoretical section on strain and surface effects, the signatures of strain, surface ordering, and dimensionality reduction behave differently. The particular way in which the Pauling entropy was restored was credited to strain effects, though it is not clear that strain is the only effect that may cause such differences. So, in a first effort to obtain DTO films that exhibited spin ice behavior, DTO films were grown on a yttria-stabilitized zirconium substrate, a crossover approach to the prior groups which could also help resolve the debate over the behavior of spin ice materials at thinnest levels as in Figure 3.5.

3.2 Thermal Probes

As an insulating material, one of the primary ways information can be accessed about the crystalline behavior of the system is through thermal measurements. At higher temperatures this behavior is dominated by Debye-like phonons, carrying thermal currents through the crystal via lattice vibrations. Dysprosium titanate exhibits a regime dominated by phonon transport down until about 4K where magnetic contributions to the heat capacity become important as the spin ice state emerges from a paramagnetic state. There are also nuclear contributions to the heat capacity from nuclear degrees of freedom, but these do not appear in a heat capacity measurement significantly until about 100mK. There are also no significant crystal field effects at these low temperatures, and so for DTO the primary components of the heat capacity are magnetic and phononic in origin.

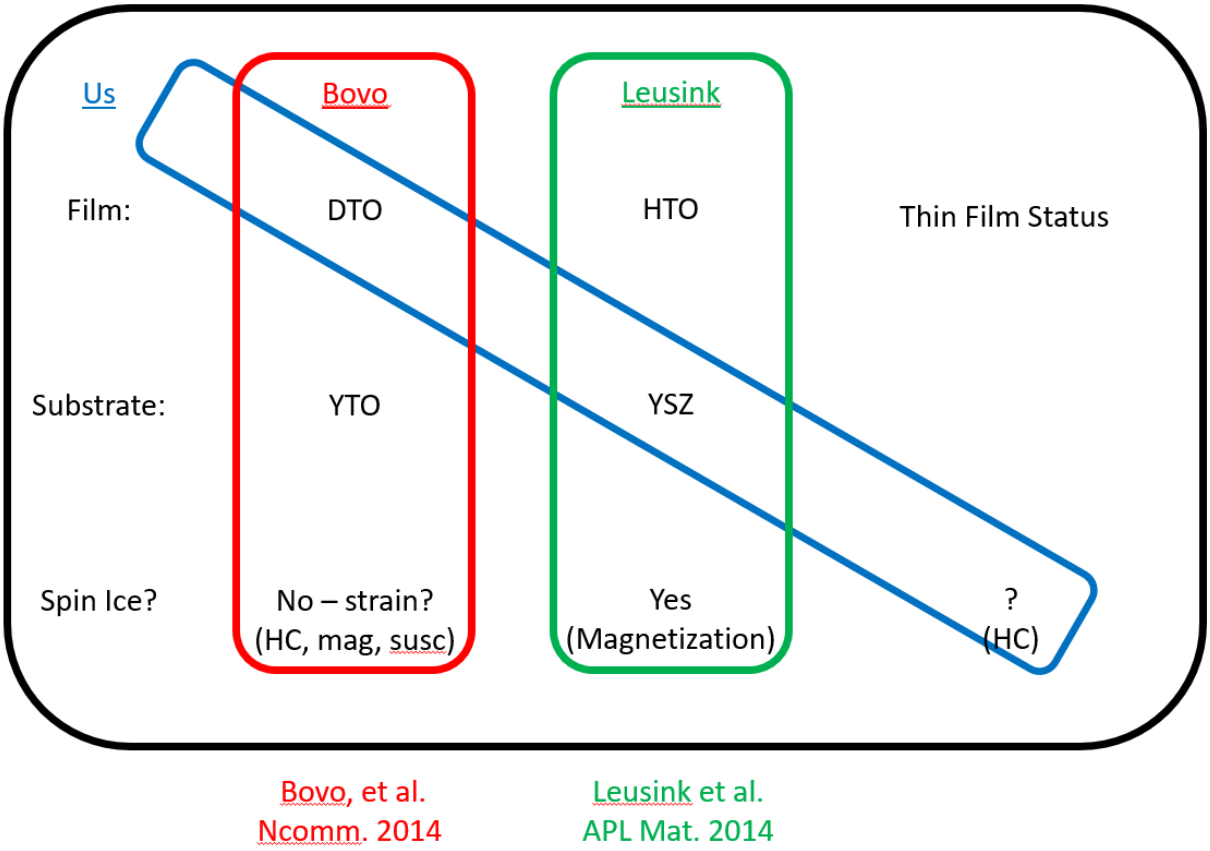

Figure 3.5: A graphical summary of the open questions in the field and our method of seeking answers to some of them via a crossover film growth approach.

3.2.1 Heat Capacity

At lower temperatures, prior measurements [8] have indicated that the primary cause of changes in heat capacity are due to the magnetic ordering of spins. It is this entrance into the long-lived spin ice state that causes the signature residual Pauling entropy. Therefore a measure of the heat capacity, when integrated, is an excellent measure of the fidelity and uniformity of the spin ice state. It also is importantly a non-directional measurement, which does not depend on mass, size, or shape of the sample. Although lower mass measurements take less time, a heat capacity measurement is a great way to pin down the ordering of the spin ice state on the single tetrahedron level. Like neutron scattering, which has a similar sensitivity and magnetic measurements which rely on bulk effects, the magnetic component

of the heat capacity is a key measurement in characterizing the behavior of spin ice material.

Heat capacity measurements were carried out using the two-tau method on a heat capacity option for the helium-3 insert in a Physical Property Measurement system. The PPMS HE-3 is capable of reaching temperatures as low as 300mK, and for this work data was taken as low as 400mK. Lower temperature data was attempted, though stability was an issue.

Data is taken in the following manner: a small spin ice sample (on the order of single mg) is affixed with n-grease to a stage suspended by 4 contact wires. This stage contains a very sensitive thermometer and heater, which introduces heat to the sample and measures the heat flow into and out of the sample carefully over time. The heat flow is measured and fitted to a two times scales, indicative of the rate at which heat may flow into and out of the sample.

The key advantage of using the commercial PPMS heat capacity system is that the heat flow not only must account for the heat into and out of the sample but also heat which flows into the rest of the insert, as well as how heat is absorbed by the adhesive used, which is n-grease in our case. This can be represented in a thermal resistance diagram. The commercial system allows for easy calibration and addendum runs which can then be automatically removed from the excess heat capacity due to the sample which you are measuring.

3.2.2 Entropy

The heat capacity measurement then is done in the carefully controlled thermal and magnetic environment provided by the PPMS. With the contributions from the non-sample parts already subtracted, only the magnetic contribution is considered. To do that, the higher temperature Debye phonon contribution must be fitted and removed.

Taking data for the $Dy_2Ti_2O_7$ samples in the range of 10-30K gives a contribution dominated by the phonon thermal channels, and fitting to the Debye phonon form allows us to subtract the most significant non-magnetic contribution in the range under 10K and above

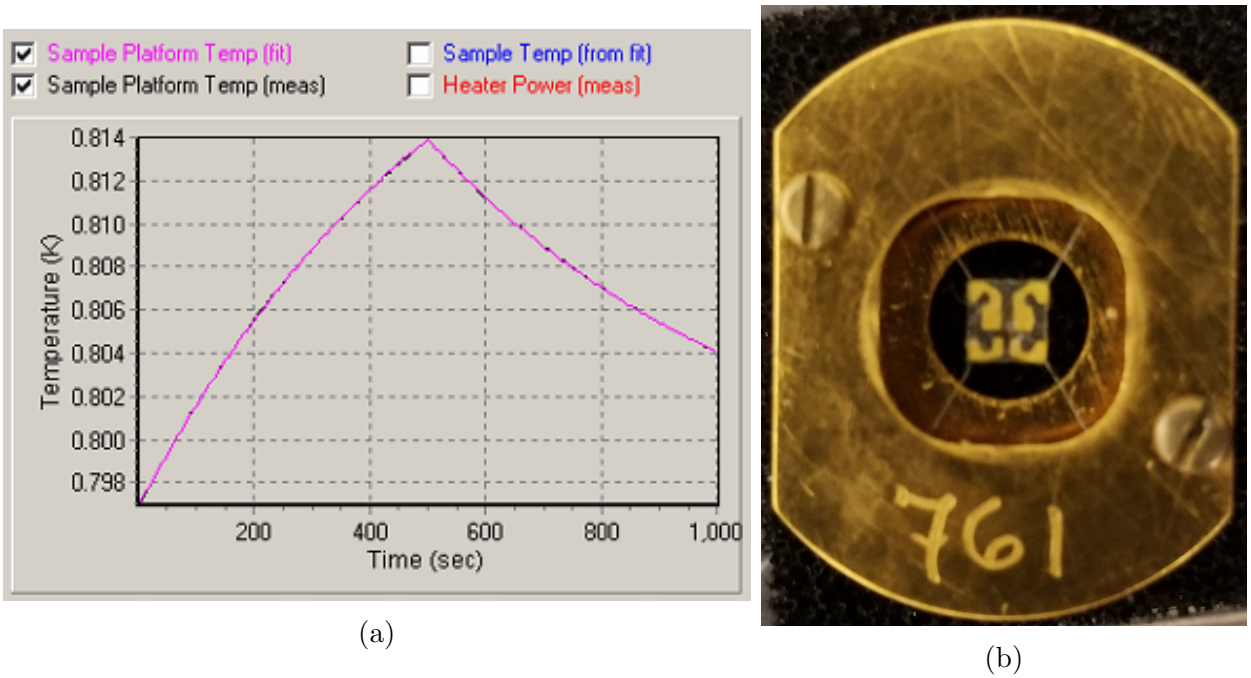

(a) (b)

Figure 3.6: (a) A heat pulse in introduced into the sample area and carefully measured. The current is then removed and the temperature again carefully measured as the heat flows out of the stage. [Quantum Design MultiVu Software-controlled] (b) A four-wire suspended thermal setup. Precise control of heat into and out of the suspended platform is combined with well characterized background heat capacity measurements to determine the contribution to the overall heat capacity by the sample. Samples must be smaller than the suspended stage, which for DTO is generally less than 10mg. [Quantum Design He-3 Heat Capacity Puck]

100mK, which is below our lowest achievable temperature in the PPMS, which is on the order of 300-400mK using a He-3 cooling circuit insert.

Integrating the remaining magnetic component of the heat capacity allows us to get a direct measure of the entropy loss associated with the formation of the ordered spin ice state. As in Section 2, the residual entropy arises from the configurational equality of spins pointing in or out of the tetrahedra. Practically speaking, though, the primary obstacles in measuring the entropy of the low temperature spin ice state arise on the low temperature and long time extrema of measurement.

As the Third Law of Thermodynamics requires, systems must tend towards zero entropy at zero temperature, though not necessarily on experimentally-accessible time scales. [18] For our systems, there is a clear Schottky-like anomaly in the heat capacity which emerges as

the system nears 1K. Lower than 1K, however, the behavior between the lowest temperature data points and the presumed end of the magnetic contribution must be fitted to an expected distribution to get an idea of how closely the data fits a canonical spin ice state, as seen in Figure 3.7.

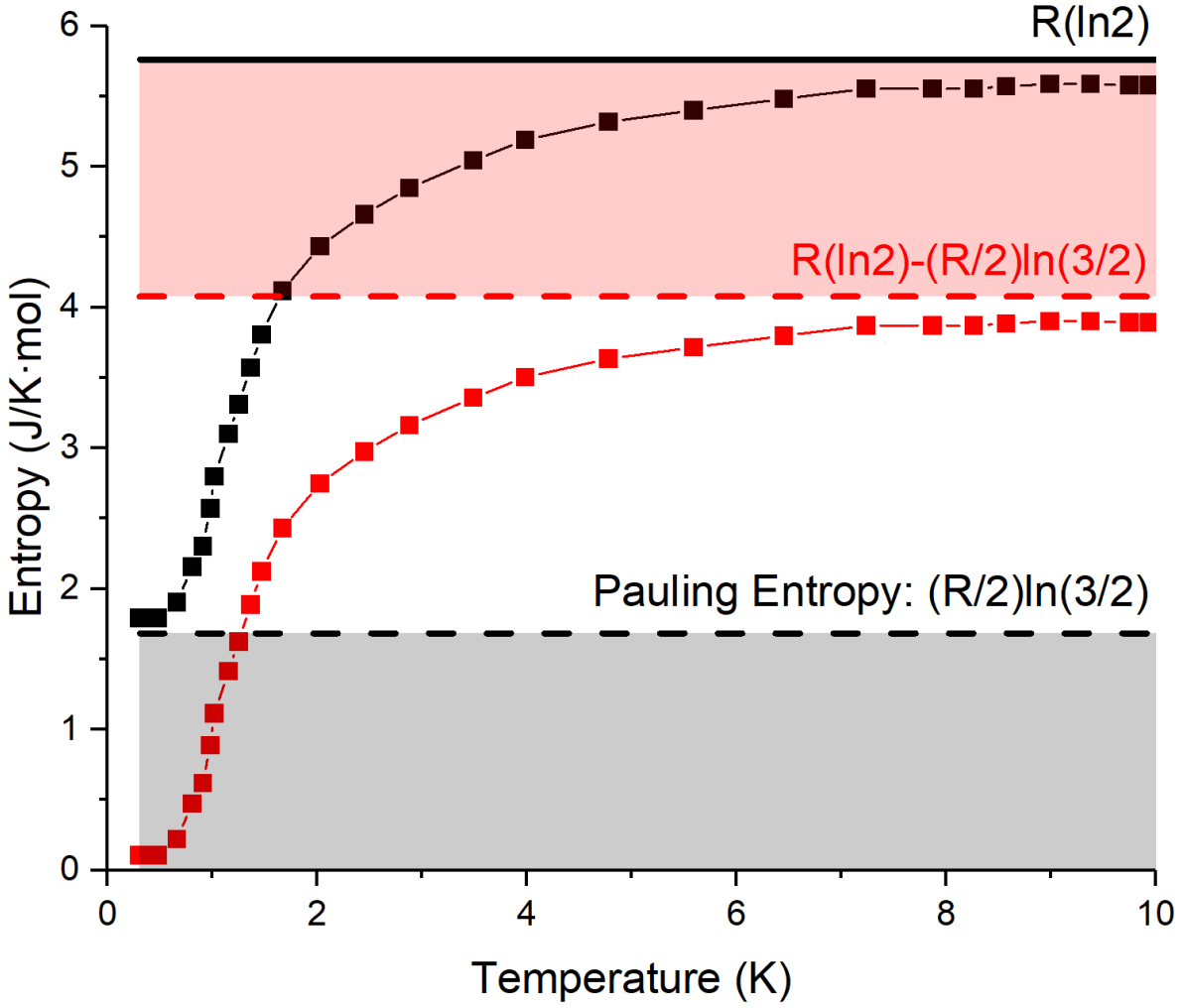

Figure 3.7: A typical result for spin ice heat capacity, shown with and without the residual entropy subtracted. Representative data adapted from [8].

Additionally, there has been an issue in the field regarding the behavior of spin ice materials at long time scales, and the cause of this long-time behavior was one of the primary drivers for growth of many crystals in multiple different oxygen pressure environments. Prior measurements have mixed indications of the effect of slow dynamics on the heat capacity

values seen at lowest temperatures. One paper showed data which indicated that the Pauling entropy was partially recovered on extremely long timescale measurements, indicating very slow dynamics [28]. Other measurements presented at the APS meeting detailing neutron scattering measurements carried out after similarly long time scales did not indicate any difference in behavior [29]. Some other measurements done on oxygen annealed or non-annealed samples of $Dy_2Ti_2O_7$ and $Y_2Ti_2O_7$ give some idea that oxygen does play a role in affecting these thermal measurements by changing the relaxation time [10]. Finally, a close nuclear synthesis indicated that the isotope of Dy which is present in the samples does not make a significant impact on the spin ice canonical heat capacity behavior. [29]

3.3 Structural Measurements

To understand the stoichiometry and quality of our samples, both crystals and thin films, a variety of x-ray probes can be used to measure the sample lattice parameter, orientation, thin film thickness, and composition.

3.3.1 X-ray Diffraction

X-ray diffraction relies on the scattering of an x-ray beam through the repeating lattice of the target crystal. Bragg peaks seen in an angular scan of the scattered x-rays indicate the lattice parameter based on the known crystal structure.

For $Dy_2Ti_2O_7$, the pyrochlore lattice is an interpenetrating tetrahedral lattice. The overall structure is cubic, $Fd\bar{3}m$, and so the Bragg peaks and x-ray diffraction measurements follow simple cubic lattice vectors and analysis. For our purposes then, the peaks show up near:

$$\begin{aligned} \lambda &= 2dsin\theta \\ d_{hkl} &= a/(h^2+k^2+l^2)^{1/2} \end{aligned} \tag{3.1}$$

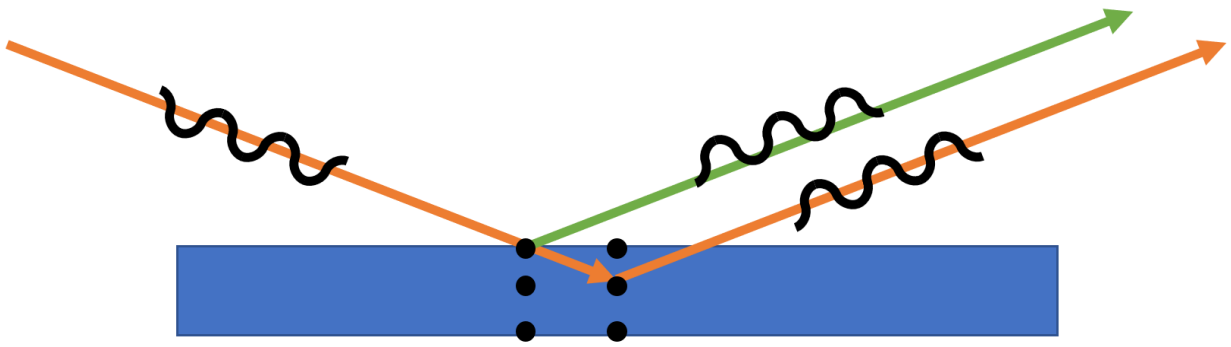

Figure 3.8: Bragg's law allows for constructive x-ray scattering interference to yield lattice parameter information from crystalline targets.

Further information on the uniformity of the sample is available from the peak intensity and the broadness of the peak. A broader peak indicates that not all of the crystal has the same lattice parameter. Some broadening can indicate strained or deficient portions of the crystal. For example, prior work on $Y_2Ti_2O_7$ indicated a lattice parameter change on the order of 0.1 percent as the sample was annealed in a deprived, standard, or high pressure oxygen environment. [10]

3.3.2 X-ray Reflectivity

X-ray reflectivity is a measurement which relies on the shallow angle incidence of an x-ray beam and the resulting interference patterns between the reflected x-rays from the film surface and the substrate surface. This process yields information on the thickness of the thin film, and works best on films and substrates with a uniform surface.

The substrates used in this work were commercially-bought cut and oriented Yttria-stabilized Zirconium, which yielded a smooth substrate surface. The films had mixed success on the smoothness front, as will be seen in following sections. The fitting for the film thickness versus expected reflected x-ray pattern is empirical, and so an example is shown here:

The fitting is done via FULLPROF software suite, but the key qualitative feature is the presence of the sinusoidal oscillations after the drop at low angles. The spacing of the peaks

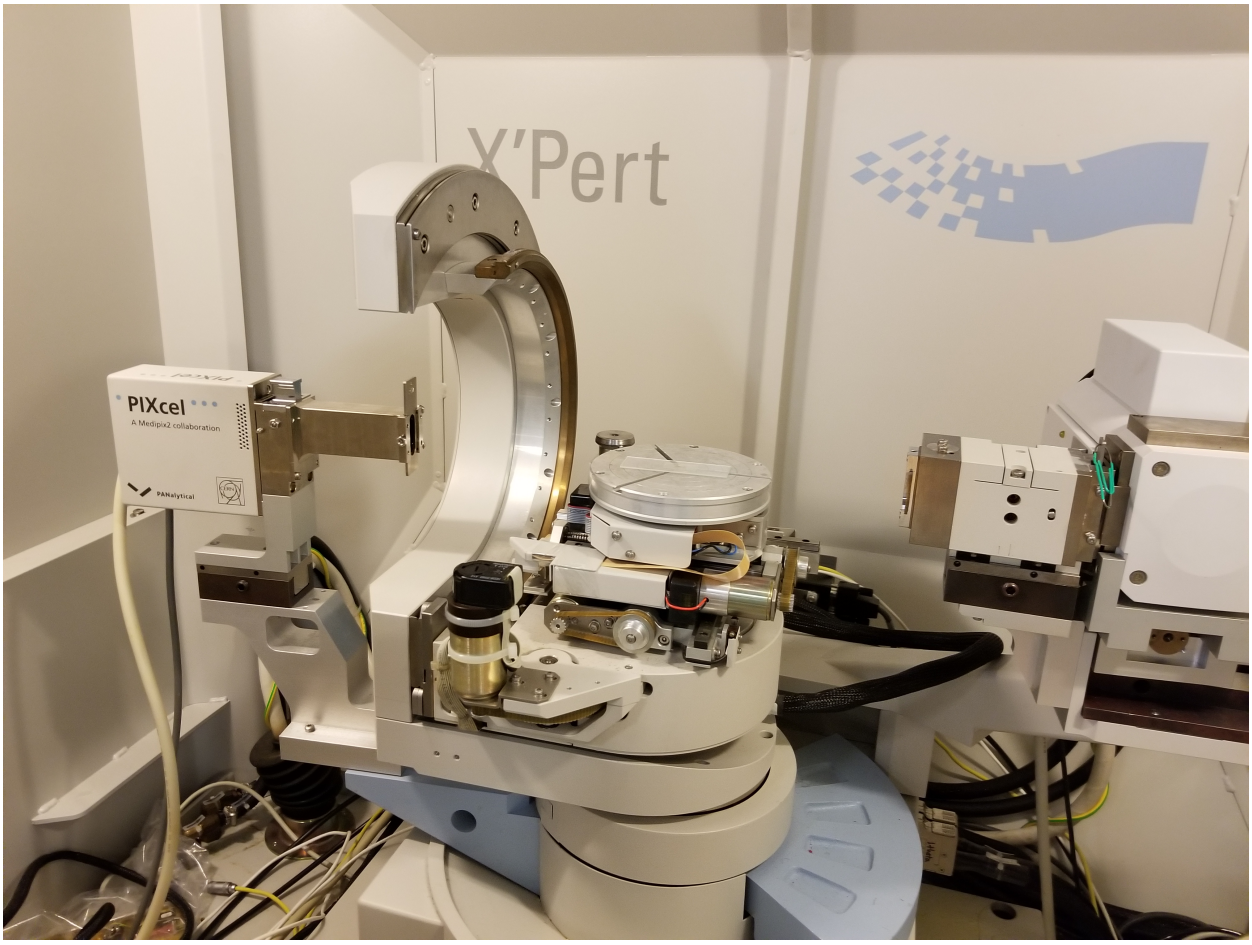

Figure 3.9: A Philips X'Pert X-ray source, stage, and detector. Precise linear and angular control combined with well characterized x-rays yield high quality structural data.

and troughs gives some relation to the film thickness t, given approximately by:

$$t \approx \lambda/(2\Delta\theta) \tag{3.2}$$

where $\Delta\theta$ is the width of a Kiessig fringe, the oscillation in the XRR signal and λ is the x-ray wavelength. Measurement of multiple films' thicknesses gives some indication of the relation of growth time to thickness.

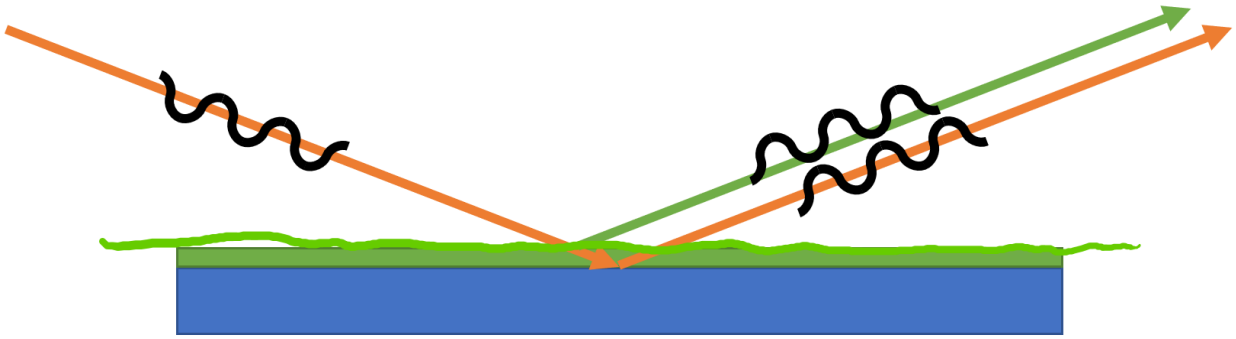

Figure 3.10: X-rays scattering off of a film surface and a film-substrate interface yield Kiessig fringes at low scattering angles indicative of the thickness and roughness of the films.

3.3.3 X-ray Fluorescence

X-ray fluorescence is useful to determine the relative presence of different elements in a sample by measuring a broad x-ray spectrum indicative of the typical elemental electronic energy scale differences. Inbound x-rays will excite electrons into higher energy states, which will then fluoresce characteristic x-ray frequencies as the electrons relax into lower states.

These characteristic x-rays can be located by comparing with known x-ray fluorescence tables, and their intensity can give an idea of the relative presence of the atoms. For this case, the relevant atoms would be Dysprosium and Titanium for thin films, since oxygen energy scales are outside the range of the detector, and Yttrium and Zirconium for the substrates.

3.3.4 Atomic Force Microscopy

Atomic force microscopy can measure the smoothness of the surface of a thin film. A thin film with a smooth surface should exhibit the reflectivity pattern from x-ray probes, but an AFM image can also show the uniformity of the surface smoothness. An Asylum AFM in contact mode was used to precisely map the surface of grown films to get an idea of the smoothness and uniformity of the film.

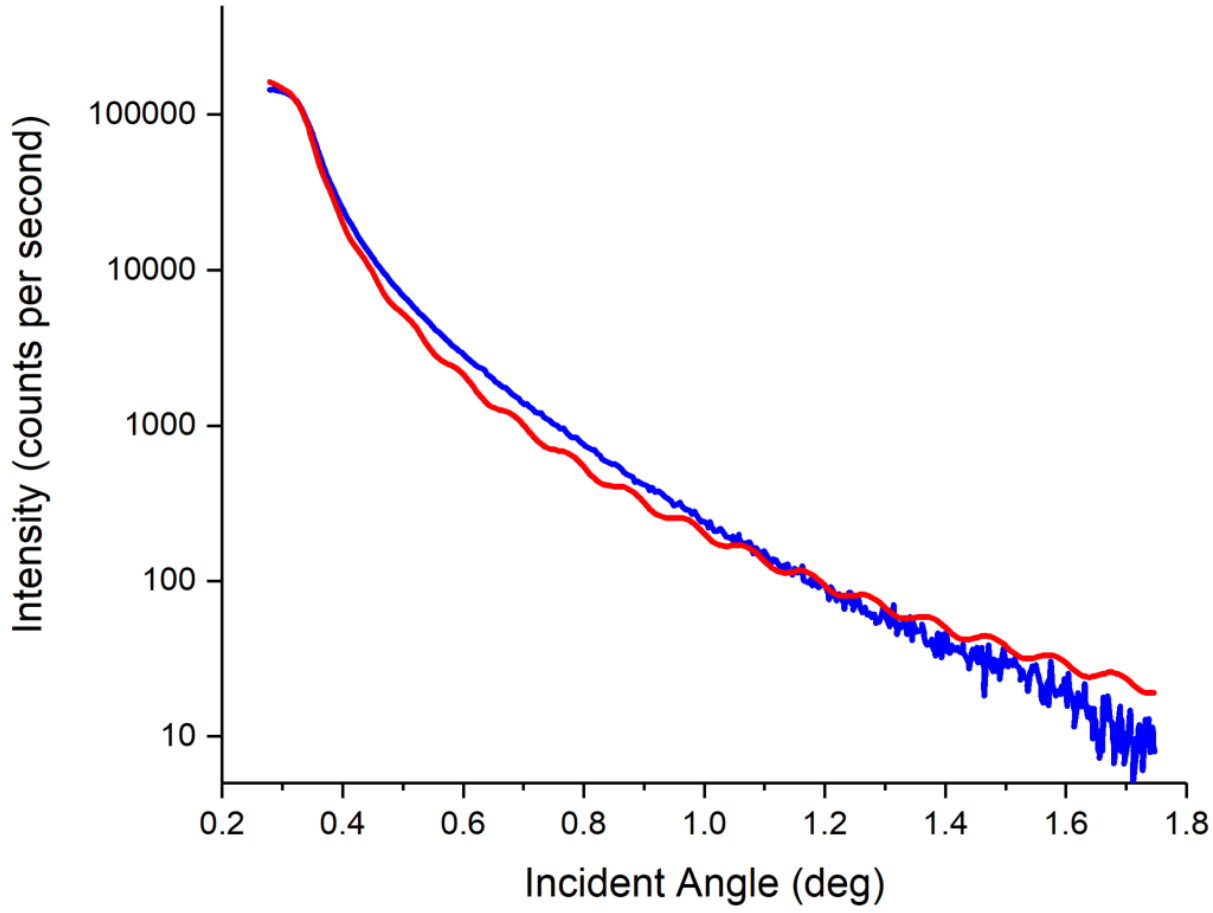

Figure 3.11: In blue, a rough surface is shown lacking any Kiessig fringes. In red, a fitting to Kiessig fringes of 40nm shows a characteristic oscillation on top of the longer scale decline.

3.4 Magnetic Probes

The unusual thermal behavior arises from the spin arrangement on the pyrochlore lattice. Once thermal measurements show the system behaves in a spin ice like manner on a regular pyrochlore lattice, the rich magnetic landscape found in $Dy_2Ti_2O_7$ can be probed. Effects of directionality, dimensionality, and extreme temperature and field behaviors on the spin ice state can be probed, as well as the mobility, creation, pinning, and persistence of the monopole quasiparticle excitations. There are three magnetic probes available, and the third of these will be treated separately as there are clever ways in which it can be used.

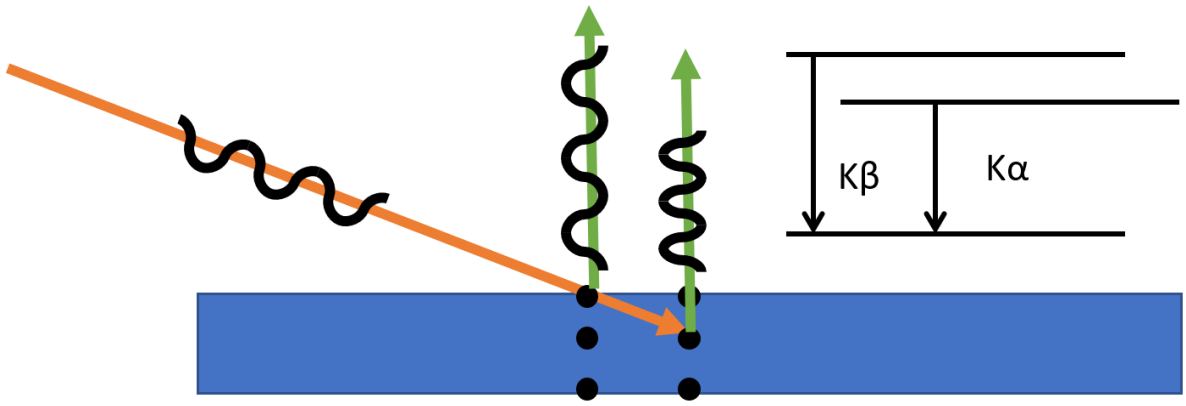

Figure 3.12: X-ray Fluorescence relies on the unique pattern of energy level relaxation in each element to determine the elemental content of materials. In this case, we were able to use the different energy level relaxation x-rays from Yttrium, Zirconium, Dysprosium, and Titanium to determine the content of each in our thin film deposition.

3.4.1 Magnetization

The magnetization of $Dy_2Ti_2O_7$ is a direction dependent measurement technique. Because of the complex magnetic and thermal phase diagram of $Dy_2Ti_2O_7$, characterization using magnetization requires known directions precisely. Prior work [30] has indicated that magnetization may be affected additionally by the shape of the material and a necessary demagnetization correction must be applied. Furthermore, that same work implies that signatures of the spin ice correlations emerge at temperatures above the onset of the spin ice state itself.

Magnetization data was taken in a Dynacool Magnetic Property Measurement System (MPMS), a "cryogen-free" cryostat cooled by high purity helium gas run through a compressor.

3.4.2 AC Susceptibility

AC susceptibility is a measure of the in-phase and out-of-phase magnetic response to an applied sinusoidal magnetic field. By adding a small sinusoidal field on top of a large constant field offset, we can probe the components of the magnetic field which respond directly to the externally applied field versus which respond to the internally created field as we move

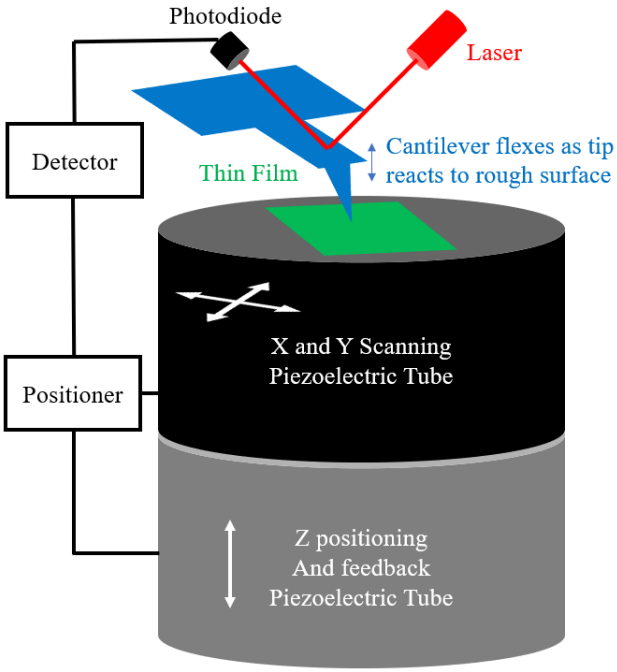

Figure 3.13: An atomic force microscope consists of a cantilevered narrow tip which can be dragged along a surface while its displacement is measured with a laser interferometer or other precise method. A piezoelectric scanner moves the sample beneath the tip, and the probe undergoes a force from the surface. As the tip approaches the surface, it first experiences a regime of attractive force, followed by increasingly repulsive force as the tip-sample distance decreases.

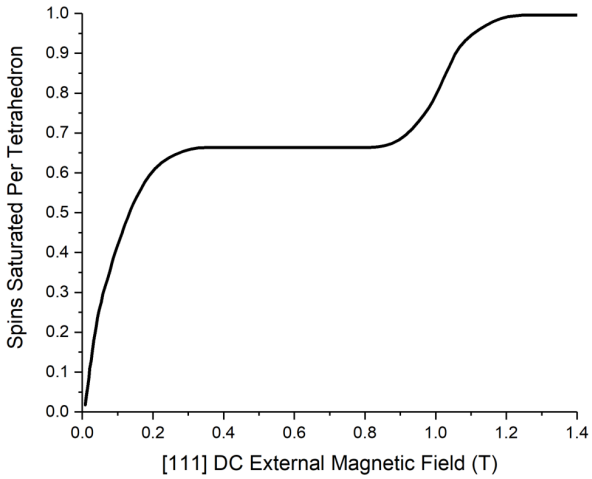

Figure 3.14: A typical curve for magnetization in the 111 direction in the spin ice regime, with a double plateau structure indication stable phases in the kagome ice and saturated ice states. [17] [74]

through the spin ice phase diagram. [75]

$$\chi = dM/dH = \chi' + \chi'' \tag{3.3}$$

An AC susceptibility setup consists of a set of concentric solenoids, with a coil to apply a small AC excitation on top of a large DC field supplied by a superconducting magnet in a PPMS. The other concentric solenoid then acts as a detector via Lenz's law. Furthermore because it is an AC measurement, both the in-phase (χ') and out-of-phase (χ'') response can be measured. These quantities are connected by the Kramers-Kronig relations. [76] This is significant because the out-of-phase component correlates with the effects of the internal field caused by the magnetic ordering. While the in-phase component directly relates to the size of the external field applied on the spins, the out-of-phase component demonstrates how the system relaxes on the timescale of the AC signal.

3.5 Superconducting Quantum Interference Devices (SQUIDs)

A superconducting quantum interference device is a sensitive magnetic flux to voltage converter. Because very sensitive electronic methods and equipment to measure voltage exist, therefore sensitivities on the order of $10^{-9}\phi_0$ per Hz exist for magnetic flux measurements. This is accomplished in the following way:

A Josephson Junction (JJ) is a non-superconducting gap between two superconducting leads. The Josephson relation describes the voltage across the junction as a function of the difference in superconducting phase between the two leads. A SQUID consists of a loop of superconducting wire with two JJs, and any magnetic flux passing through the loop induces a current in the loop, and hence a change in voltage across the junctions. An inductively coupled readout circuit enables a voltage measure of the SQUID effect.

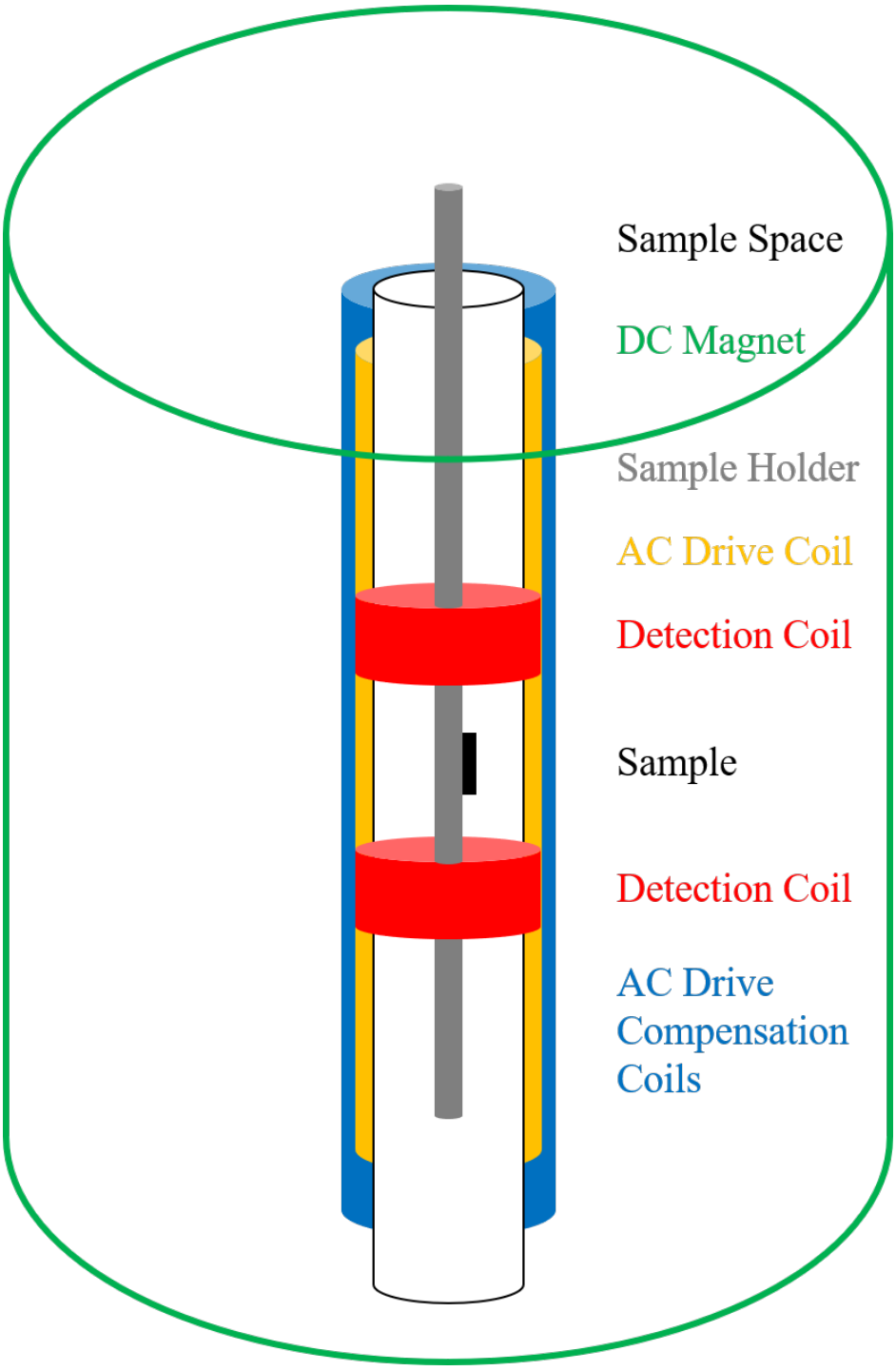

Figure 3.15: A concentric set of magnetic coils drives an AC field on top of any DC field applied via an external superconducting magnet. The detection coils then generate a current when flux from the sample causes a differential dipole field in the upper and lower coil, which can then be decomposed into in-phase and out-of-phase responses to the applied AC frequency. A central thermometer carefully measures the sample temperature.

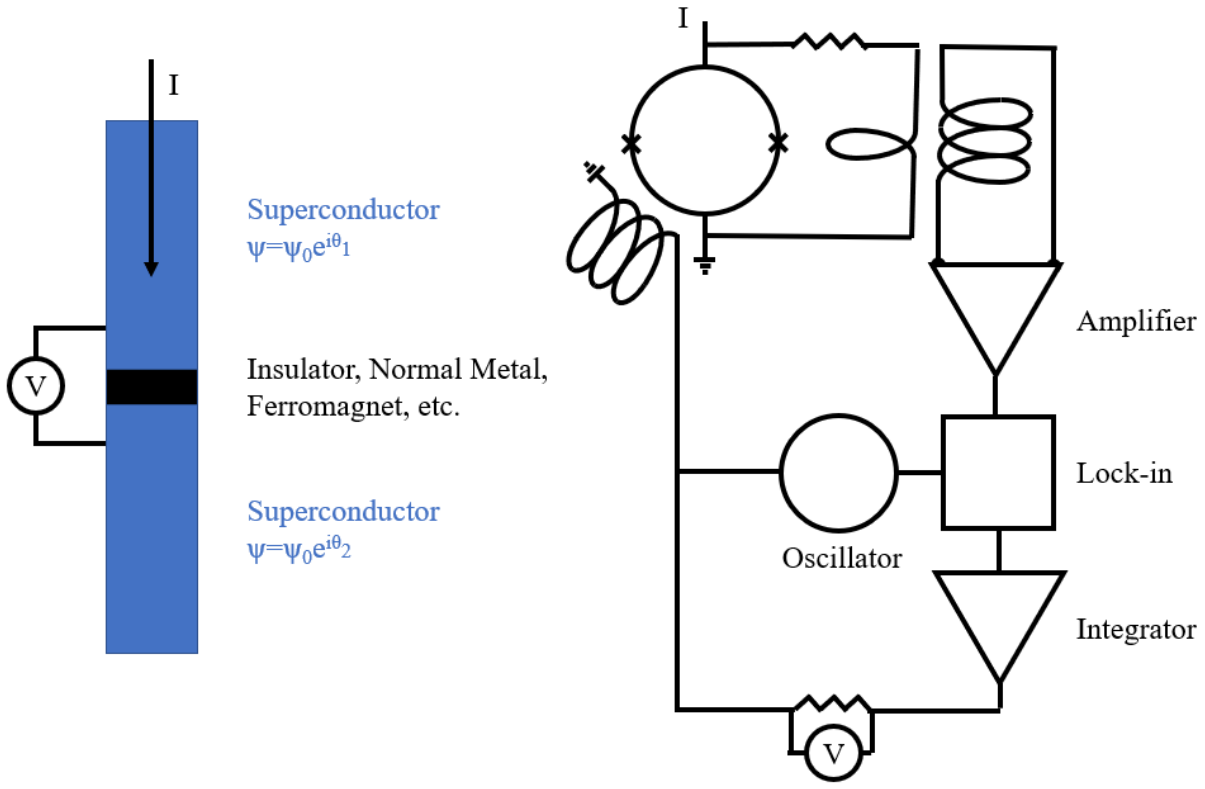

Figure 3.16: Left: A current I passes through an insulating gap in a superconducting channel, called a Josephson Junction. The voltage across the gap winds with the difference of the superconducting phase, θ. Right: A diagram of a practical SQUID readout circuit contains a pair of Josephson Junctions in a loop, an inductively coupled feedback loop to readout the SQUID voltage and keep the SQUID in the linear voltage regime (see Figure 3.17), and an inductively coupled pickup loop to provide the signal from a remote source. [77]

With a feedback coil, we can maintain a linear response to the applied flux, and that offset is what is measured. A flux-locked SQUID in practice then can be optimized by setting the inductance of the pickup loop equal to the inductance of the SQUID.

In operation, the SQUID in use is a STAR Cryo commercial SQUID with PCS100 software. The SQUID is printed on a PC board and is housed within a lead shielded screwcap container, connected to the external electronics with a shielded "cryocable" consisting of a coaxial cable thermally sunk to the cryostat at three places within the cryostat, while a pickup loop is inductively coupled to the SQUID fed through a lead shielded input line to within a few millimeters of the SQUID.

The cryostat in use is an Oxford Triton dry dilution refrigerator, which uses a closed cycle helium-4 and helium-3 mixture to cool to a base temperature of about 20mK. This base temperature is obtained at the bottom of six plates within a light and air tight vacuum shield system. These plates are connected by poor thermal conductors, stainless steel or a polymer like G10, and they allow for radiation, conduction, and convection separation as a system of compression and evaporation cooling allows the plates to achieve a succession of lower and lower temperatures. The SQUID is thermally anchored to a plate with a base temperature of 100 mK, while its heatsinks are anchored to plates with base temperatures of 600mK, 4K, and 10K.

In addition to reading out directly the voltage and hence magnetic flux passing through a SQUID, the SQUID magnetometer has a characteristic noise profile, consisting of a low frequency 1/f noise region and a high frequency white noise region. [79] Thus we can characterize the background SQUID noise with a simple crossover frequency where the 1/f noise region and the white noise region meet. The background white noise level gives a measure of the overall sensitivity of the SQUID, and a comparison with other magnetic probes such as scanning hall probes or magneto-optics as in [80] shows that a SQUID achieves the lowest field sensitivity, and a spatial resolution limited in comparison to magnetic force microscopy or electron microscopy mostly by how small of a pickup loop area one can create.

To take advantage of the sensitive SQUID magnetometer, we sought to create a clever experimental setup to isolate the monopolar field and probe the monopolar dynamics as defects propagate amid the spin ice state. To do this, we first took advantage of the superexponential dependence of monopole density on temperature. This should allow us to create a gradient of monopole density with a well-chosen thermal gradient. In this case, the density of both species at any point should be the same. Second, different species of monopole charges should respond to an applied magnetic field the same way as electrons and positrons would respond to an electric field. Thus a magnetic field applied to a pair of defects should drive the defects further apart along the applied field. In a uniform distribu-

tion of monopole charges, this should not have any effect as on average the density of each species does not change. However, a combination of the two conditions should produce a region with a difference in species density as we drive one species from a region with higher density of one species into a region of lower density of the other species. This temperature gradient and applied field effect should allow us to obtain an extra monopolar contribution to the field detected as coming from the sample. With the high sensitivity of the SQUID, low spatial resolution of the pickup loop, superexponential decay of monopole density with temperature, and high mobility of the monopole defects, we think that in an ideal case we would be able to get a direct probe of the magnetic nature of the monopole quasiparticles in spin ice.

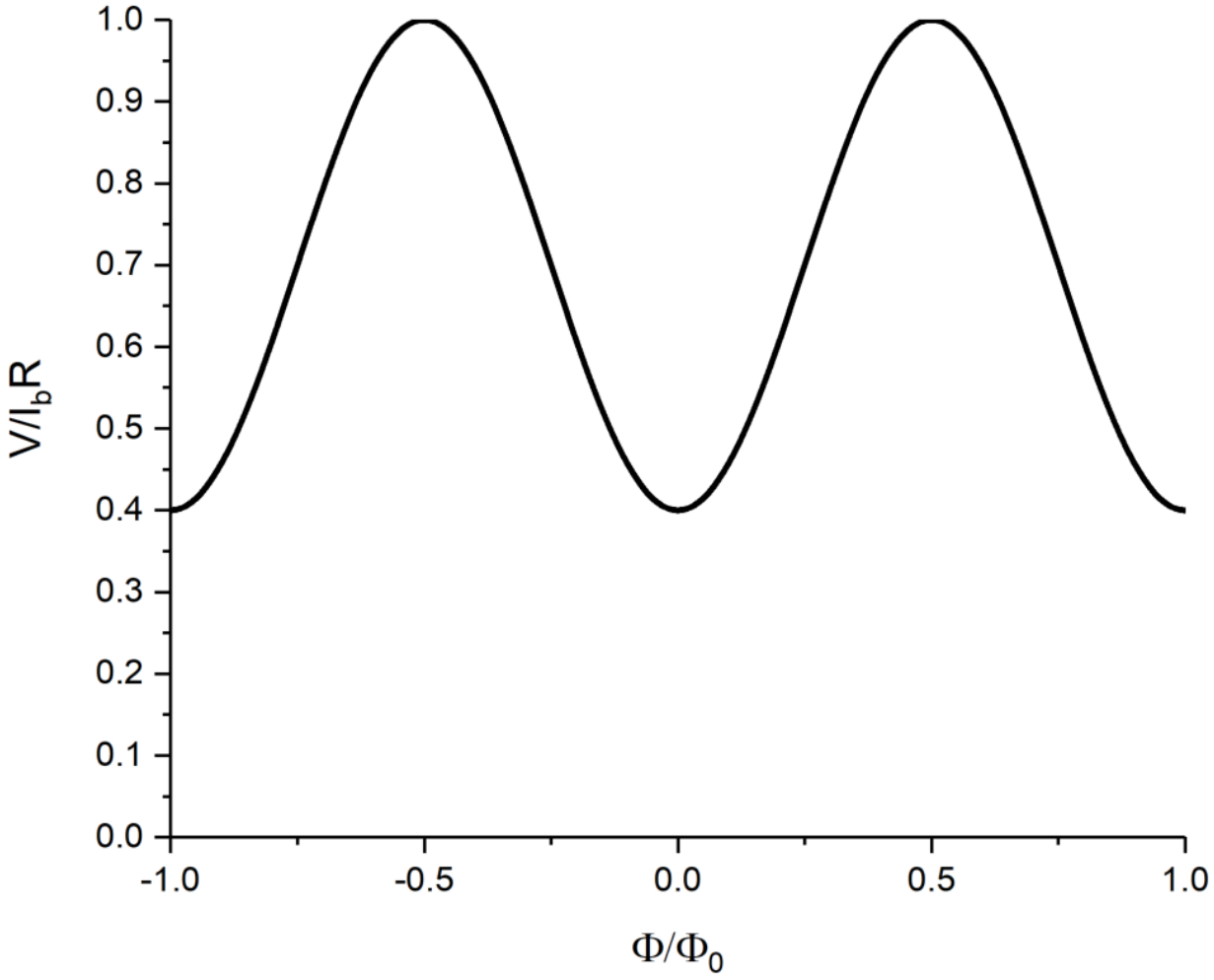

Figure 3.17: A SQUID voltage versus flux though the superconducting loop diagram yields a sinusoidal response for an SIS junction. By inductively coupling a tunable loop, we can maintain the SQUID voltage in the linear regime (midway between peaks where small changes in flux yield an approximately linear change in voltage), and create a sensitive magnetometer. [77]

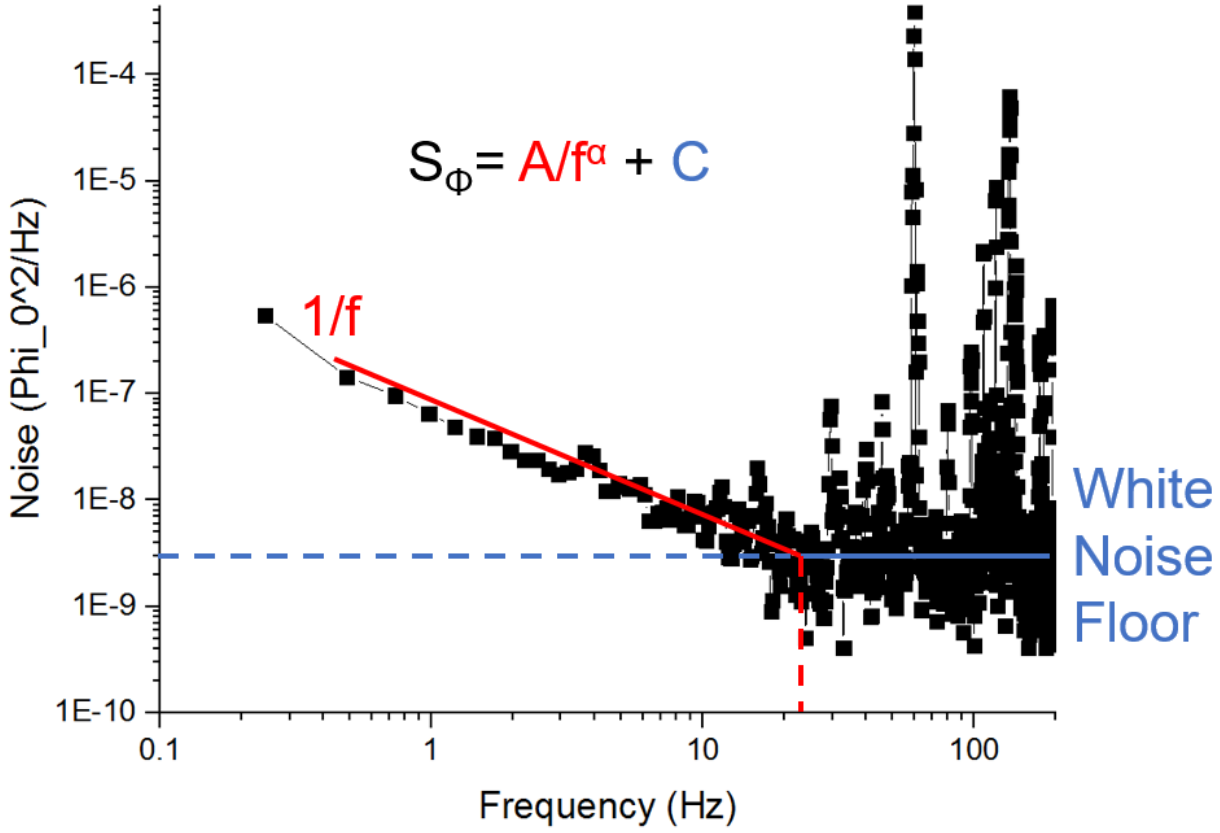

Figure 3.18: In addition to the SQUID voltage signal, we can also examine the power spectral density of the SQUID flux noise. A bare SQUID yields a 1/f low frequency regime and a white noise high frequency floor. This characteristic noise profile can be characterized by a single point: the crossover frequency. [78]

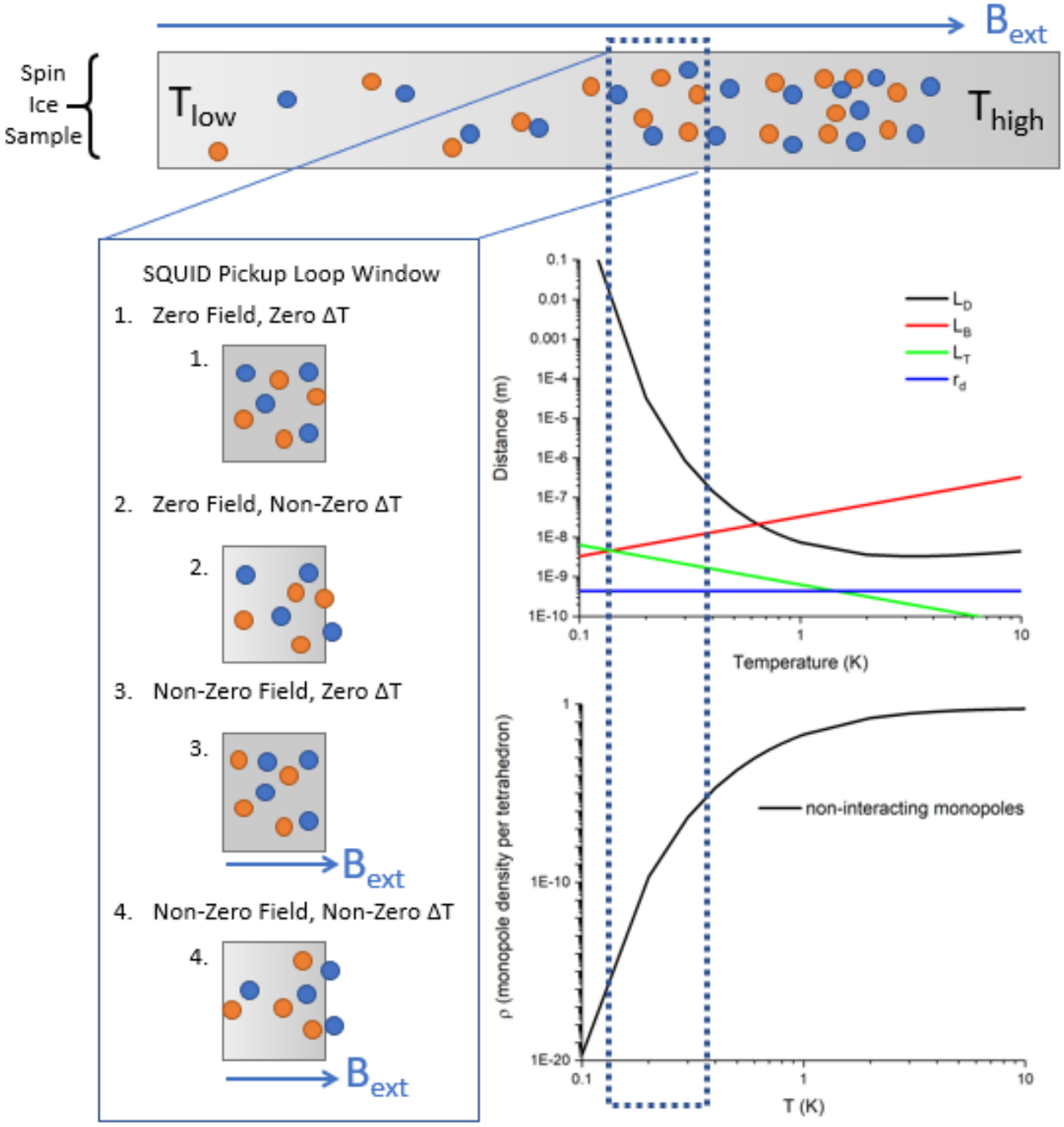

Figure 3.19: At top, a spin ice crystal is shown in gray under the influence of an applied thermal gradient and magnetic field. At left, a non-zero net monopole charge density is created in the SQUID pickup loop window (dashed area) in the following way: (1) A DTO crystal is cooled into the spin ice regime with a dilute defect density of opposite pairs of monopoles. (2) An applied thermal gradient (shown as a grayscale gradient) will cause a superexponential differential density of defect pairs as shown in the top graph at right. [65] (3) Independently, an applied magnetic field will drive pairs of monopole in different directions further apart, as shown in the length scale plot below right. (4) However, applying both a thermal gradient and field will drive different densities of opposite monopole charges into the same area, inducing a net effective monopole field detectable by the SQUID pickup loop.

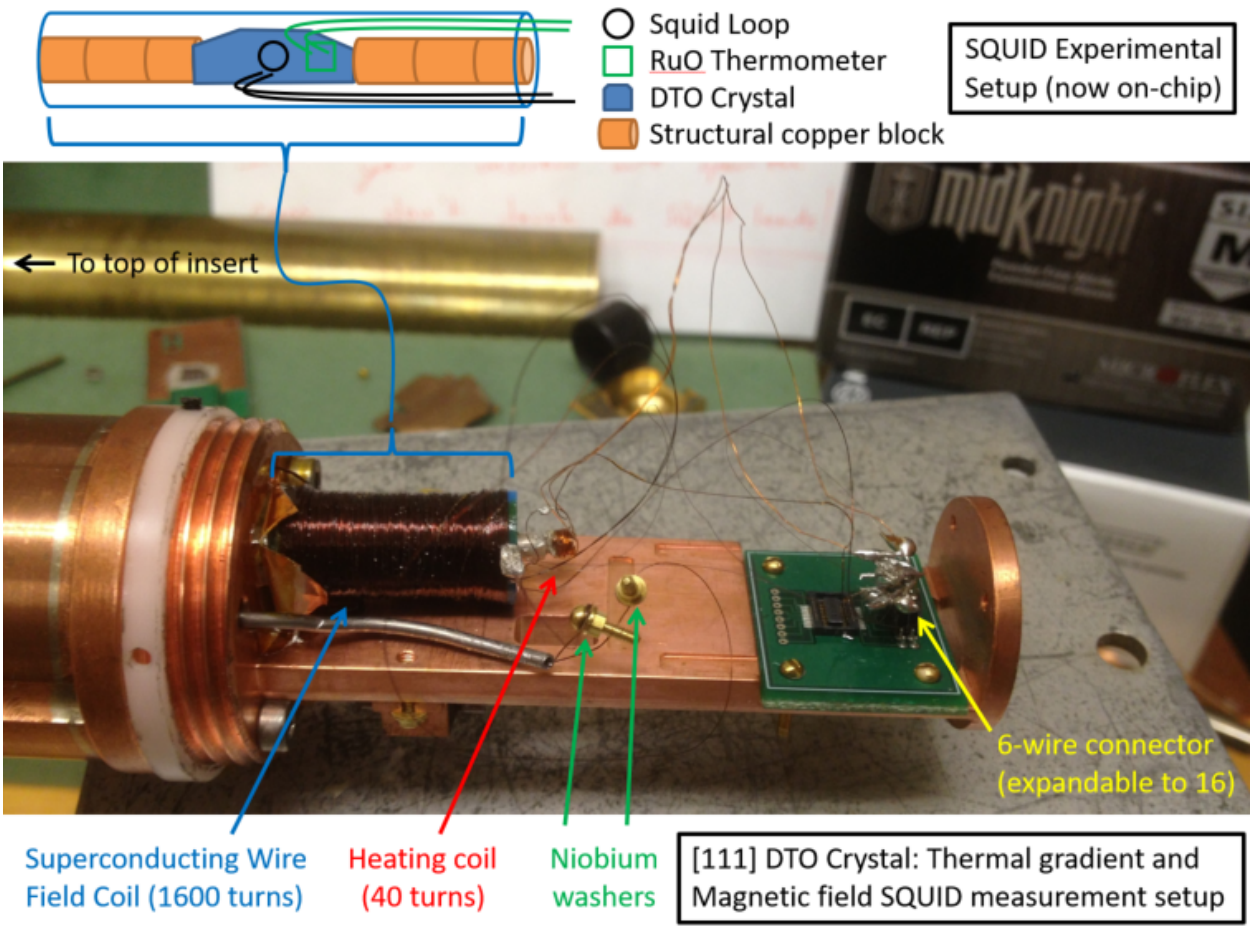

Figure 3.20: The diagram in Figure 3.19 is realized initially in a He-3 cryostat, and later with the ability to remove and replace the sample in a He-3/He-4 dilution refrigerator. The setup is capable of creating the necessary linear field though the solenoid and thermal gradient with a counterwound coil on one end and a PID controlled thermal anchor on the other. A SQUID coil is placed on or near the surface of the crystal, all within the solenoid.

Figure 3.21: Attached to the mixing chamber plate of the dilution refrigerator are concentric copper, mumetal, and lead shields to expel external magnetic flux and create a uniform radiation temperature environment. Within one of these shield setups is a SQUID magnetometer as pictured in 3.20.

Chapter 4

Crystalline $Dy_2Ti_2O_7$ Oxygen Effects

In this chapter, the effect of different oxygen atmosphere growth conditions on the crystal structure and magnetic and thermal behavior of $Dy_2Ti_2O_7$ was probed. Systematic changes in structure and behavior indicative of changes to the crystal or spin ice state order were studied as a result of the presence of oxygen vacancies.

4.1 Structural Characterization

$Dy_2Ti_2O_7$ crystals were grown in a floating zone furnace from prepared powders of $Dy_2Ti_2O_7$ under four different growth conditions in an overpressure of high purity O_2 gas: 2.5 atm, 5 atm, 7.5 atm, and 9 atm. Single crystals resulting from these growths were cylindrical around 5 cm in length and 5 mm in diameter. From these crystals we cut several samples oriented along relevant crystal directions for the magnetic sublattice, namely [100], [110], and [111]. These samples were oriented using a Laue x-ray diffraction pattern and cut using a wire saw. The resulting samples ranged from rectangular prisms measuring around 1 cm in length and 2 mm by 2 mm in cross-section to less straightforward shapes including needles and samples with one flat face and other rounded edges. These shapes merely resulted from cutting the largest possible samples oriented in the appropriate directions given the fact that the grown single crystals had a single orientation along their length. For the measurements presented here, the shape of the crystal and the associated demagnetization correction effects should not significantly alter the important derived quantities.

One sample in each direction from each growth condition (for a total of twelve separate

Identifier	**Pressure**	**Dir.**	**Label**	**Mass(mg)**	**Vol.(mm^3)**	**Shape**	**Color**
2D111AT1	Pre-existing	111	n/a	120.8		rectangular column	opaque brown
2D111AT2	2.5 atm	111	1	8.5			transparent yellow
2D111AT3	2.5 atm	111	2	30	5.4	square pillar	transparent yellow
2D111AT4	2.5 atm	111	3	42.8	6.732	square pillar	transparent yellow
2D111AT5	2.5 atm	111	4	5.2			transparent yellow
2D111AT6	2.5 atm	111	5	12.7		triangular wedge	transparent yellow
2D111AT7	2.5 atm	111	6	2.8		triangular wedge	transparent yellow
2D110AT1	2.5 atm	110	1	31.3	4.128	square pillar	transparent yellow
2D110AT2	2.5 atm	110	2	23	2.93	triangular wedge	transparent yellow
2D110AT3	2.5 atm	110	3	16.7	2.1	triangular wedge	transparent yellow
2D110AT4	2.5 atm	110	4	12.2	1.5	triangular wedge	transparent yellow
2D110AT5	2.5 atm	110	5	6.5	1.8	triangular wedge	transparent yellow
2D110AT6	2.5 atm	110	6	4.01	0.4	triangular wedge	transparent yellow
2D110AT7	2.5 atm	110	7	3.3	0.9	square pillar	transparent yellow
2D110AT8	2.5 atm	110	8	2.6	0.4	triangular wedge	transparent yellow
2D100AT1	2.5 atm	100	1	15.7	3.17	quarter ellipse	transparent yellow
2D100AT2	2.5 atm	100	2	8	5.6	trapezoidal pillar	transparent yellow
2D100AT3	2.5 atm	100	3	5.6	0.896	triangular wedge	transparent yellow
2D100AT4	2.5 atm	100	4	4.7	1.116	quarter ellipse	transparent yellow
5D111AT1	5 atm	111		16.3		oblique cylinder	light trans. yellow
5D110AT1	5 atm	110		4.5		triangular wedge	dark trans. yellow
5D100AT1	5 atm	100		8.6		disk	light trans. yellow
7D111AT1	7 atm	111		8.5		disk	transparent brown
7D110AT1	7 atm	110		8.9		disk	transparent brown
7D100AT1	7 atm	100		11.9		cylinder	transparent brown
9D111AT1	9.5 atm	111		32.3		oblique cylinder	transparent yellow
9D111AT2	9.5 atm	111		64.5		semi-cylinder	transparent brown
9D110AT1	9.5 atm	110		8		slanted disk	transparent brown
9D100AT1	9.5 atm	100		10.6		disk	transparent brown

Table 4.1: An inventory of the DTO samples grown.

samples) were then subject to x-ray diffraction studies in a Philips X'pert device. A theta-2theta scan was conducted broadly then narrowly to determine the lattice constant for the crystal samples. As seen in Figure 4.1, the nine samples were probed in three different crystal lattice angle peaks, corresponding to the [222], [400], and [440] peaks. In the figures, the amplitudes are normalized to 1 since the measurement time and hence scattering intensity varied and the figure of merit is the angular peak location. The significant feature is the systematic spread of the peak angles as a function of the growth condition. From the data we can calculate the lattice constant a for each case: For 2.5 atm, $a = 1.021 \pm .007$ nm, for 5 atm $a = 1.014 \pm .003$ nm, for 7.5 atm $a = 1.012 \pm .002$ nm, and for 9.5 atm $a = 1.010 \pm .001$ nm.

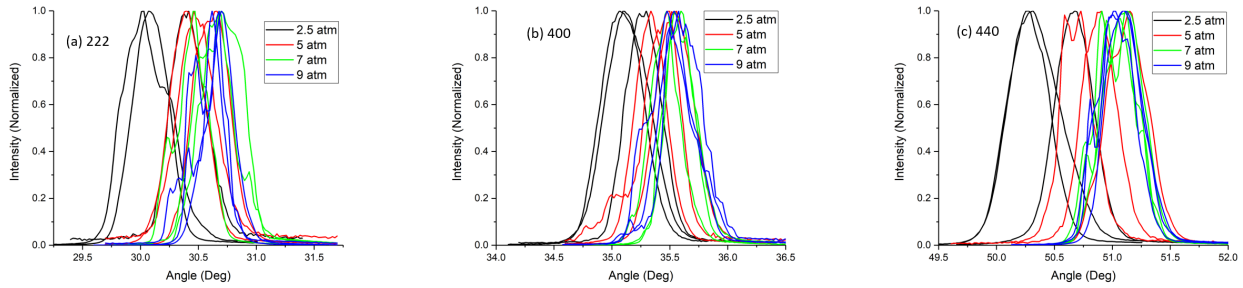

Figure 4.1: Theta-2Theta scans of DTO crystals grown at various oxygen pressures. The variation in peak location indicates a variation in crystal density, and hence a variation in crystal structure.

Several trends are important to note from the theta-2theta scan:

The first is that these values span around prior literature values of expected $Dy_2Ti_2O_7$ values, between about 1.01 and 1.02 nm. [10] This is approximately represented by a solid back line in Figure 4.4. We will see later that other properties similarly range both above and below expected values for these materials.

Prior work [10] saw that annealing caused a decrease in lattice spacing. In our work, we can add to that that increasing the oxygen pressure during growth has caused a decrease in lattice constant, in the following way:

The error in the measurement, or the range over which peaks were seen, also dropped

significantly as we increased the oxygen growth condition. This may indicate that the presence of oxygen vacancies in the samples is nonuniform - that some areas of the sample grown have a larger number of vacancies, and hence a larger lattice constant, but others do not. This inconsistency is a further confounding variable in measurements in spin ice crystals - not only do the vacancies act as pinning sites to slow spin dynamics and inhibit equilibrium, variations in vacancy density would cause inconsistent thermal and magnetic measurements even given the same lower oxygen growth conditions.

Some notable trends across all samples include the fact that many samples seem to have additional peaks on the sides of the main peak. If we are to assume that these peaks arise from the same sort of oxygen defects as which cause the variation in the peak location, then we can see that these cut samples even within themselves can contain variations in lattice parameter. More detailed crystallographic study may elucidate the particular defect density finite size effect.

Also, the widths of the peaks as a function of growth condition do not seem to change systematically. This may be due to the inconsistency of growth techniques.

Further, we can reduce the error for the data points from each of our samples by recognizing that any zero-point angular slop in the positioning of the instrument can be subtracted off by a linear fit to the expected Bragg peak locations. Since each measurement is taken along a different crystal axis, the three data points can be fit to a line whose axis-crossing will be offset from zero by the amount of the slop. An example from our data using the 2.5 atm sample is shown in Figure 4.3, with an intercept outside of its goodness of fit away from zero. This means that we can subtract this value from the peak location and recalculate the lattice parameter. These values are shown in Figure 4.4, where it's seen that the 2.5 atm lattice parameter values are now within the error of each other. This makes sense because all the measurements were taken from the same crystal sample in the same run, just at different directions. Furthermore the correction leaves the 2.5 atm sample still in the largest lattice parameter position. This is again consistent with the rest of our data and with prior data.

In this way, we sought to vary the number of oxygen defects in a systematic way, and then we examined the effects of such defects on the thermal and magnetic properties characteristic of the spin ice state.

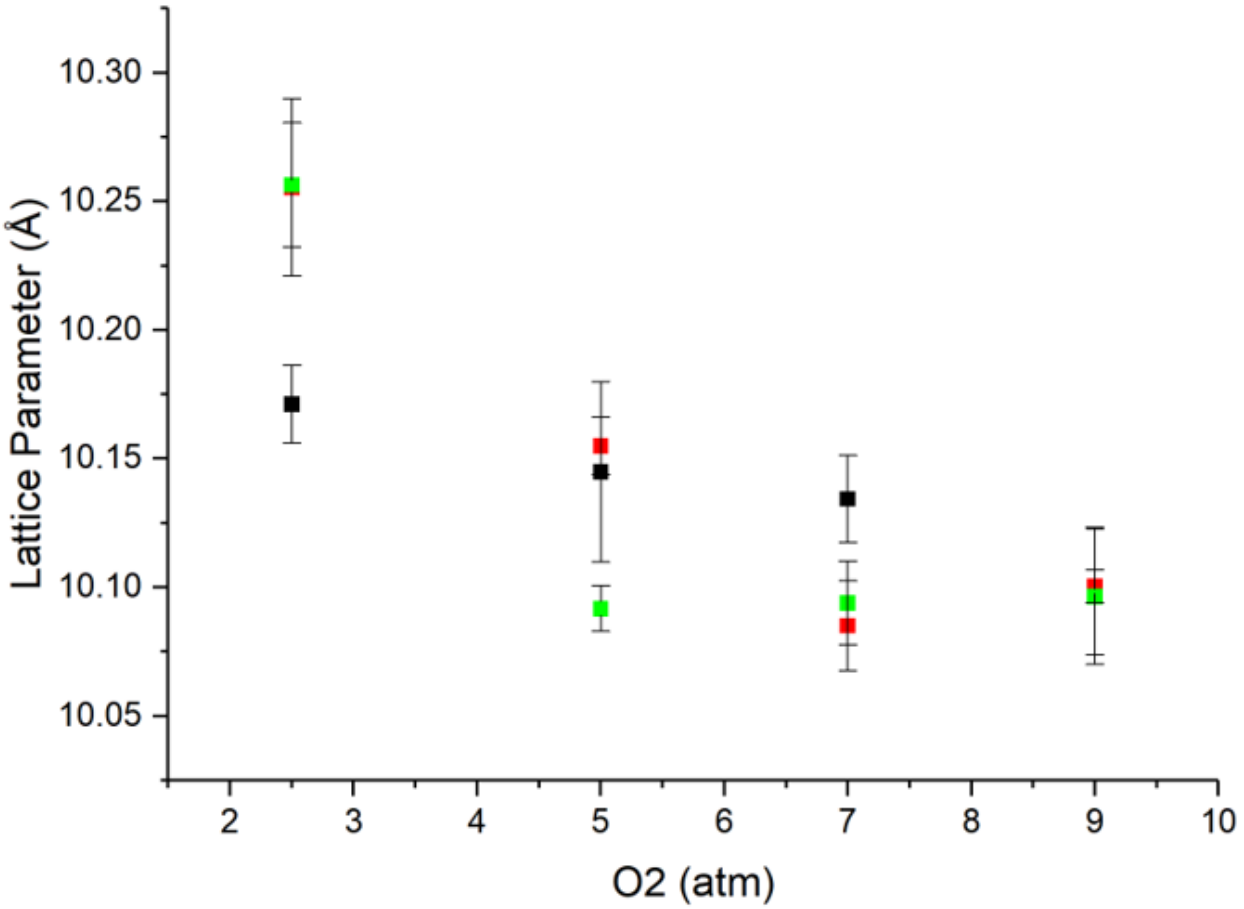

Figure 4.2: Extracted lattice parameters from the XRD data an overall trend decreasing as the oxygen growth pressure increases, however there are also wide variations within each growth condition.

4.2 Thermal Trends

The spin ice state is marked by the presence of residual Pauling Entropy at low temperatures, and so we measured the heat capacity of one sample from each growth condition to integrate the entropy and compare to the theoretically expected value.

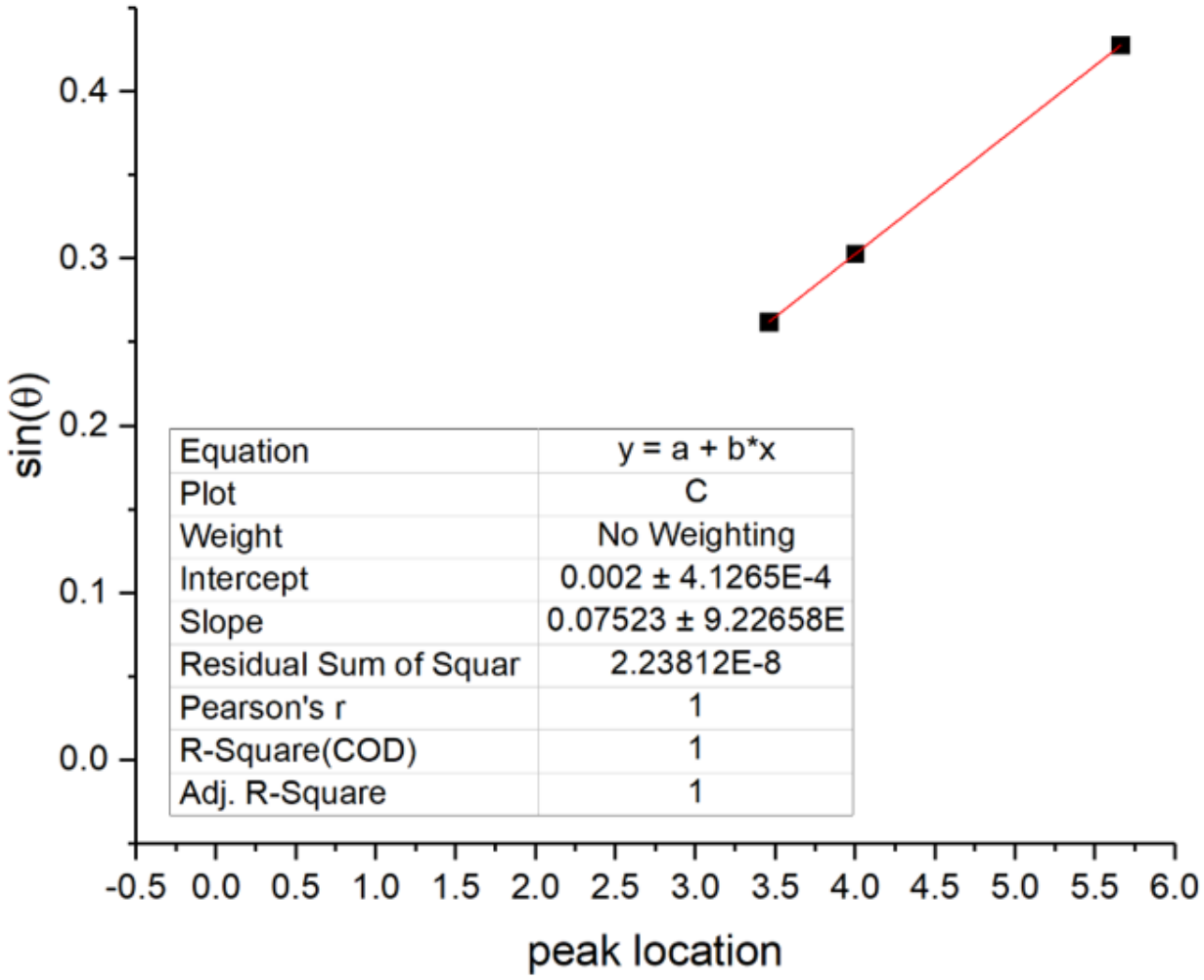

Figure 4.3: A linear regression of peaks within the same samples yields a measure of a zero-point angular offset slop within the Philip X'Pert 2, which may be a source of separation of measurements within each sample.

To measure the heat capacity, we used a Quantum Design Physical Property Measurement System. A small sample from each growth condition was placed on a well calibrated thermal stage, on which the temperature may be measured carefully as heat is introduced to and diffused by the sample. The measurement of the heat pulses is fitted to a "two tau" model, allowing for two different characteristic time scales over which the sample may absorb or diffuse heat. From this fitting we get an overall value for the heat capacity of the sample and measurement system.

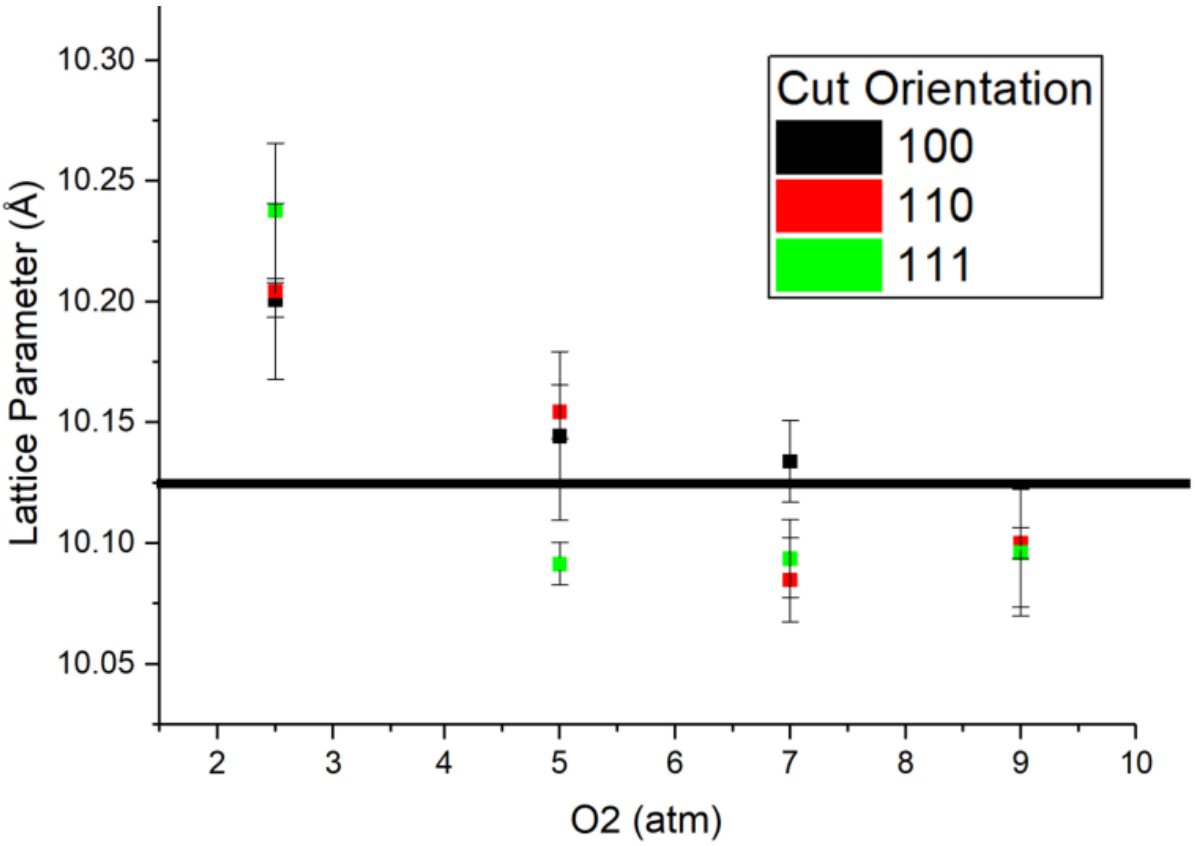

Figure 4.4: Compare the 2.5 atm case here to the one in 4.2 to see how correcting for the zero-point offset can bring the lattice parameters for a sample within error of each other, but not of the other growth conditions, helping to validate the trend. The black line at 1.0125nm represents a typical literature value for the lattice parameter of dysprosium titanate.

Subtracting off background contributions to the heat capacity yields solely the contribution from the sample. The sample itself has several contributions to the heat capacity: nuclear, magnetic, and phononic. We can subtract off the phononic contribution by fitting the high temperature data to the low-temperature limit of Debye phonon theory, such that $C \propto T^3$, leaving the magnetic and nuclear degrees of freedom to contribute. For $Dy_2Ti_2O_7$, the nuclear heat capacity increases very sharply at temperatures lower than our study (0.15K). For our purposes then, we can ignore the nuclear contribution to the heat capacity, and treat the data as shown in Figure 4.5 as if it is entirely due to the magnetic contribution to the heat capacity.

The heat capacity can then be integrated to get a measure of the entropy in the system.

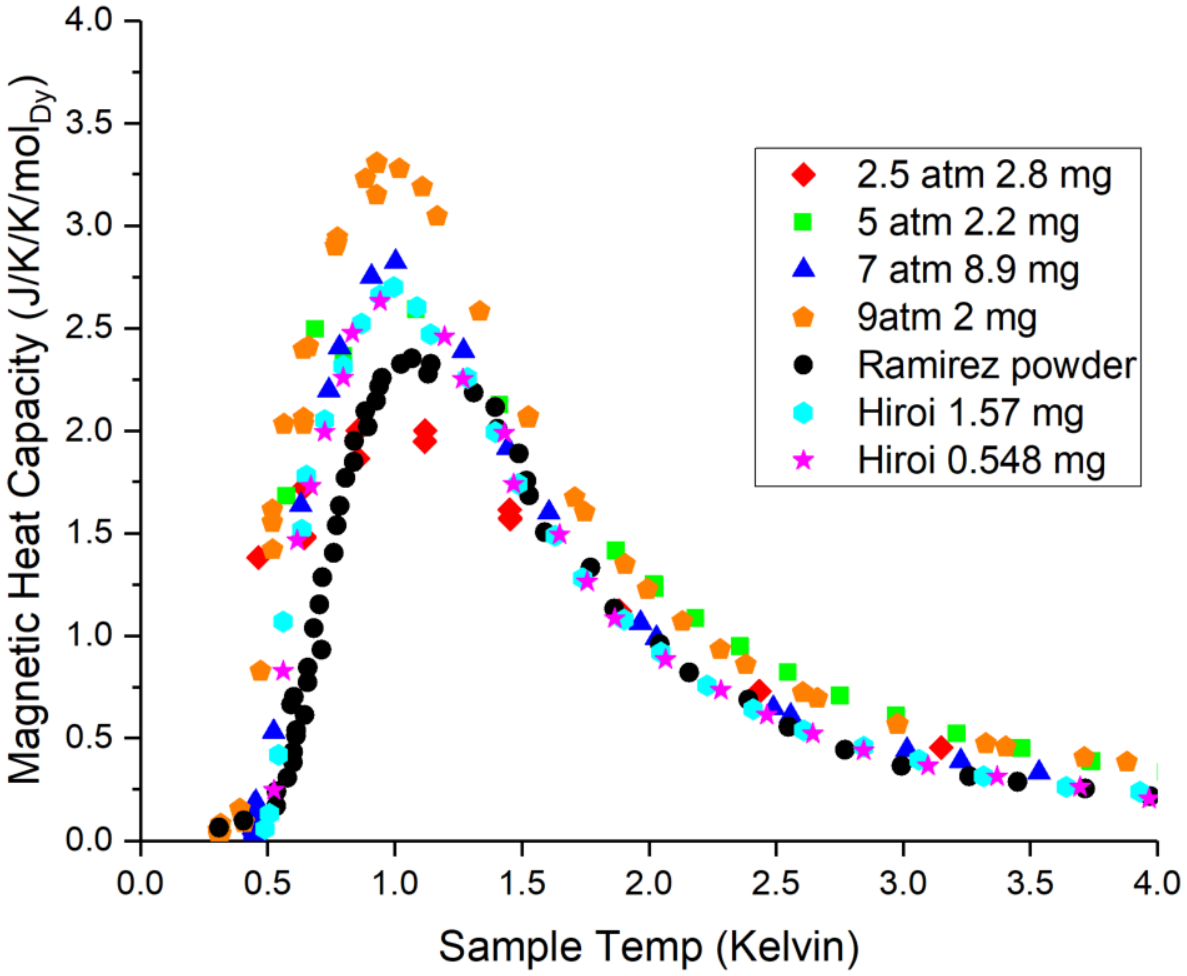

Figure 4.5: Heat capacity over temperature per Dy spin versus temperature measurements for small crystals of $Dy_2Ti_2O_7$.

The magnetic contribution to the heat capacity in $Dy_2Ti_2O_7$ stems entirely from the configurational ordering in the spin ice state. Indeed, we see that as the system enters into the spin ice state regime, we get a peak in the magnetic heat capacity indicative of the establishment of a "two in two out" state. This theoretically should account for the Pauling entropy at low temperatures.

In the heat capacity and entropy, we notice several trends in the data:

The first is that the values again range around the expected value for a spin ice material, namely $(1/2)\log(3/2)$, the Pauling Entropy. Subtracted from the overall available configu-

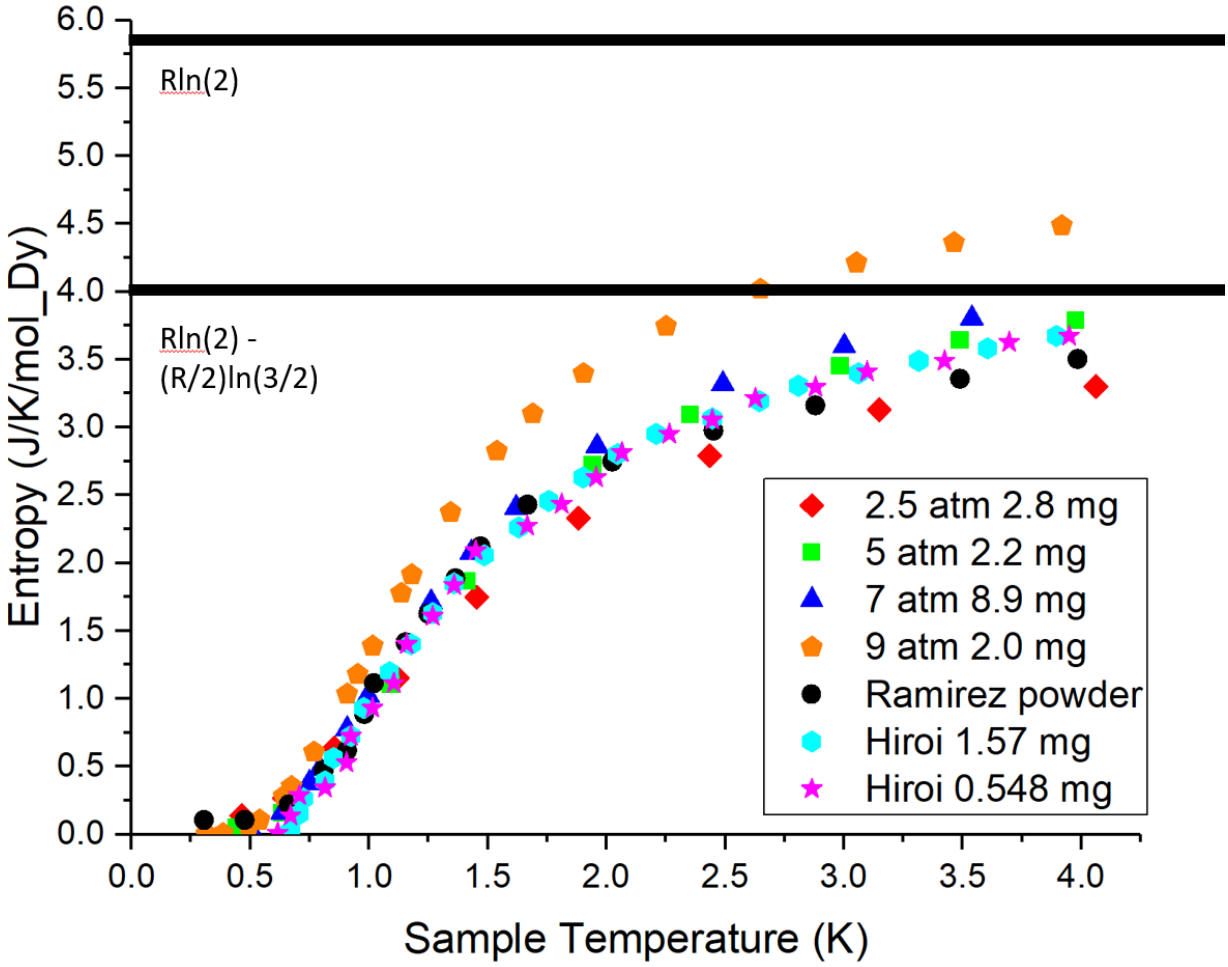

Figure 4.6: Entropy per Dy spin versus temperature measurements for small crystals of $Dy_2Ti_2O_7$.

rational entropy, we see variation around the expected value of 4.08 J/K/K/molDy. We see that with increasing oxygen growth condition, we get an increasing value of entropy, and hence recover an increasing amount of the residual Pauling entropy.

The general form for the heat capacity peak in a system such as this where each spin has just two available states is the generalized Schottky Anomaly as we saw in 2.

$$\frac{C_m}{k_B} = \frac{(g_1/g_0)(\beta\Delta)^2}{(e^{\beta\Delta/2} + (g_1/g_0)e^{\beta\Delta/2})^2} \tag{4.1}$$

The g factors in the above equation refer to the relative degeneracy of the ground and first excited state, in our case, where we have 0 or 1 defect in the spin ice "two in two out"

pattern. The value of Delta is a measure of the energy gap between these two states. For our data, the best fit is attained when the value for Delta remains fairly constant, while the g factors vary. This fit follows the trends seen in the data - the peak height changes significantly but not the peak temperature. In contrast to the thin film study, which is better fit by changing the delta parameter of the fit, our data is better fit by changing the g factor, indicating a change in the relative degeneracy of the states.

Indeed, this behavior is just what we expect from oxygen vacancies. Pinning of spins changes the number of available configurations for that site, and also changes them differently for the spin ice state from the defect state. For example, the defect free ratio of the number of states in the ground state to the excited state is 6 to 8. Pinning one spin changes the number of states available but not their ratio, to 3 to 4. However multiple pinned spins does change the ratio in addition to the number, yield ratios of 1 or 2 depending on the pinned configuration.

What this indicates based on the fitted g factors (1.04, 1.19, 1.34, 1.63 for 2.5 atm, 5 atm, 7.5 atm, and 9.5 atm respectively) is that each of these samples has a collection of defect states, approaching that of the ideal spin ice, but then exceeding it, perhaps as excessive oxygen creates states where two spins are pinned aligned. All samples are well fitted by the same Delta parameter, 3.1 K, indicating that the Dy spins are in their same Ising state in all samples, and that the variation arises from disruptions to the usual freedom of these spins to flip and to order in a ferromagnetic way.

4.3 Magnetic Behavior

Due to the interesting systematic variation of the magnetic component of the heat capacity, magnetic properties of these samples were probed using ac susceptibility. [81] The ac susceptibility was measured using a Quantum Design Physical Property Measurement System, and a selection of data for one sample is shown in Figure 4.7. The 9 atm sample data

shown displays a characteristically varying peak in the out of phase component of the ac susceptibility as a function of the applied ac frequency. The out of phase component of the susceptibility gives us insight into the system magnetic relaxation times, shown in Figure 4.8. The inverse relationship between the maximum response frequency and the relaxation time tells us about how the dynamics of the system behave internally under and external field. The structure of the peak location change indicates that there are indeed the expected transitions out of a spin ice like state into a kagome ice state and then a saturated state. The difference between our samples in Figure 4.8 and prior data indicates that we see a significant change in relaxation time. [68, 82] Furthermore the Cole-Cole plot on the right indicates a deviation from the single-channel relaxation expected.

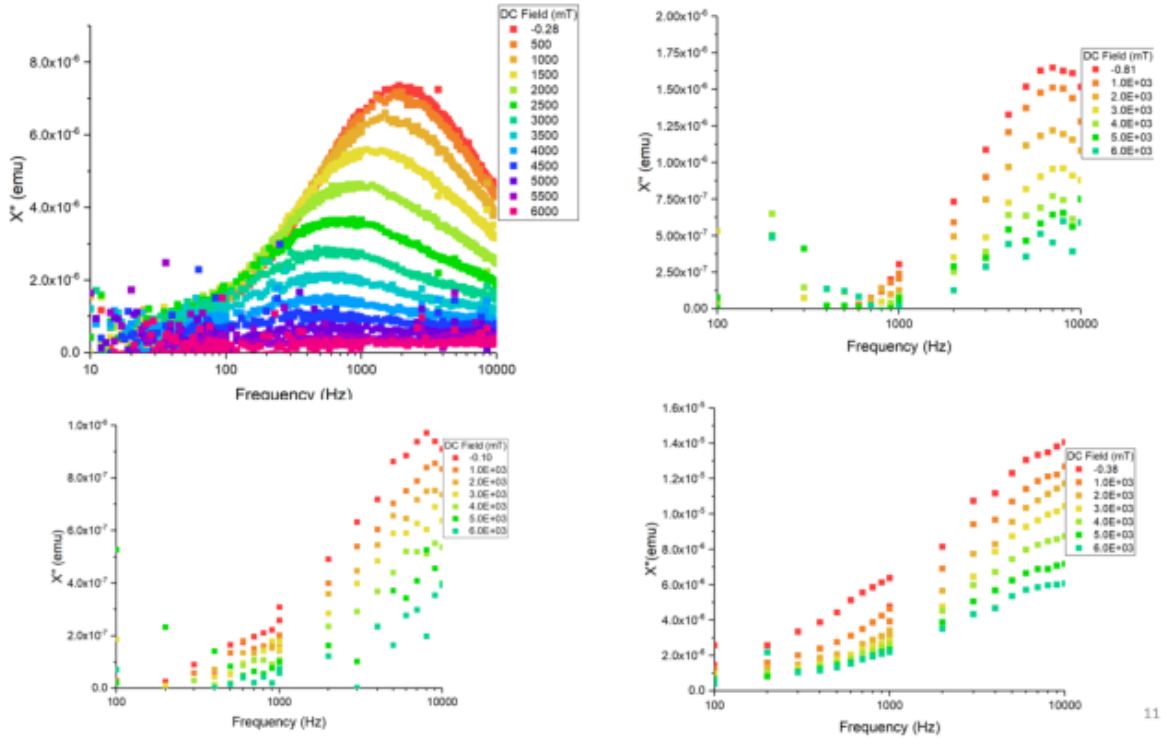

Figure 4.7: Clockwise from top left: The out-of-phase component of the magnetic ac susceptibility versus frequency for 9atm, 7atm, 5atm, and 2.5atm samples.

This is significant for two reasons. The first is that one of the primary ways in which questions arose about the nature of the spin ice state was that the system behaved differently under different time scales. Here, we show that oxygen growth condition changes by a large

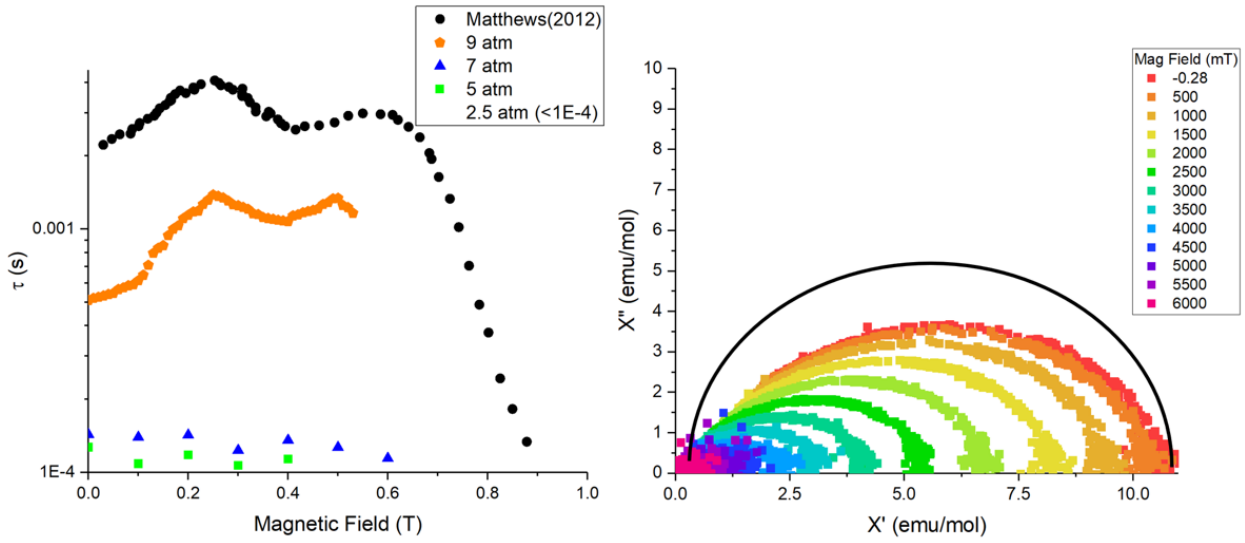

Figure 4.8: Left: Casimir-Du Pre single channel relaxation analysis of 9 atm sample, 7 atm sample, and 5 atm sample. Note that although it is not represented on the plot, the error in determining the peak frequency increases at higher fields, so those values are less confident than the lower field values. Right: Cole-Cole plot of 9atm sample, with a solid black circle representing a single relaxation channel form.

margin the relaxation times of the system while maintaining some key aspects of the spin ice state. Secondly, the original authors of the paper on relaxation times [68] indicated that their data too was quantitatively different from prior measurements [82] on powdered samples. This discrepancy they blamed on slight oxygen off-stoichiometry, further indicating that the key difference between sample results was the oxygen content.

In structural, thermal, and magnetic measurements, we have seen that changing the oxygen pressure during growth results in systematic changes in $Dy_2Ti_2O_7$ characteristics. Such oxygen content related effects have been supported as the source of many unusual behaviors in spin ice. In x-ray diffraction data, we see that there is a systematic change in the lattice constant, indicative of varying oxygen content in the samples. In the heat capacity data, we see that the variation is best explained by the presence of pinning oxygen vacancies, which fit the data better by changing the relative degeneracies of the "two in, two out" state and the single defect state, rather than being explained by other ways in which the configurational entropy can be changed, such as by straining the lattice or by changing

the Ising spin nature. In the ac susceptibility data, we see that this oxygen vacancy causes a wide change in relaxation time, with longer times at increasing oxygen vacancy density, indicative again of a spin pinning behavior.

Chapter 5

Thin Film $Dy_2Ti_2O_7$

5.1 Thin Film Growth Procedure

Using the pulsed laser deposition system and technique described in Section 3.1.2, we ablate a 1" diameter and 1/4" height dysprosium titanate compressed powder target at 3 Hz with a laser energy of 1.8 J/cm^2 in a rectangular spot size focused to 1 mm by 1 cm. This energy and spot size are achieved by using about 6 or 7 attenuators, reducing the beam energy and variation by a factor of 1/2, then by focusing the beam with the 20mm lens placed at about 22" from the deposition chamber window. The ablation is done in a 15 Pa pure oxygen atmosphere, with the substrate heated to 800 C. (I should note here that it would be interesting to grow films at the same oxygen pressures and temperatures as the crystals, if a suitable substrate can be found.) Currently we are growing on polished and oriented Yttria-stabilized Zirconia (YSZ) substrates, which are lattice matching to within 2% of the DTO crystal structure. Furthermore, there are a number of other variables which we can change during our growth sequence. For example, target rotation speed can change the extent to which the ablated surface is uniformly heated and removed. Also, target-substrate separation distance is crucial to depositing plasma which is neither too weak to deposit on the surface nor too powerful so that it removes material already deposited. For the parameters noted, we found that a separation of about 1" was sufficient to obtain a good plume and consistent deposition.

A typical thin film growth procedure consists of the following:

A commercially available oriented YSZ substrate purchased from MTI Crystal is cut via

scoring with a diamond tipped scribe and mounted with silver paste on the cleaned heated deposition stage. Its orientation can be changed by rotating its attachment point at the KF flange, and its separation from the target can be adjusted via a set screw. Once mounted, the substrate heater and thermometer must be plugged into the heater PID control box, which can then be programmed to ramp and hold temperatures. Next, the target is sanded to remove any surface imperfections and inspected for cracks. It is attached to the copper target mounting block with silver paste, and mounted on the rotor head in the chamber. The magnetically-coupled rotor outside the chamber is then attached to the motor via a rubber belt (usually an o-ring). Once installed, the chamber is sealed and evacuated using the turbo and roughing pumps. The evacuated chamber is then re-filled with a rate of oxygen controlled roughly by the turbo speed and pump shutter, and more finely by the flow controller settings. The substrate is then heated at a controlled rate, and may be pre-annealed. With an adjustable feed-through shutter between the target and substrate, we can then begin the rotation and pre-ablation of the target to create a uniform ablation region. Ablation then can begin with the desired parameters set. After ablation, we can perform any post-annealing, then allow the substrate to cool to room temperature, and vent the chamber.

For our experiments, we sought first to vary the thickness of the films by varying the time of growth while keeping a consistent rate of ablation. All other parameters were kept largely the same as well. The most variable parameter would be the energy density at the target. Pulse to pulse variations caused by the inherent uncertainty in laser energy were averaged over many cycles, but small changes in the laser working gas pressure cause a need to vary the number of attenuators to reach an approximately equivalent energy density. This may the cause of the difference between measured thicknesses on samples grown under nominally equivalent conditions due to the apparent important effect of the art of controlling the size and intensity of the plume. Other parameters which may have varied included those which we had less precise control over. For example, the alignment of the substrate above the

Sample Label	Substrate	Orientation (mm)	Substrate Thickness (Hz)	Growth Time (min)	Growth Rate (Hz)	Film Thickness (nm)	Weight (mg)	Shape
KS020116	YSZ	[100]	0.5	60	3	180 (est)	76.6	5x5 mm Square
KS020416	YSZ	[100]	0.5	15	3	45 (est)	75 (est)	5x5 mm Square
LT062216	YSZ	[111]	0.5	30	1	23.37	75.6	5x5 mm Square
LT070116	YSZ	[111]	0.5	60	3	45 (est)	74.2	5x5 mm Square
LT071316	YSZ	[100]	0.1	30	3	90 (est)	2.5	triangle
LT071416	YSZ	[100]	0.1	15	3	44	5.5	triangle
LT071516	YSZ	[100]	0.1	10	3	38	7.3	kite
LT071916	YSZ	[100]	0.1	10	3	30 (est)	10.1	kite
LT072116	YSZ	[100]	0.1	5	3	17.7	8.2	quadrilateral
LT072516	YSZ	[100]	0.1	1	3	3 (est)	7.1	quadrilateral

Table 5.1: Growth Conditions for Thin Film Samples

target did not have a consistent measurable distance; instead, we mounted the substrates on the same location on the substrate heater every time, though any misalignment caused during re-installation of the heater in the chamber may cause the substrate to be exposed to a different part of the plume. Finally, although great care was taken to prepare the target before each deposition, we noticed that after many growths, the target did start to form cracks. These may cause some non-uniformity in both heating and ablation and may result in a long-term trend in film behavior.

A few other observations about growth conditions and their effects are worth noting: Growths done under vacuum conditions with no additional oxygen environment supplied resulted in the blackening of the target and presumably an oxygen-depleted film. On this and other parameters, we began by following the rough growth conditions outlined in prior literature. Notably the conditions found in the papers by Bovo and Leusink [34, 35] yielded a reasonable looking plume and avoided the target change seen outside this range.

5.2 Structural Characterization

To understand our film growth process, a useful feedback is obtained from the structural probes of the x-ray suite of measurements. As noted in Chapter 3, we can obtain composition information from x-ray fluorescence measurements, orientation and strain information from x-ray diffraction measurements, and thickness information from x-ray reflectivity mea-

surements.

5.2.1 X-ray Fluorescence

X-ray fluorescence measurements rely on the emission of characteristic x-rays from elements within the target. Electronic energy levels within each element are detected after electrons are excited to a higher energy state and then the characteristic x-rays are measured as the electrons relax back to their prior state. Since these energies are unique for each element, we can obtain a measure of the elemental of the film and substrate by examining the x-ray spectra measured from the sample.

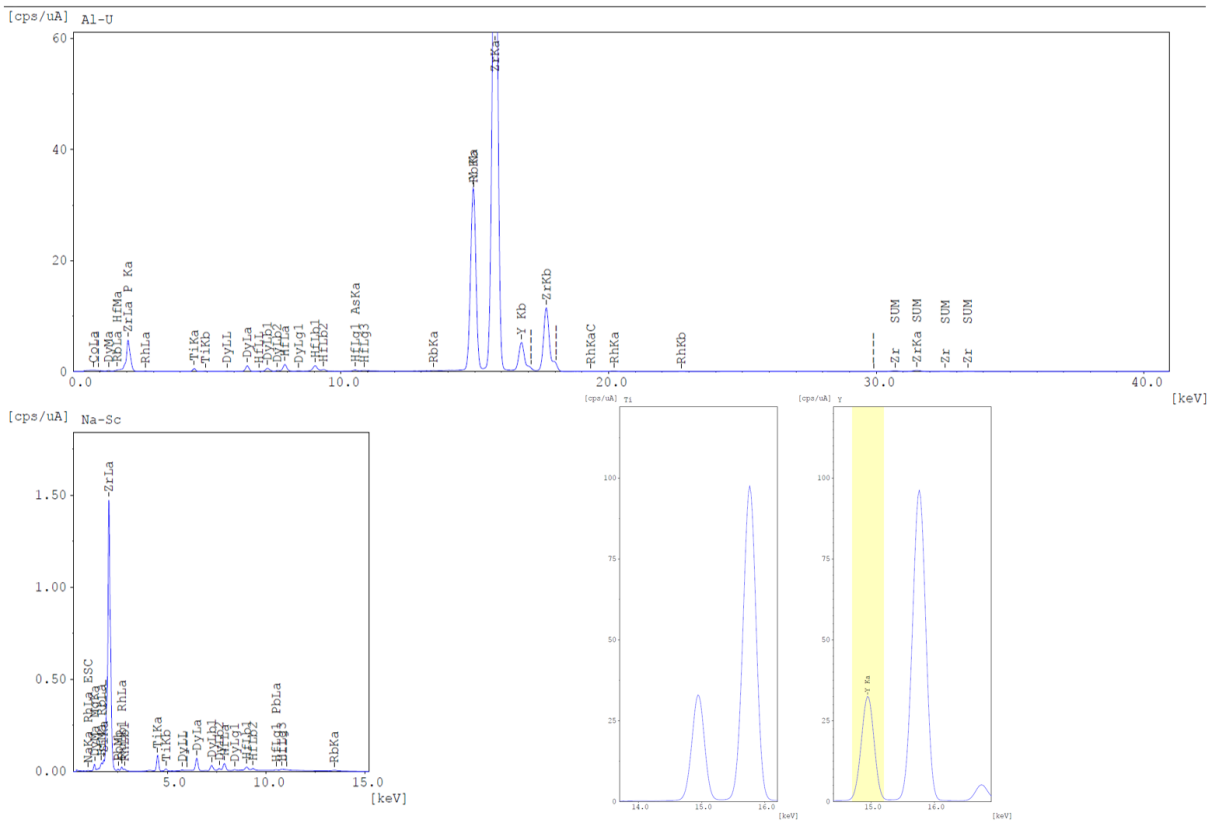

Figure 5.1: Counts per second of x-ray fluorescence (XRF) from a 60-minute film growth time at 3 Hz over a range of fluorescent x-ray energies. At top, the widest energy spectrum is shown, capable of detecting elemental transition signatures between Aluminum and Uranium. At bottom left, a more precise low energy scan is capable of showing elemental transition signatures between Sodium and Scandium. At bottom right, two expanded views of Yttrium and Zirconium peaks.

In Figure 5.1, we can see that many peaks emerge when measuring a broad range of x-ray energies. The Shimadzu EDXRF has two separate detectors operating over different energy spectra. As seen in the separate XRF scans in Figure 5.1, we were able to extract primarily emissions from yttrium and zirconium, the two primary components of our substrate material. Since the thickness of the substrate is many orders of magnitude larger than the film, we then look toward the smaller peaks to determine the composition of our material. As seen especially in the lower energy scan, peaks emerge on a much smaller scale to indicate the presence of Titanium and Dysprosium. In particular, we can see qualitatively the relative size of the Titanium K-alpha peak to the Zirconium K-alpha peak, and the Dysprosium L-alpha peak to the Zirconium L-alpha peak. From this data, we can see that we have deposited dysprosium and titanium in stoichiometrically correct ratios (i.e. 1:1), indicating that the target material was appropriately made and accurately deposited onto the substrate.

5.2.2 X-ray Diffraction

As in crystals, x-ray diffraction can be used to determine the orientation of the deposited film material. Whereas XRF indicated the stoichometry of the film, XRD can tell us if we have deposited an oriented and coherent layer of film material on our substrate. We first took a look at the YSZ substrate under x-ray diffraction, and we obtain the scan as in Figure 5.2. Growing a film over the substrate yields a second peak as in Figure 5.3, which indicates that we have grown a separate material on top of the substrate, oriented in the correct direction but with a separate lattice parameter. This is an excellent indication that we have avoided strain effects, since a strained film would have a lattice parameter equal to that of the substrate. However, a zoomed in and more careful scan of such a film and substrate measurement in Figure 5.4 shows that the peak associated with the substrate is narrower than the peak associated with the film. This may indicate that there is a wider range of lattice parameters associated with the film than the substrate, and perhaps a strained film

near the interface but that strain relaxes as the distance from the interface increases.

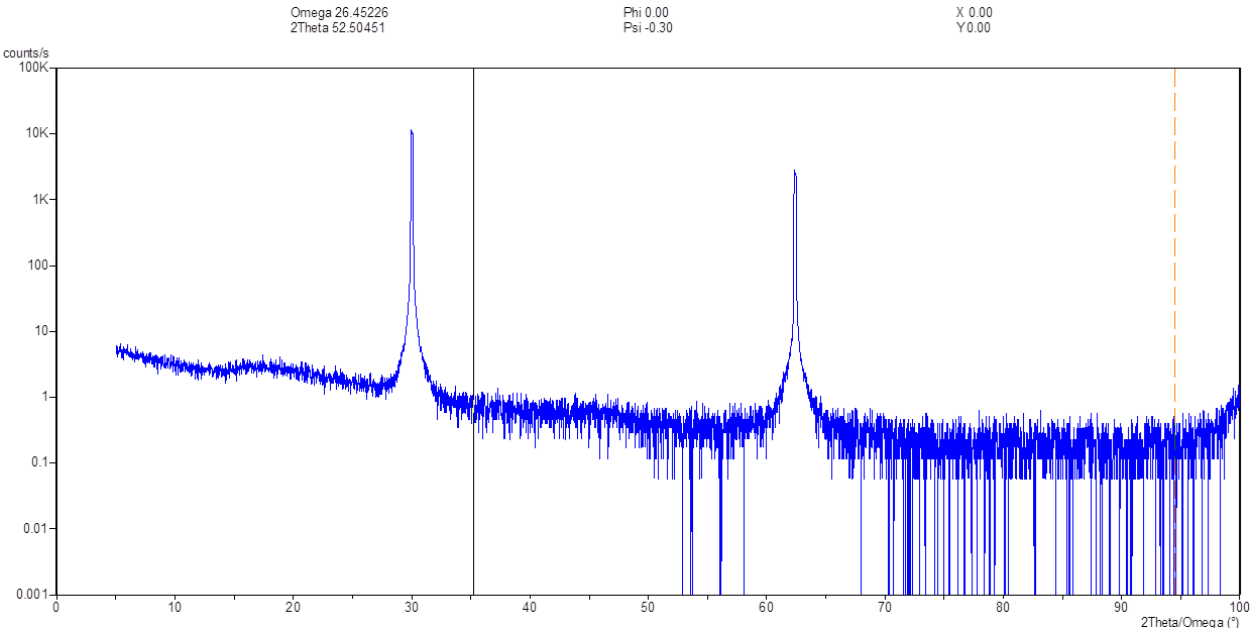

Figure 5.2: XRD wide angle scan. Note the lack of double peaks.

5.2.3 X-ray Reflectivity

X-ray reflectivity was a third structural analysis technique we used to probe the thickness of the film. Our external parameter to control the thickness was varying the growth time and hence number of laser pulses for each growth. However, due to the number of other parameters to be set in the film growth process, it becomes difficult to predict film thickness per pulse for any given material. Thus a simple way to get a handle on the rate of deposition is to use XRR to probe the film thickness for a range of growth times. As we can see in Figure 5.5 and as we saw earlier in the description of XRR, fitting of the XRR curves is empirical though we can get a sense of the thickness by noticing the width of the period in the oscillation. The three films in Figure 5.5 show an inverse relationship between period of oscillation and growth time, which correlates with thickness. Thus with all three x-ray analysis techniques, we can get a sense of the composition, orientation, and thickness of the films. Finally, although there is some information about surface roughness in XRR, we

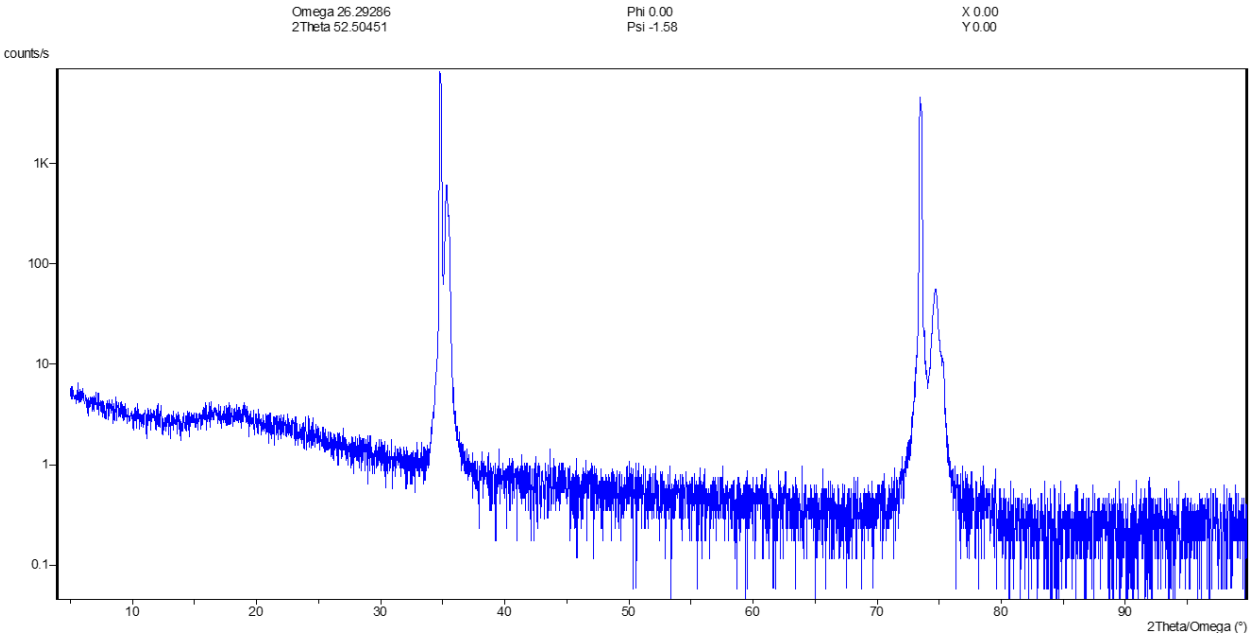

Figure 5.3: A wide scan of a film and substrate. Note the slightly offset peaks indicating that two separate lattice parameters exist within the sample.

can also examine the films under Atomic Force Microscopy to examine the uniformity and smoothness of the films.

5.2.4 Atomic Force Microscopy

Atomic force microscopy scans of the grown films indicate a smooth film on the order of 1 nm surface roughness over a range of the 4 um by 4 um scan. This is on the order of a single unit cell of DTO, and compared with the thickness of the films on the order of 3-60 unit cells, we can say that the films are mostly unaffected by signficant surface variations. Importantly, unlike other attempts to grow films via PLD, we do not see significant clumping, a slope in the film level, or cracks or other surface imperfections.

5.3 Thermal Probes

As with the crystals, we were able to take heat capacity measurements using the He-3 insert on the PPMS. The output of the heat capacity measurements for films have an additional

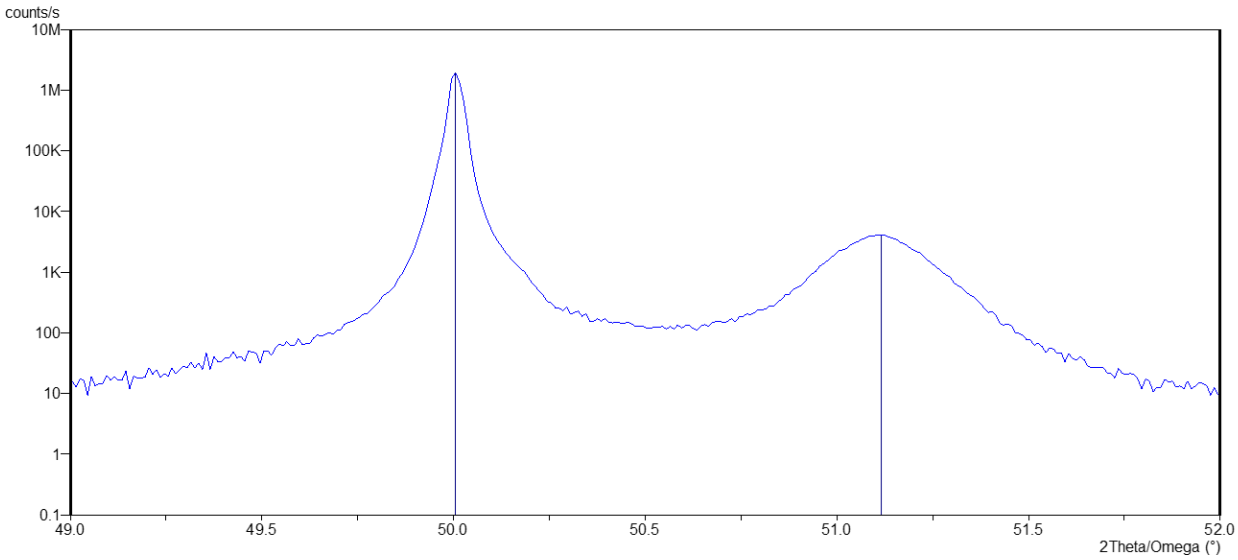

Figure 5.4: X-ray Diffraction of a 60-minute Thin Film in the 440 direction. The two closely spaced peaks indicate the presence of two layers of materials with similar lattice spacing.

complication due to the fact that the heat capacity measurements will also show a contribution from the substrate. Therefore in addition to the previously subtracted components from the crystal samples, which were the contributions from the PPMS setup, the N-grease, and the phonons, the contribution from the substrate must also be fit and subtracted. For YSZ, an insulator, the only significant contribution to the heat capacity at these low temperatures is phononic, and so from the data in Figure 5.8 we can see that the contribution from the much thinner film appears as a bump in the low temperature heat capacity. Subtracting the substrate and phonon contribution from the heat capacity measurement, we can see in Figure 5.9 that on a per-spin or per-tetrahedron basis (a factor of 4 difference), a Schottky-like anomaly emerges around the same temperature as in the crystal case. This is a good indicator that we have created a system which enters into the spin ice state. The more interesting feature, however, appears at lower temperatures. Whereas in the crystal samples, the primary variation was in the shape, height, and location of the Schottky-like peak, in this case there is an additional contribution around 500mK which varies between films. Since a per-spin basis is inherently a per-volume measurement, we can also re-scale

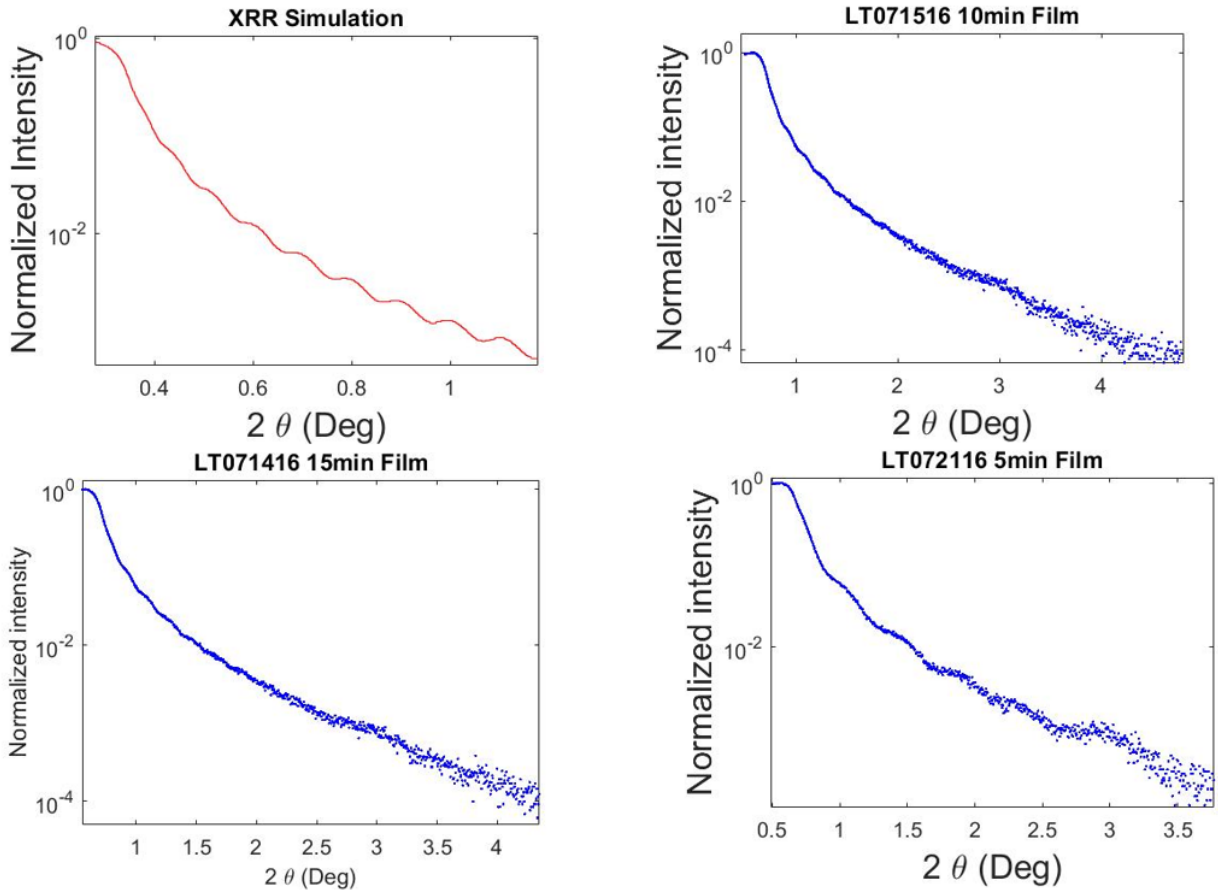

Figure 5.5: Four plots of XRR simulation and results. The top left shows a simulation for a film of thickness 40nm, and the rest of the plots show results from XRR scans on different growth times. Kiessig fringes in these measurements show the smoothness and thickness of the films.

the vertical axis to show the contributions to the heat capacity on a surface area basis in Figure 5.10. This varies not on the mass or thickness of the sample but on the surface area of the film. If the additional contribution arises from an effect on the top surface of the film or from the interface of the film and substrate, the peak should be invariant under a surface area re-scaling, instead of a volume re-scaling. Indeed, when the film heat capacity is re-scaled by surface area, we can see that the three thinnest films have a lower temperature feature of similar magnitude, while the thicker film's low temperature feature is suppressed. So, it appears as if this low temperature feature is a surface or strain effect, and based on the bifurcation between thin and thick films, it may be some kind of surface ordering which

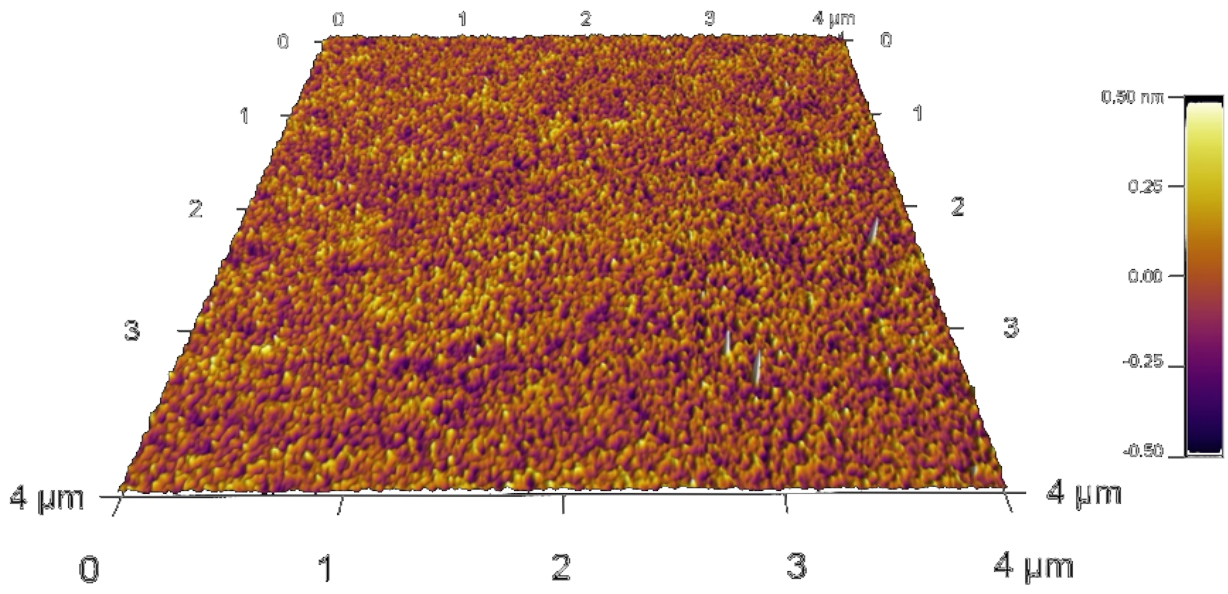

Figure 5.6: A 3d plot of surface height over a 4um by 4um atomic force microscopy scan of a thin film deposition shows no significant clustering or cracking, and an average roughness of 1nm, on the order of one dysprosium titanate unit cell.

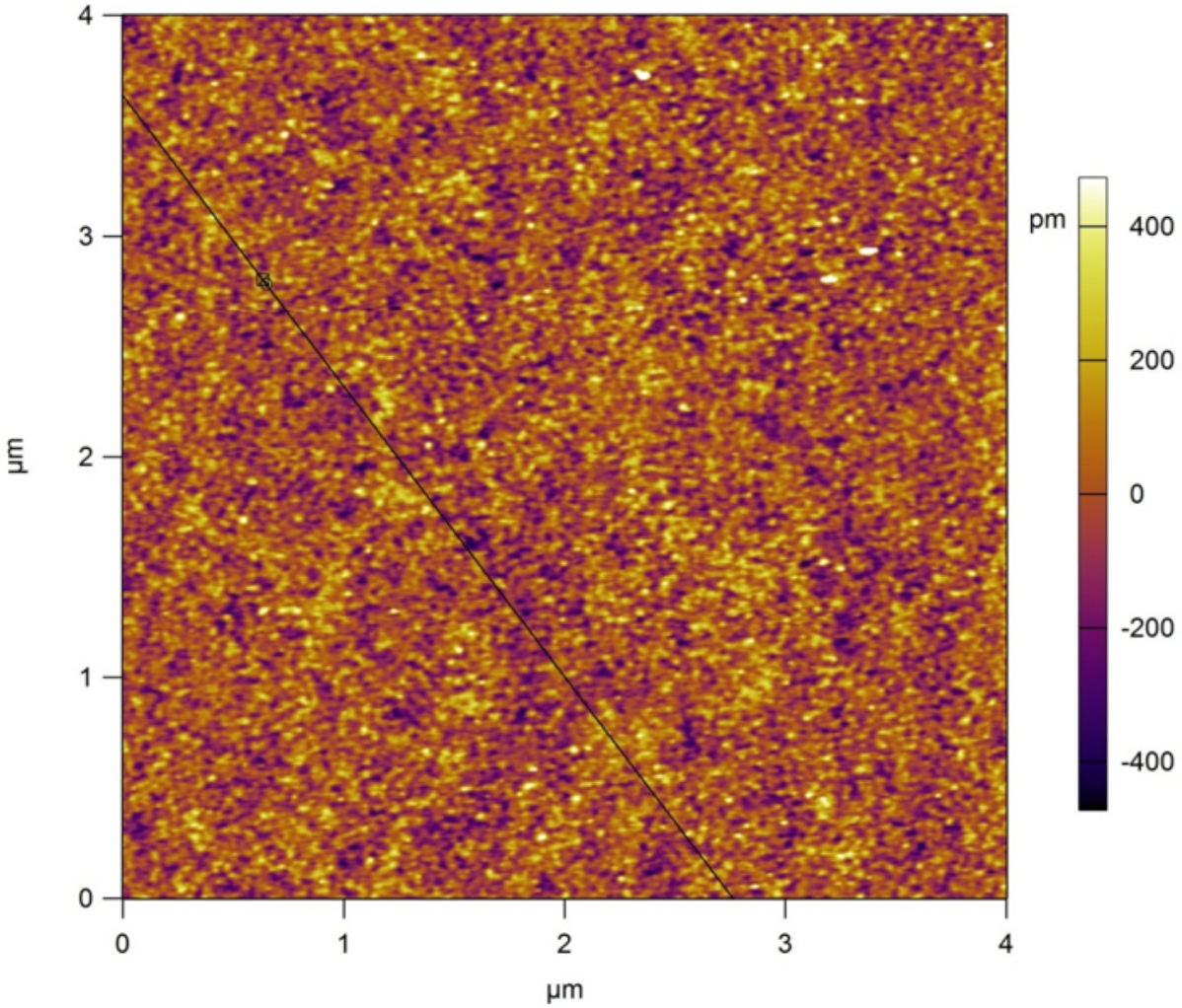

Figure 5.7: A top down view of the same scan in Figure 5.6 shows any horizontal and vertical trends.

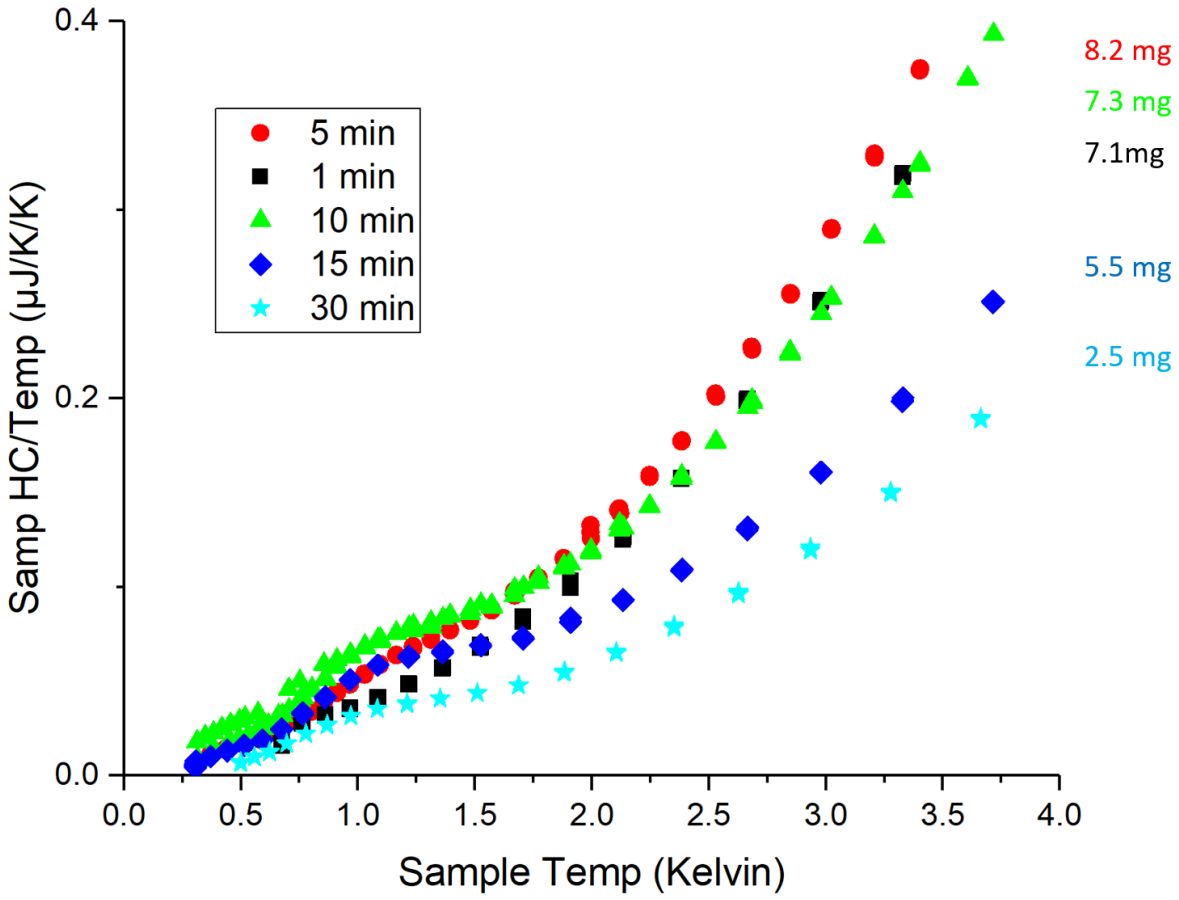

Figure 5.8: Heat capacity versus temperature shows the impact of phonons from the substrate and film on the overall heat capacity curves. The small bumps around 1K represent the Schottky-like anomaly in each sample. The masses of each substrate are shown to the right, indicating that the main contribution arises in proportion to the mass of the substrate, and does not correlate with the thickness of the film.

emerges as dimensionality is reduced. If it were strain effects, we might expect a monotonic trend as the film thickness increases. It may also be interesting to look at how the additional low temperature feature contributes to the entropy, as the magnitude of entropy recovered may correlate with some type of surface ordering.

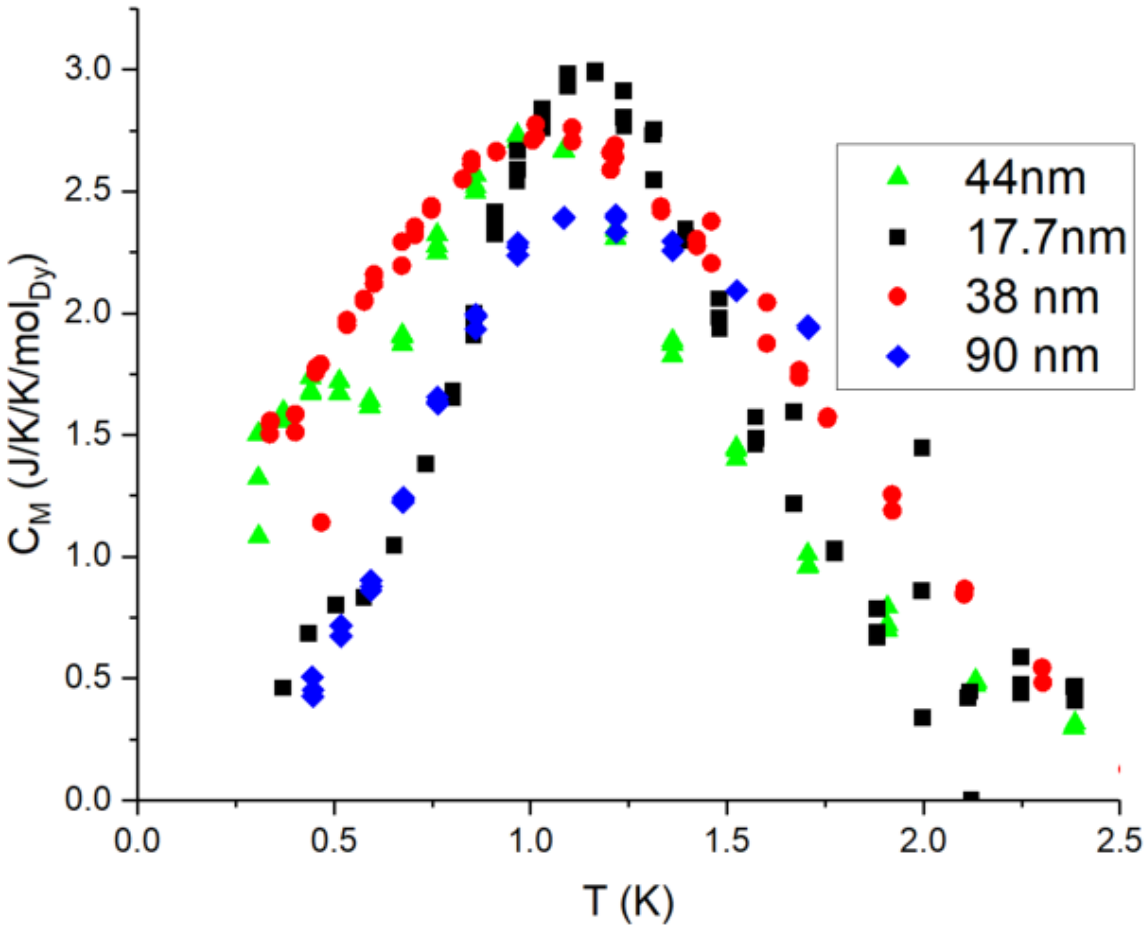

Figure 5.9: Heat capacity divided by temperature versus temperature per Dy spin shows a Schottky-like anomaly around 1K for four spin ice thin film samples, and in comparison to crystalline spin ice, exhibits additional features at lower temperatures around 0.5K.

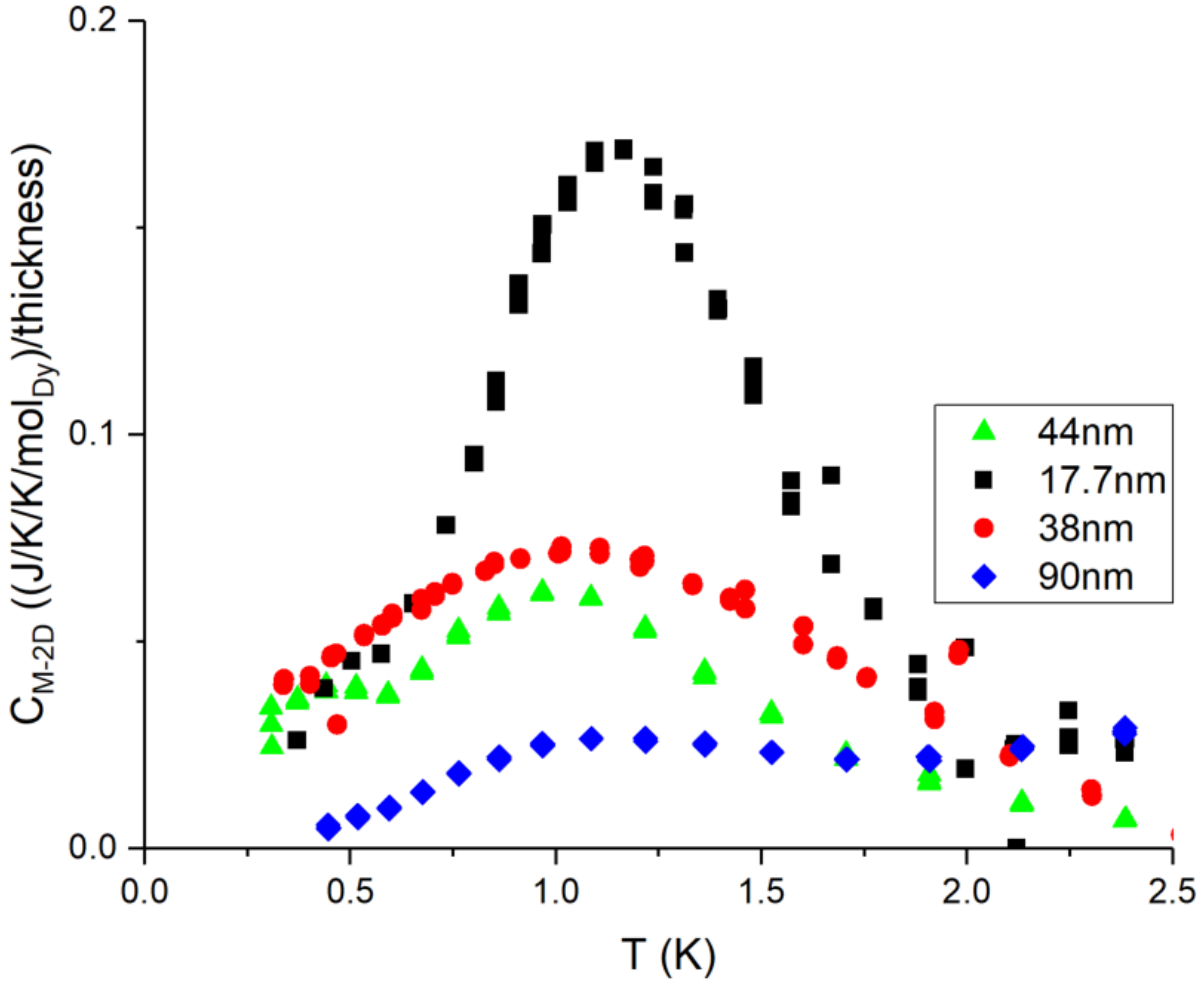

Figure 5.10: Heat capacity divided by temperature versus temperature on a surface area basis instead of a per Dy spin basis. The lower temperature feature from Figure 5.9 becomes a surface-area independent feature for thinner films.

Chapter 6

Superconducting Quantum Interference Device Magnetometry

As the original driving experiment for this research, SQUID magnetometry in external fields and thermal gradients has also spurred the creation of the high quality crystals and thin films described above, which helped answer open questions in the field of spin ice research and generated new questions of their own. The SQUID magnetometry experiments sought to extract signatures of magnetic monopoles by using techniques similar to vortex thermoelectric experiments also from the 1980s [83] [84], in contrast to experiments conducted by Blas Cabrera in 1982 [21]. Although we are using a SQUID detector to look for monopole-like excitations, the parallels with vortex experiments are much stronger.

The analogy with superconducting vortices in thin films is as follows:

First, in both cases quantized magnetic flux and anti-flux pairs are generated with a density profile that is at least exponential with temperature.

Second, in both cases the excitations relax under a single relaxation time when driven out of equilibrium (by an electric field in the vortex case, or a magnetic field in the spin ice case).

However, an important difference is that in the vortex case, the effects of pinning and (eddy-current) damping on the vortex motion were weak. In spin ice, the effects of pinning and screening have been unclear, yet our crystal results and others have indicated these may play an important role in changing or broadening the relaxation time as well as impacting the expected temperature dependence of monopole density through "spin freezing".

The primary result in the infamous Cabrera monopole search was a sharp offset in SQUID voltage, with an amplitude corresponding with an expected flux from a free monopole (yes,

just one single unrepeated and uncorroborated event, even going so far as to note that the lab was unoccupied at the time). However Cabrera contrasted this event with the usual offsets caused by more mundane things such as cryogen transfers. Although Cabrera's results were never replicated and often questioned, the emergence of magnetic monopolar quasiparticles in condensed matter and atomic BEC systems has generated interest in how such probes may be able to enlighten the behavior of magnetic monopoles.

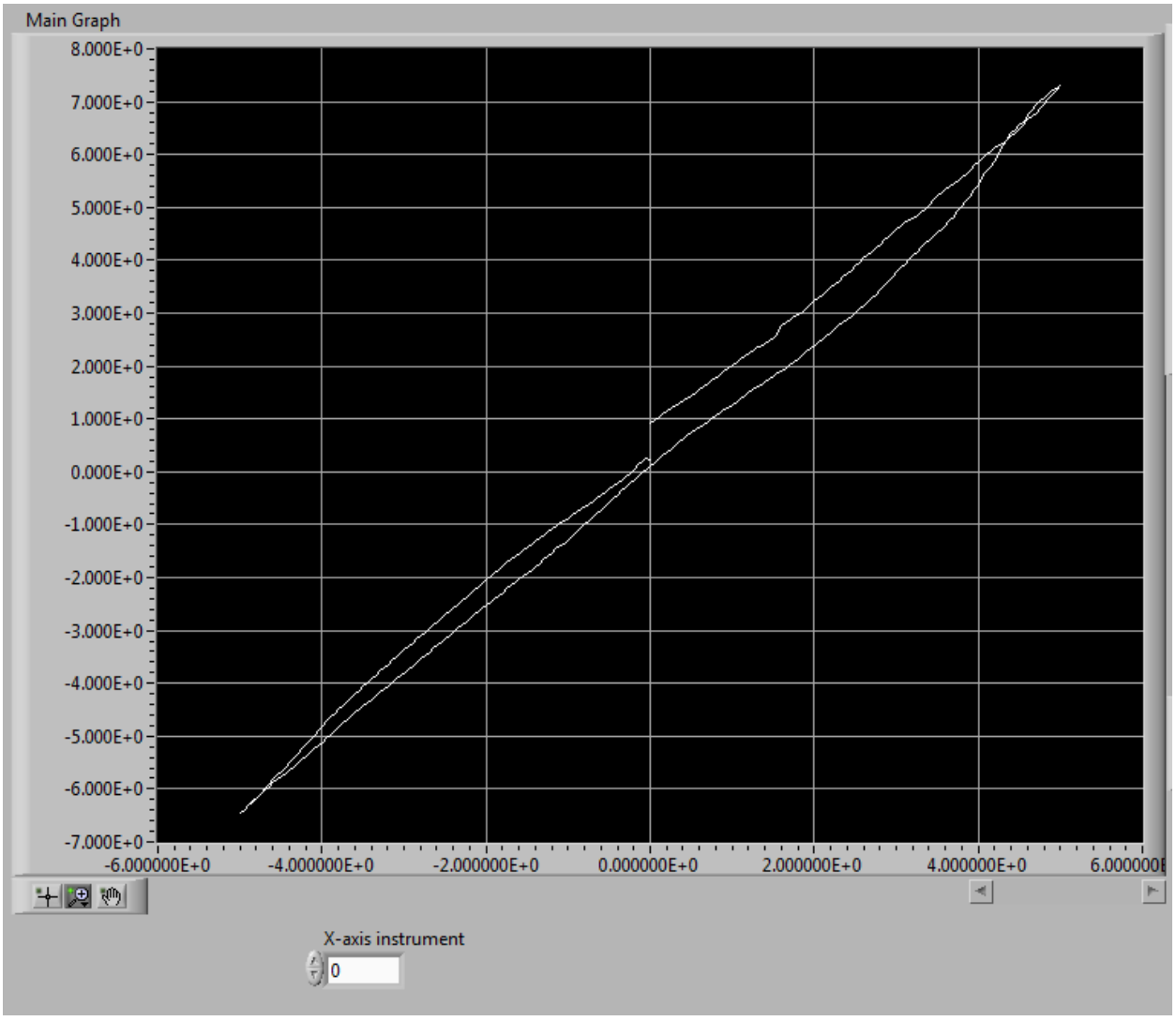

Figure 6.1: A known magnetic field ramped outside the shielding shows the field penetration and drift in the SQUID voltage response.

We created the setup described in Figure 3.5, and collected both SQUID voltage time

traces and SQUID voltage noise spectra, which we can then convert into SQUID magnetic flux measurements and SQUID magnetic flux noise signals. Practically speaking, the first and most consistent behavior of our SQUID system is its sensitivity. We saw earlier how the bare SQUID noise follows a characteristic 1/f and white noise pattern, but due to its sensitivity, we quickly discovered that magnetic signals of any kind, as well as vibrations, temperature variations, superconducting vortices in the wiring or SQUID itself, poor thermal connections, and proximity to the sample can all cause additional voltage noise which complicates measurement. Although we have some information about the theoretically predicted mobility of monopoles and the relaxation times associated with the dynamics of our samples [85, 86], nevertheless it seemed our best first approach was to simply see if any noise signatures emerged which fit the pattern of appearing in the case of an applied magnetic field and a thermal gradient but not appearing in either case individually nor in the background. In this way we hoped to bypass some of the issues typically associated with SQUID noise signals, compounded by the movable nature of the setup.

An example of the variation of the 1/f and white noise regimes under different conditions is shown in Figure 6.2 at 4K. Here we apply a thermal gradient of 50mK by applying a current to the counterwound heating coil, and then separately apply a field of 100 Gauss through the solenoid along the [111] direction of the crystal. Then, we apply both a thermal gradient and a [111] magnetic field to determine what extra contribution may arise due to effects not present in the previous cases, such as flux through the pickup loop due an excess of one species of monopole or another.

Another measurement of SQUID noise seen during the application of a heat load on one end and an applied field can be seen in Figure 6.3. Here, we look at temperatures within the spin ice range (100mK) and overlay guides to the eye on the white noise (blue lines) and 1/f (red lines) regions.

Recent theoretical work [40] and simulations [85] has indicated a change in the SQUID noise behavior in the low frequency regime resulting from the interplay between two relax-

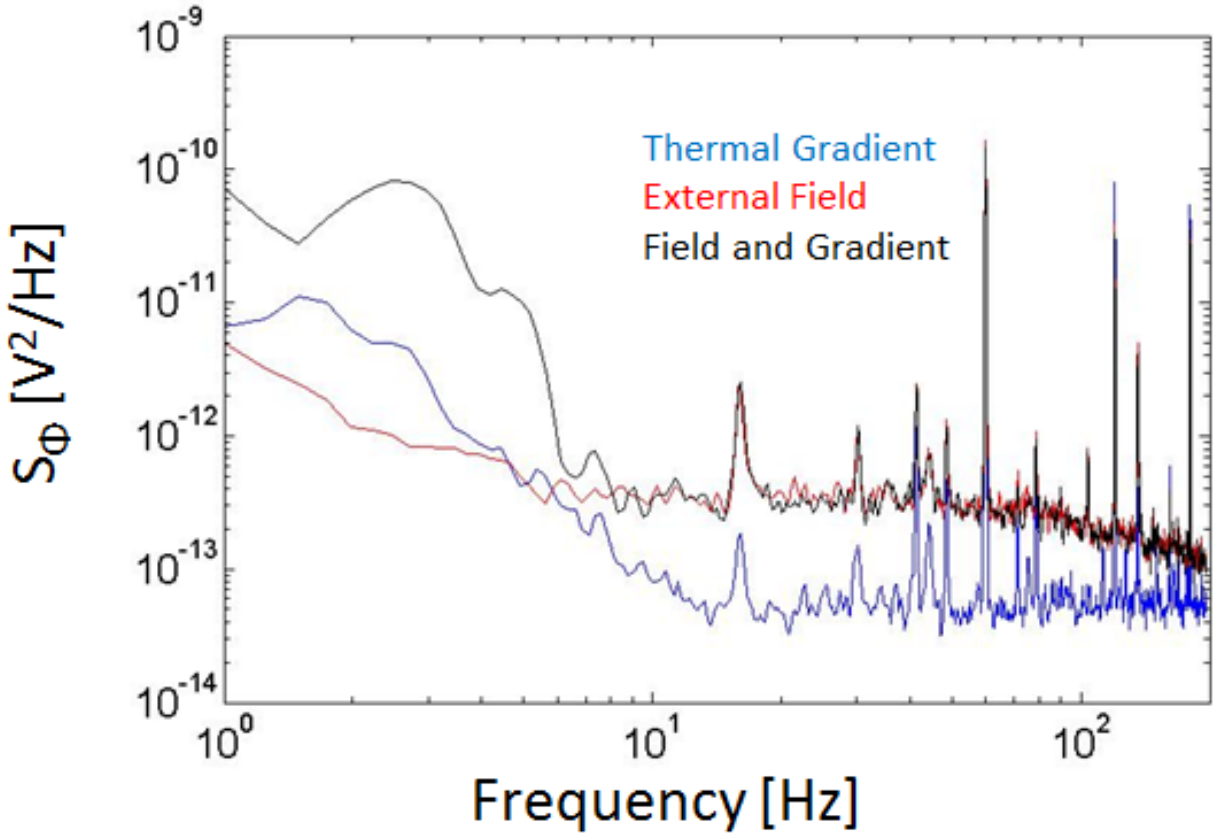

Figure 6.2: The blue curve is SQUID noise with a heat load applied. The red curve is SQUID noise with a DC field applied. The black curve is both field and heat applied.

ation timescales. This behavior manifests as an increase in the low frequency noise in the spin ice temperature regime compared to temperatures without this relaxation behavior, e.g. temperatures too high or too low. Similar trends were seen in some of our data, in Figure 6.4, though more data would further confirm this behavior.

Our thermal gradient and applied field experiment is expected to see an excess of magnetic charges of one species, and since we have some theoretical predictions for monopole density in the static case and mobility in the dynamic case, as well as more confident values for the magnitudes associated with the monopolar charge, we then become limited by less certain values for things like the pinning effects of defects and screening and surface effects of the spin ice manifold and of other defects.

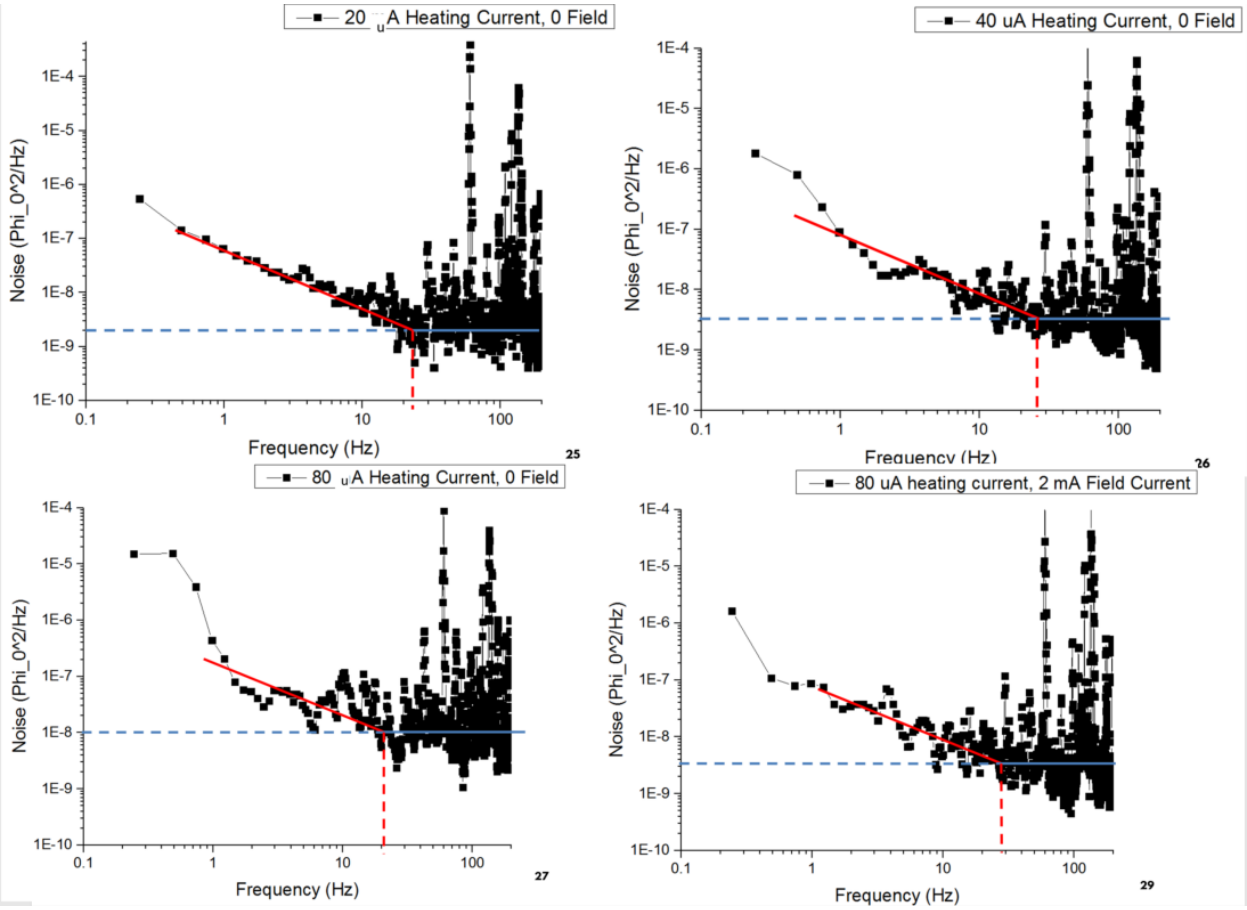

Figure 6.3: Note the movement of the 1/f to white noise intersection point as a function of applied field and thermal gradient.

We sought many methods to overcome these practical obstacles, first by mounting the sample, thermometers, and heating element on a translatable stage in a dilution refrigerator within a solenoid, so that the same SQUID could be used to measure conditions with and without a sample present. This background subtraction method suffered primarily from the difficulty of avoiding vibrational noise, since both pickup coil and sample assembly had to be placed on cantilevers into the solenoid. The sample assembly was particularly prone to vibration as the translation rod was manipulated at the top of the dilution refrigerator, increasing the overall scale of the system. Subsequently, we have begun taking similar measurements using a gradiometer setup and on thin films of spin ice material in an effort to improve signal to noise ratio.

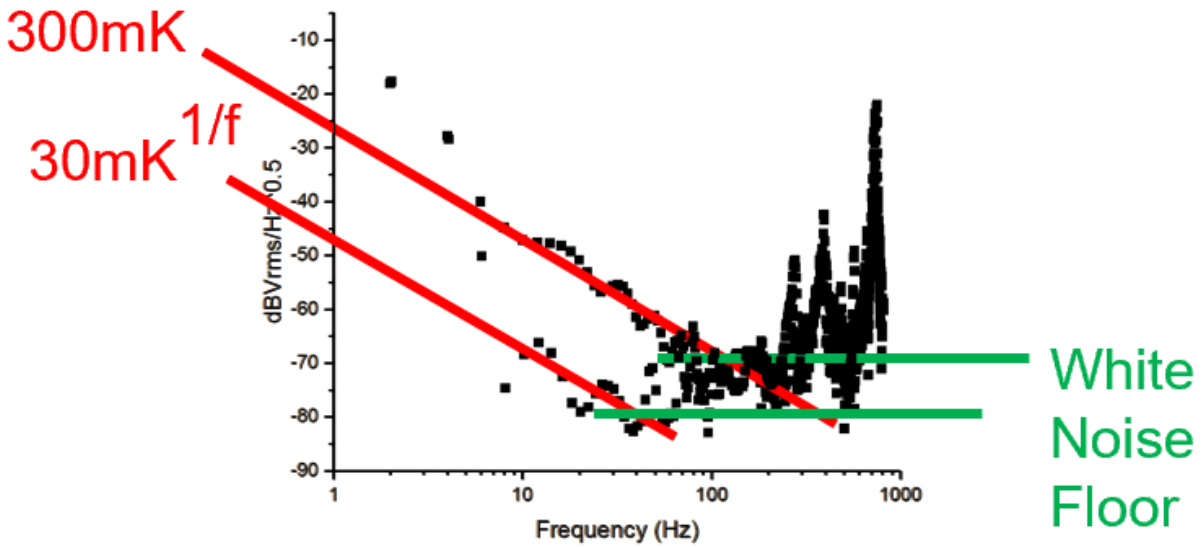

Figure 6.4: A decrease in low frequency flux noise signal as the spin ice dynamics freeze out.

Although these efforts have not produced as clear direct SQUID voltage signatures as expected, and much work remains in analyzing and collecting these types of measurements in our effort and others', we can look at aspects of the noise spectra to get some insight into the magnetic behavior of the spin ice samples. Interesting behavior may arise from the trends in the 1/f to white noise crossover point, the changes in noise at different base temperatures, and in particular, additional factors in the low frequency regime which indicate a transition from a 1/f distribution to a $1/f^2$ behavior, which in another SQUID study [87] has been theorized to originate from correlated spin flips. This is particularly interesting because it is the sort of dynamics we would expect from a system of spin defects driven out of equilibrium, and it is currently perhaps our strongest indicator of monopolar behavior in this particular configuration by analogy with thermoelectric probes of vortex dynamics.

Chapter 7

Conclusions

7.1 Impact

Our search for thermal and magnetic signatures of quasi-monopoles in spin ice via SQUID magnetometry drove the creation and investigation of a range of spin ice crystals under different oxygen growth conditions and spin ice thin films of varying thicknesses.

We have seen by the systematic changes induced in our crystals that oxygen content or vacancy may play a critical role in affecting spin ice behavior and measurement consistency. We saw in structural measurements that a small change in oxygen content yields a distinct trend in lattice parameter. Thermally, that results in a spread of entropy around the expected spin ice value as the shapes of the Schottky peaks change, possibly due to disorder [88] and relative degeneracy effects [50]. Magnetically, trends in the relaxation times may indicate oxygen-modulated changes in interaction strength, as spin flip processes may become pinned by oxygen vacancies.

The results of varying oxygen growth conditions for our spin ice crystals help to guide answers to open questions in the field of spin ice centering on statics and dynamics and thermal and magnetic behavior of spins in frustrated systems. In particular, the timescale of "spin freezing" inhibiting equilibrium in the lowest temperature ground state of spin ice was proposed to be related to oxygen [28, 89], and our heat capacity measurements could indicate that while oxygen may affect the particular form of the Schottky anomaly, DTO still progresses through the spin ice state even with different oxygen contents. Magnetically, we saw that a dynamical quantity, the relaxation time, varies with oxygen content, and

prior probes of relaxation times cited oxygen content as a primary driver behind disparities between measurements [30].

In thin films, we see the appearance of low temperature features beyond the spin ice state which change depending on film thickness. This thermal signature may be proportional to the surface area, indicative of the effect of reduced dimensionality on a spin ice thin film. This is in addition to the usual spin ice schottky anomaly which indicates that we see spin ice behavior in thin films, helping to resolve an open question in the field of spin ice [34, 35] as to the persistence and effects of reduced dimensionality and strain and surface effects on the spin ice state. Further analysis of this low temperature feature may help indicate the nature of the low temperature spin ice ground state, as well as the disparity between the prior work on thin films. To that end, we have started Monte Carlo simulation work on thin films of spin ice, further described in the Future Work section below.

Finally, although our SQUID measurements have so far been less conclusive, we have measured spin ice crystals under thermal and magnetic conditions conducive to measuring the magnetic signatures of quasi-monopoles in spin ice. The data taken can be further analyzed and investigated, especially as new information and predictions about spin ice statics and dynamics emerge, for example in [85], a very recent paper proposing time scales for characteristic spin flip hopping frequency. These types of predictions may help illuminate the behavior that we do see in signals such as the change in 1/f to $1/f^2$ low noise behavior or possible trends in the 1/f to white noise crossover regime.

7.2 Future Work

While the present work may help to resolve some issues in the field of spin ice, the range of samples and the techniques and instruments developed may yet still be used to further expand understanding of frustration, fractionalization, and magnetism in these materials.

In the area of crystalline oxygen effects, one of the most readily available structural mea-

surements to complete is thermogravimetric analysis (TGA), a destructive but illuminating process by which spin ice samples are heated in an oxygen environment while being carefully weighed. This process was used with XRD in [10] on a trio of Yttrium Titanate samples to obtain a precise lattice parameter relation to the oxygen content of oxygen-depleted, -neutral, and -annealed samples. We use this relation by proxy in our relation of oxygen content to our XRD data on DTO samples, but a direct TGA measurement of our samples would provide further confirmation that the trend in lattice parameter is consistent with oxygen variation. Another open question in crystalline spin ice has to do with shape and surface effects on spin ice dynamics [90, 91], which with appropriately cut and oriented samples from the grown crystals could be answered.

On thin films, I should note the almost endless parameter space which could be explored in future work. While we varied the growth time and hence thickness, one could also vary with easily interesting results the substrate composition, substrate orientation, energy density, pulse rate, oxygen pressure or other gas environment, target density, target composition, and less quantitative things like plume size, shape, and color. As seen in the current thin film debate, there is already significant differences seen based on the choice of substrate, and indeed many of these parameters can impact the film quality and uniformity.

Additionally, much work has gone into Monte Carlo simulations of the statics and dynamics of spin ice. [92,93] Just as in experimental efforts, there has been less focus on simulations of film behavior and dimensional effects, and so to supplement the few existing investigations we have also begun to simulate thin films of spin ice. This in-house investigation may help us to understand better the origin of the observed low temperature feature, and perhaps predict behavior which we can then grow films to confirm.

Finally, throughout our efforts on SQUID investigations of spin ice statics and dynamics, we also considered some other modifications and approaches to attempt to get a better handle on how best to practically approach this behavior. One modification was to create a gradiometer in series in the SQUID pickup loop, wherein flux generated outside the sample

would act to cancel the signal in both halves of the pickup loop, but flux within the SQUID should generate a signal. This was partially inhibited by the revised translatable dilution refrigerator design, but a purpose-built setup could yield a more accurate measurement. One other possible improvement would be to fabricate a "microSQUID" on the surface of a crystal or thin film. This direct measurement would allow not only a smaller scale for a SQUID probe but also due to its narrow junction can measure in much higher magnetic fields (on the order of single Tesla), which then would open up probes of transitional behavior. A magnetic quench procedure was one such probe, where a large field would be quickly (relative to the spin dynamics) reversed, creating a non-equilibrium state of the spins and defects. A prior thermal quench procedure [94,95] was fruitful in understanding the dynamics of defects far from equilibrium.

An understanding of classical spin ice magnetodynamics can then assist in further study of more exotic and difficult materials, such as quantum spin liquids [96, 97], which can be seen as a vector to topological quantum computing [98] and probe to understand high temperature superconductivity [99]. The monopolar excitations themselves may prove useful in fundamental investigations of electromagnetism [100], multiferroics [101,102], and critical phenomena [103].

Appendix A

Preliminary Magnetic Measurements of Spin Ice

As we began collaborating with the MacDougall group at UIUC to grow a series of crystals at varying oxygen contents, we began investigating the magnetic characterization methods for probing the spin ice state, similar to those found in [68]. We found that some of these probes, such as magnetization measurements shown in Figures A.1, A.2, A.3, and A.4, showed few interesting spin ice features at available temperatures. However, we did see interesting trends in wide scans of parameter space in ac susceptibility data, as seen in Figures A.5 and A.7, though these were similar to prior literature studies [68], [104]. This helped inform us as to which measurements might be most useful to determine the magnetic trends under different oxygen growth conditions.

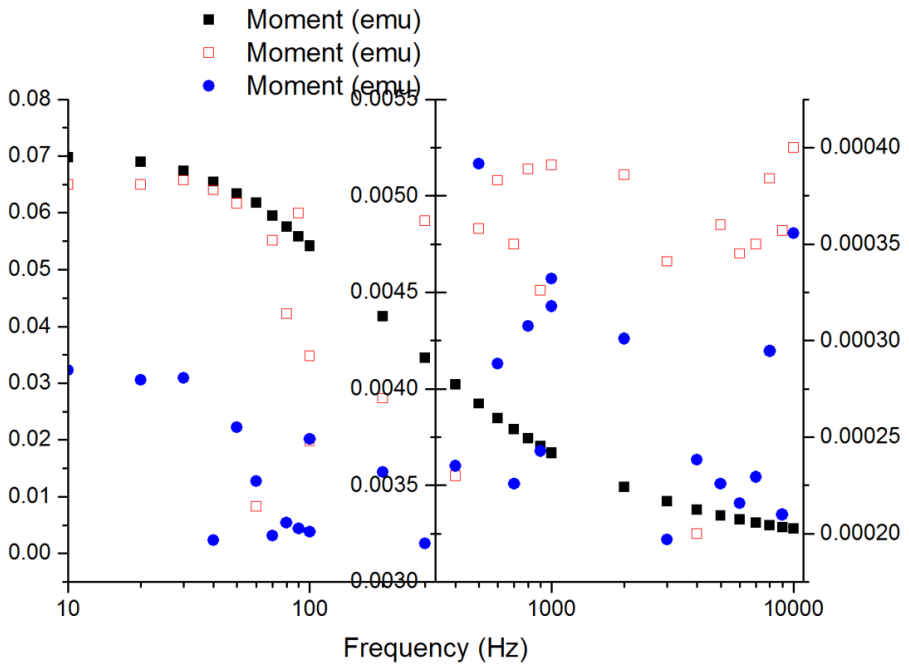

Figure A.1: Magnetization data on a spin ice crystal under a small ac field (10 Oe) as a function of frequency applied. Note that the scales for 2K, 5K, and 10K (left to right) decrease by an order of magnitude each time as the system becomes paramagnetic at higher temperatures. Notice also the emergence of some semblance of ordered response at 2K with a higher response at low frequency and a lower response at high frequency.

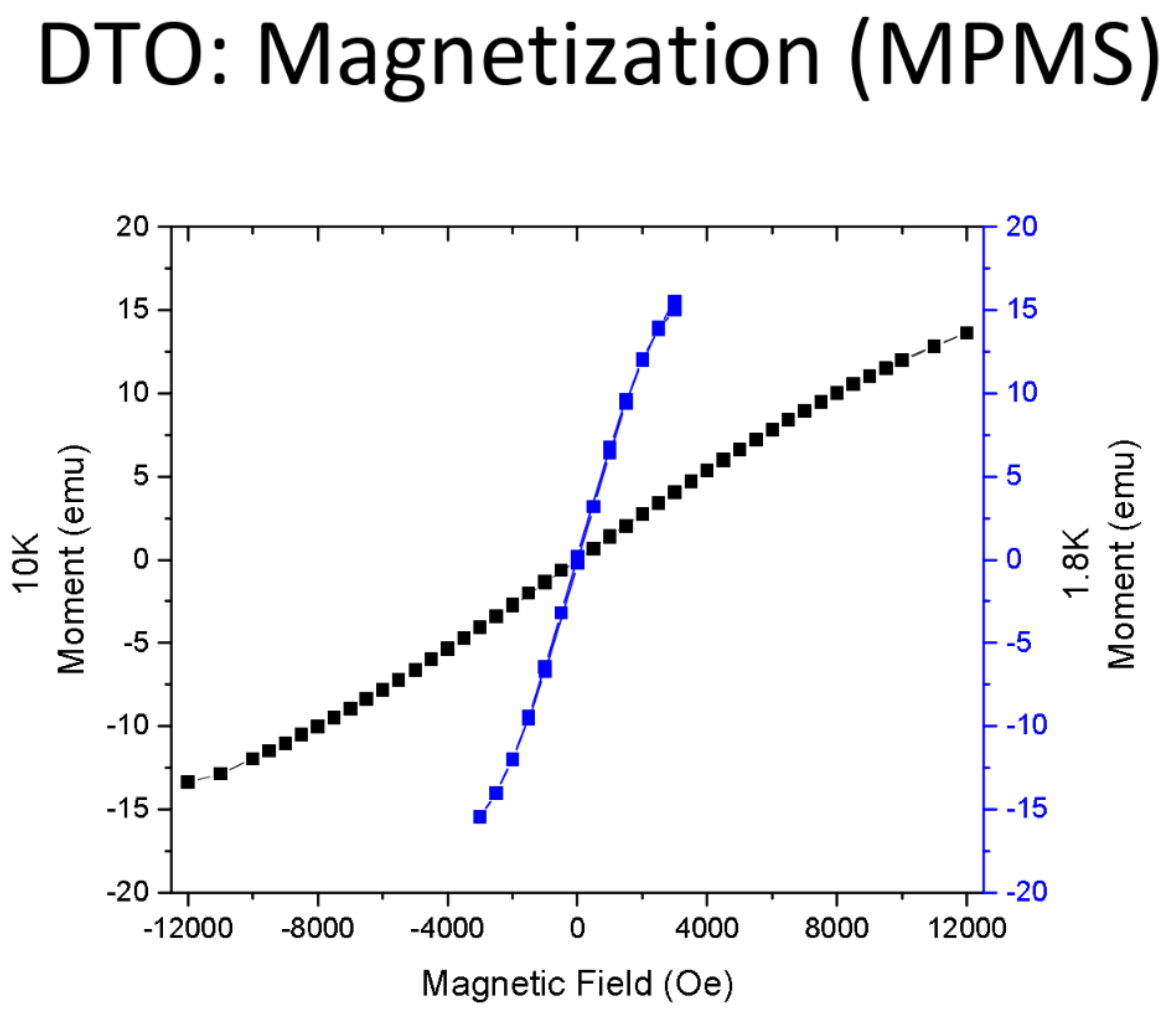

Figure A.2: An attempt to view the plateau features of DTO in a magnetization measurement shows no sign of plateaus down to 1.8K.

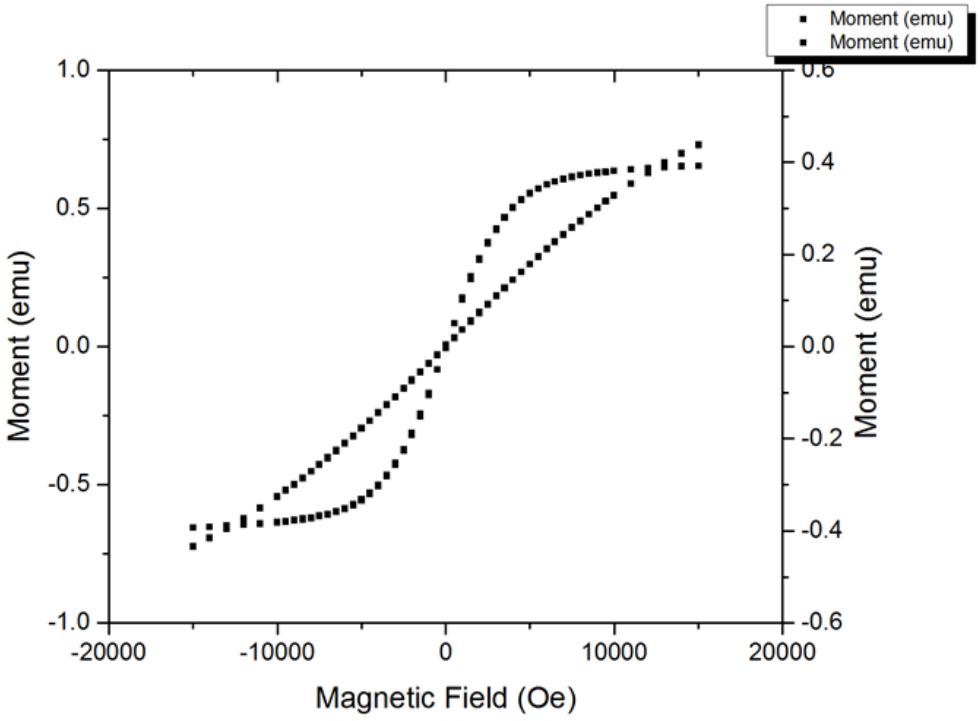

Figure A.3: Magnetization data on DTO shows a transition from paramagnetic at 10K to a saturated state at 2K.

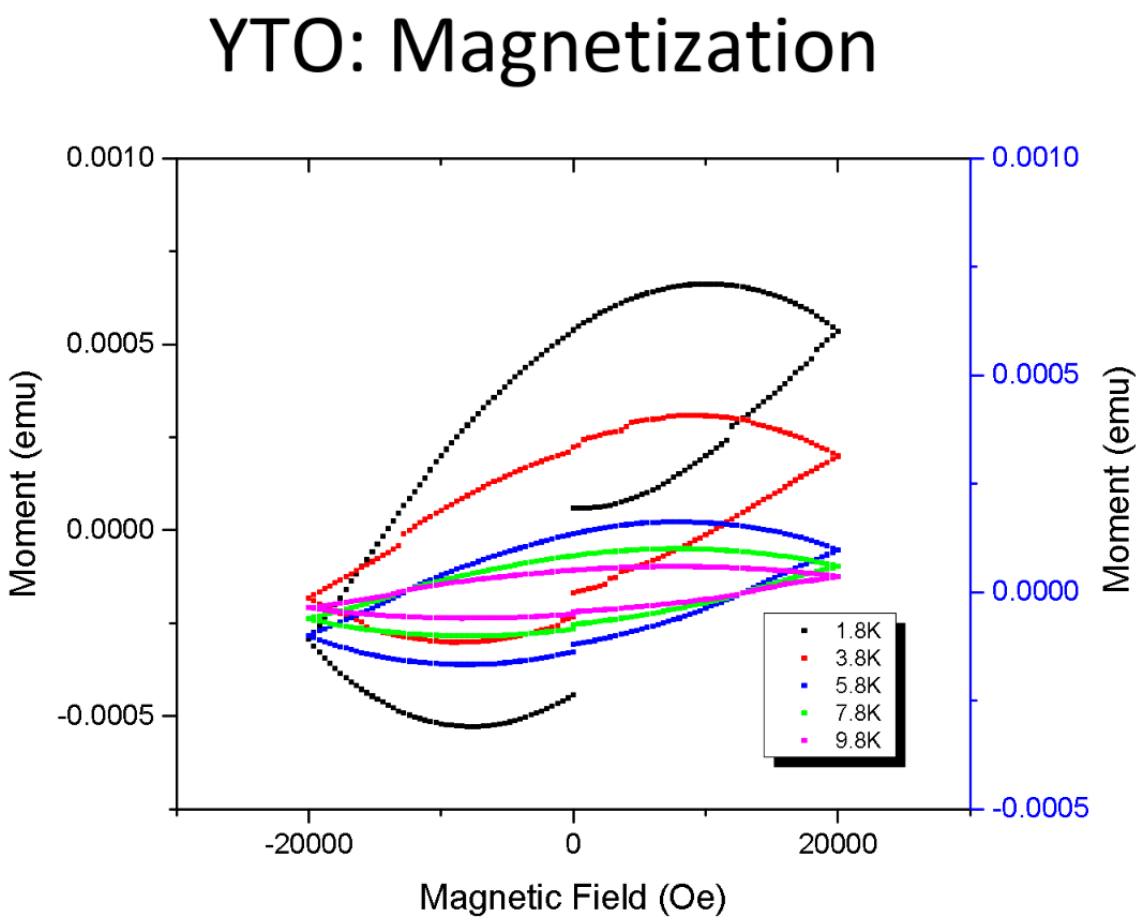

Figure A.4: Magnetization versus applied DC field data for Yttrium Titanate shows a small hysteretic background, which is negligible on the scale of the DTO signals, about 3 orders of magnitude smaller.

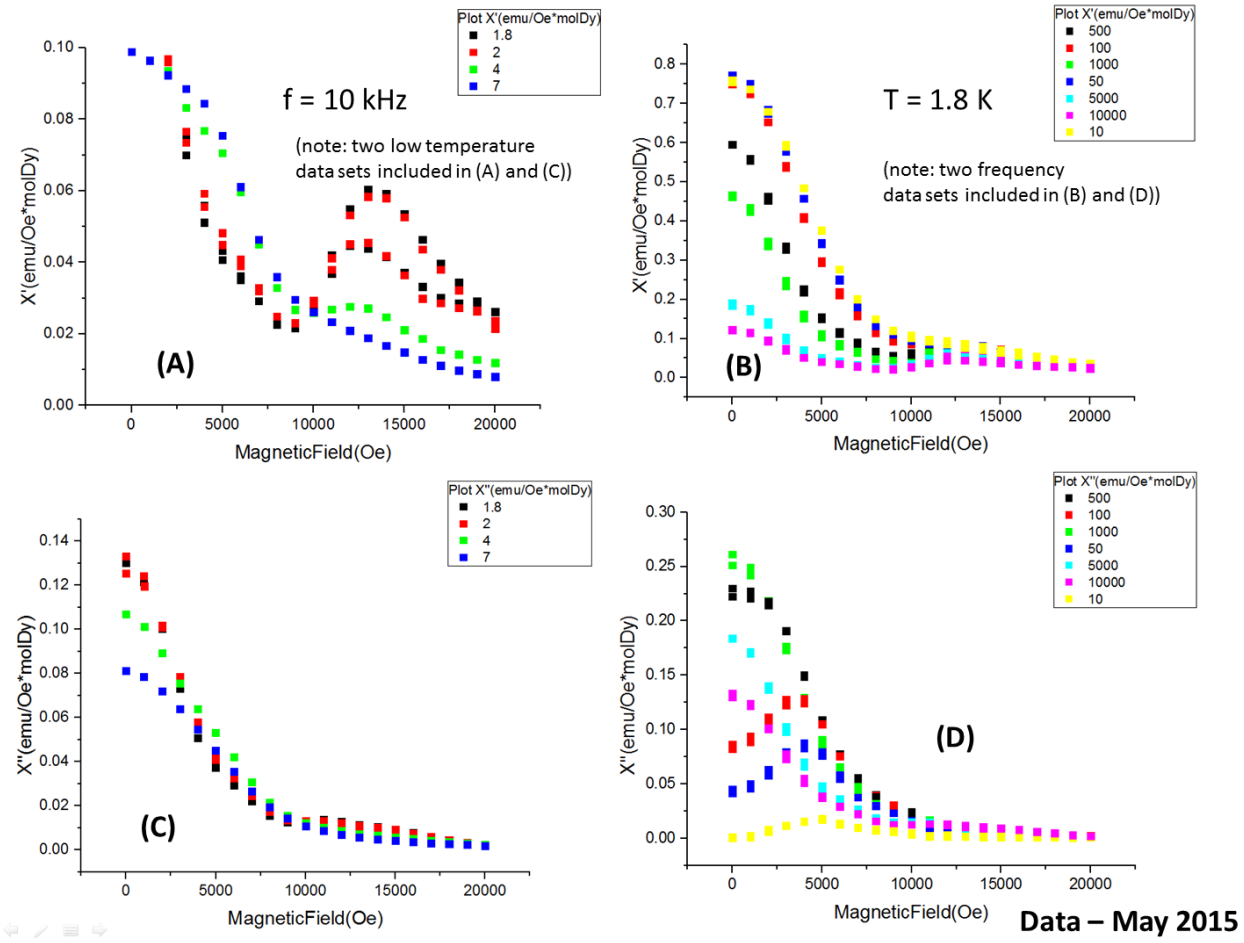

Figure A.5: Real (top) and imaginary (bottom) parts of the AC susceptibility are measured as a function of temperature (left) and frequency (right). Note the two inflection points in 1.8K and 2K in (A) which indicate the transitions from spin ice to kagome ice and then to a saturated ice state, which have been surpressed by 4K and 7K. In (D), note how increasing frequency curves peak near 1000 Hz, indicating a relaxation time consistent with other data. Compare [104].

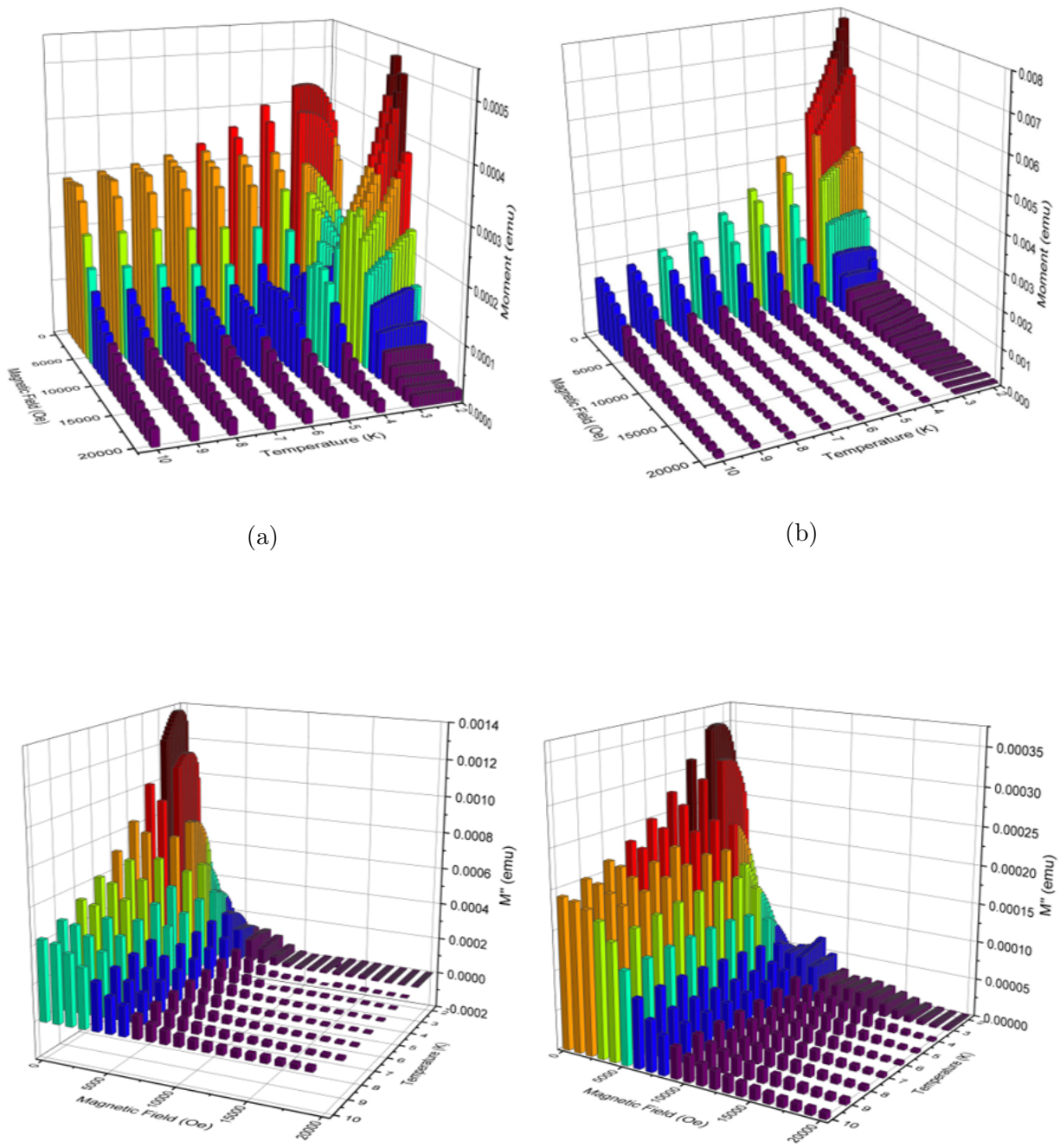

(a) (b)

(a) (b)

Figure A.7: Scans of the real and imaginary parts of the AC Susceptibility response at 10 kHz and 10 Oe excitation show the behavior of DTO change as temperatures and fields decrease. A large peak emerges in the top left for example as a sign of the transition between spin ice and kagome ice.

References

[1] P.W. Anderson. More is different. *Science*, 177(4047):393–396, 1972.

[2] Charles Kittel. *Introduction to Solid State Physics*. Wiley, 2004.

[3] Michael Tinkham. *Introduction to Superconductivity*. McGraw-Hill, 1995.

[4] Liang Fu and C.L. Kane. Superconducting proximity effect and majorana fermions at the surface of a topological insulator. *PRL*, 100(096407), 2008.

[5] ATLAS Collaboration. Search for heavy Majorana or Dirac neutrinos and right-handed W gauge bosons in final states with two charged leptons and two jets at $\sqrt{s} = 13$ TeV with the ATLAS detector. *JHEP*, 01(016), 2019.

[6] CMS Collaboration. Search for heavy Majorana neutrinos in e+/- e+/- plus jets and e+/- mu+/- plus jets events in proton-proton collisions at $\sqrt{(s)} = 8$ TeV. *JHEP*, 04(169), 2016.

[7] M. J. Harris, S. T. Bramwell, D. F. McMorrow, T. Zeiske, and K. W. Godfrey. Geometrical frustration in the ferromagnetic pyrochlore $Ho_2Ti_2O_7$. *PRL*, 79(2554), 1997.

[8] A.P. Ramirez et al. Zero-point entropy in spin ice. *Nature*, 399:333–335, 1999.

[9] C. Castelnovo, R Moessner, and S.L. Sondhi. Magnetic monopoles in spin ice. *Nature*, 451:42–45, 2008.

[10] G Sala et al. Vacancy defects and monopole dynamics in oxygen-deficient pyrochlores. *Nature Materials*, 13:488–493, 2014.

[11] J Snyder et al. How spin ice freezes. *Letters to Nature*, 413:48–51, 2001.

[12] M. J. Jackson, E. Lhotel, S. R. Giblin, S. T. Bramwell, D. Prabhakaran, K. Matsuhira, Z. Hiroi, Q. Yu, and C. Paulsen. Dynamic behavior of magnetic avalanches in the spin-ice compound $Dy_2Ti_2O_7$. *Phys. Rev. B*, 90(064427), 2014.

[13] R Siddharthan, BS Shastry, AP Ramirez, A Hayashi, RJ Cava, and S. Rosenkranz. Ising pyrochlore magnets: Low-temperature properties, ice rules, and beyond. *PRL*, 83:1854–57, 1999.

[14] S. T. Bramwell et al. Spin correlations in $Ho_2Ti_2O_7$ a dipolar spin ice system. *PRL*, 87(047205), 2001.

[15] C. Castelnovo, R. Moessner, and S.L. Sondhi. Spin ice, fractionalization, and topological order. *Annual Reviews of Condensed Matter Physics*, 3:33–55, 2012.

[16] Z. Hiroi, K. Matsuhira, S. Takagi, T. Tayama, and T. Sakakibara. Specific heat of kagom ice in the pyrochlore oxide $Dy_2Ti_2O_7$. *J. Phys. Soc. Japan*, 72(411), 2003.

[17] K Matsuhira, Z Hiroi, T Tayama, S Takagi, and T Sakakibara. A new macroscopically degenerate ground state in the spin ice compound dy2ti2o7 under a magnetic field. *Journal of Physics, Condensed Matter*, 14(29), 2002.

[18] ST Bramwell and MJP Gingras. Spin ice state in frustrated magnetic pyrochlore materials. *Science*, 294:1495–1501, 2001.

[19] M. J. P. Gingras and B. C. den Hertog. Origin of spin ice behavior in ising pyrochlore magnets with long range dipole interactions: an insight from mean-field theory. *Can. J. Phys.*, 79(1339), 2001.

[20] DJP Morris et al. Dirac strings and magnetic monopoles in the spin ice $Dy_2Ti_2O_7$. *Science*, 326(5951):411–414, 2009.

[21] B. Cabrera. First results from a superconductive detector for moving magnetic monopoles. *PRL*, 48(1378), 1982.

[22] MoEDAL Collaboration. Search for magnetic monopoles with the MoEDAL forward trapping detector in 2.11 $fb^{-}1$ of 13 TeV proton-proton collisions at the LHC. *Phys. Lett. B*, 782(510), 2018.

[23] Ville Pietila and Mikko Mottonen. Creation of Dirac Monopoles in Spinor Bose-Einstein Condensates. *PRL*, 103(030401), 2009.

[24] M. W. Ray, E. Ruokokoski, S. Kandel, M. Mttnen, and D. S. Hall. Observation of Dirac monopoles in a synthetic magnetic field. *Nature*, 505:657–660, 2014.

[25] H.M. Revell et al. Evidence of impurity and boundary effects on magnetic monopole dynamics in spin ice. *Nature Physics*, 9:34–37, 2013.

[26] Taoran Lin. *A study of the effect of perturbations in spin ice systems: site dilution, weak exchange, quantum and finite-size effects*. PhD thesis, Waterloo, 2014.

[27] Marianne Haroche and Claudio Castelnovo. Long-range Coulomb interactions and monopole population inversion following thermal quenches in spin ice. In *APS March Meeting*, volume L48.00001, 2017.

[28] D. Pomaranski, L. R. Yaraskavitch, S. Meng, K. A. Ross, H. M. L. Noad, H. A. Dabkowska, B. D. Gaulin, and J. B. Kycia. Absence of paulings residual entropy in thermally equilibrated $Dy_2Ti_2O_7$. *Nature Physics*, 9(353), 2013.

[29] SR Giblin. Pauling entropy, metastability and equilibrium in $Dy_2Ti_2O_7$ spin ice. *PRL*, 121(067202), 2018.

[30] M. Matthews. *Field Dependent Spin Dynamics in $Dy_2Ti_2O_7$*. PhD thesis, Penn State, 2011.

[31] R.F. Wang et al. Artificial spin ice in a geometrically frustrated lattice of nanoscale ferromagnetic islands. *Nature*, 439:303–306, 2006.

[32] K. Kimura et al. Quantum fluctuations in spin-ice-like $Pr_2Ti_2O_7$. *Nature Communications*, 4(1934), 2013.

[33] Jeffrey G. Rau and Michel J.P. Gingras. Frustrated quantum rare-earth pyrochlores. *Annual Review of Condensed Matter Physics*, 10:357–386, 2019.

[34] L. Bovo and others. Restoration of the third law in spin ice thin films. *Nat. Comm.*, 5:34–39, 2014.

[35] D.P. Leusink et al. Thin films of spin ice compound $Ho_2Ti_2O_7$. *APL Mat.*, 2(032101), 2014.

[36] K. Barry et al. Probing superexchange interactions in spin ice $Ho_2Ti_2O_7$ thin films. *arXiv*, 1805.06565, 2018.

[37] E.R. Kassner et al. Supercooled spin liquid state in the frustrated pyrochlore $Dy_2Ti_2O_7$. *PNAS*, 112(28):8549–8554, 2015.

[38] S.T. Bramwell et al. Measurement of the charge and current of magnetic monopoles in spin ice. *Nature*, 461:956–959, 2009.

[39] SR Dunsinger et al. Spin ice: magnetic excitations without monopole signatures using muon spin rotation. *PRL*, 107(207207), 2011.

[40] F. Kirschner et al. Proposal for the detection of magnetic monopoles in spin ice via nanoscale magnetometry. *PRB*, 97(140402), 2018.

[41] C Watson et al. Magnetic flux spectroscopy of classical spin ice $Ho_2Ti_2O_7$. In *APS March Meeting*, volume E24.00011, 2018.

[42] P. Dirac. Quantized singluarities in the electromagnetic field. *Proc. Royal Soc. of London*, 133(821):60–72, 1931.

[43] B M Wood, C A Sanchez, R G Green, and J O Liard. A summary of the Planck constant determinations using the NRC Kibble balance. *Metrologia*, 54(3), 2017.

[44] ER Williams, Ruby N Ghosh, and John M Martinis. Measuring the electon's charge and the fine structure constant by counting electrons on a capacitor. *J Res Natl Inst Stand Technol*, 97(2), 1992.

[45] Hiroaki Ishizuka and Yukitoshi Motome. Spontaneous spatial inversion symmetry breaking and spin Hall effect in a spin-ice double-exchange model. *PRB*, 88(100402), 2013.

[46] Etienne du Tremolet de Lacheisserie et al. *Magnetism: Fundamentals*. Springer, 2005.

[47] J Vannimenus and G Toulouse. Theory of the frustration effect. II. Ising spins on a square lattice. *Journal of Physics C*, 10(18), 1977.

[48] HT Diep. *MFrustrated Spin Systems*. World Scientific, 2013.

[49] R.A. Borzi et al. Intermediate magnetization state and competing orders in $Dy_2Ti_2O_7$ and $Ho_2Ti_2O_7$. *Nature Communications*, 7(12592), 2016.

[50] K. Karlova, J. Strecka, and T. Madaras. The schottky-type specific heat as an indicator of relative degeneracy between ground and first-excited states: the case study of regular ising polyhedra. *Physica B*, 488:49–56, 2016.

[51] S. Rosenkranz, A. P. Ramirez, A. Hayashi, R. J. Cava, R. Siddharthan, and B. S. Shastry. Crystal-field interaction in the pyrochlore magnet $Ho_2Ti_2O_7$. *J. Appl. Phys.*, 87(5914), 2000.

[52] Y. M. Jana, A. Sengupta, , and D. Ghosh. Estimation of single ion anisotropy in pyrochlore $Dy_2Ti_2O_7$, a geometrically frustrated system, using crystal field theory. *J. Magn. Magn. Mater.*, 248(7), 2003.

[53] J.S. Gardner, M.J.P. Gingras, and J.E. Green. Magnetic pyrochlore oxides. *Rev. Mod. Phys.*, 82(53), 2010.

[54] N. Martin et al. Disorder and quantum spin ice. *Phys. Rev. X*, 7(041028), 2017.

[55] D Bernal and RH Fowler. A theory of water and ionic solution, with particular refernce to hydrogen and hydroxyl ions. *J. Chem. Phys.*, 1(8), 1933.

[56] L. Pauling. The structure and entropy of ice and of other crystals with some randomness of atomic arrangement. *J. Am. Chem. Soc.*, 12(57), 1935.

[57] R.G. Melko, Byron C. den Hertog, and MJP Gingras. Long-range order at low temperatures in dipolar spin ice. *PRL*, 87(067203), 2001.

[58] P.W. Anderson. Ordering and antiferromagnetism in ferrites. *Phys. Rev.*, 102(1008), 1956.

[59] M. J. Harris, S. T. Bramwell, P. C. W. Holdsworth, and J. D. Champion. Liquid-gas critical behavior in a frustrated pyrochlore ferromagnet. *PRL*, 81(4496), 1998.

[60] H Aoki et al. Magnetocaloric effect study on the pyrochlore spin ice compound $Dy_2Ti_2O_7$ in a [111] magnetic field. *J. Phys. Soc. Japan*, 73:2851–56, 2004.

[61] Shun ichi Yoshida, Koji Nemoto, and Koh Wada. Ordered phase of dipolar spin ice under [110] magnetic field. *J. Phys. Soc. Jpn.*, 73:1619–1622, 2004.

[62] Sheng-Cheng Lin and Ying-Jer Kao. Half-magnetization plateau of a dipolar spin ice in a [100] field. *Phys. Rev. B*, 88(220402), 2013.

[63] Byron C. den Hertog and Michel J. P. Gingras. Dipolar interactions and origin of spin ice in ising pyrochlore magnets. *PRL*, 84(3430), 2000.

[64] C. Castelnovo, R. Moessner, and S.L. Sondhi. Debye-Huckel theory for spin ice at low temperature. *PRB*, 84(144435), 2011.

[65] S.T. Bramwell. Generalized longitudinal susceptibility for magnetic monopoles in spin ice. *Philo. Trans. Royal Soc. A*, 370(1981), 2012.

[66] S.R. Giblin. Creation and measurement of long-lived magnetic monopole currents in spin ice. *Nature Physics*, 7:252–258, 2011.

[67] S.J. Blundell. Monopoles, magnetricity, and the stray field from spin ice. *PRL*, 108(147601), 2012.

[68] M. Matthews et al. High-temperature onset of field-induced transitions in the spin-ice compound $Dy_2Ti_2O_7$. *PRB*, 86(214419), 2012.

[69] B. Klemke et al. Thermal relaxation and heat transport in the spin ice material $Dy_2Ti_2O_7$. *Journal of Low Temperature Physics*, 163(5-6):345–369, 2011.

[70] F. I. Lopez-Bara and F. Lopez-Aguilar. Two fluid model in low energy excited states within spin-ice systems. *Scientific Reports*, 8(16303), 2018.

[71] LDC Jaubert et al. Spin ice thin film: Surface ordering, emergent square ice, and strain effects. *PRL*, 118(207206), 2017.

[72] Etienne Lantagne-Hurtubise, Jeffrey G. Rau, and Michel J.P. Gingras. Spin-ice thin films: Large-N theory and Monte Carlo simulations. *Phys. Rev. X*, 8(021053), 2018.

[73] Q.J. Li et al. Single crystal growth of the pyrochlores $R_2Ti_2O_7$ (R=rare earth) by the optical floating-zone method. *Journal of Crystal Growth*, 377:96–100, 2013.

[74] S. V. Isakov, K. S. Raman, R. Moessner, and S. L. Sondhi. Magnetization curve of spin ice in a [111] magnetic field. *Phys. Rev. B*, 70(104418), 2004.

[75] L. Bovo et al. Brownian motion and quantum dynamics of magnetic monopoles in spin ice. *Nature Communications*, 4(1535), 2013.

[76] Jens Jenson. *Rare Earth Magnetism: Structures and Excitations, Chapter 3*. Clarendon Press, 1991.

[77] John Clarke and Alex Braginski. *The SQUID Handbook*. Wiley, 2005.

[78] Christopher Nugroho. *Low Frequency Critical Current Noise and Two Level System Defects in Josephson Junctions*. PhD thesis, UIUC, 2015.

[79] Roger H. Koch, David P. DiVincenzo, and John Clarke. Model for 1/f flux noise in SQUIDs and qubits. *PRL*, 98(267003), 2007.

[80] Simon J. Bending. Local magnetic probes of superconductors. *Advances in Physics*, 48:449–535, 1999.

[81] J. Snyder, J. S. Slusky, R. J. Cava, and P. Schiffer. Dirty spin ice: The effect of dilution on spin freezing in $Dy_2Ti_2O_7$. *PRB*, 66(064432), 2002.

[82] J. Snyder, B. G. Ueland, J. S. Slusky, H. Karunadasa, R. J. Cava, and P. Schiffer. Low-temperature spin freezing in the $Dy_2Ti_2O_7$ spin ice. *PRB*, 69(064414), 2004.

[83] Hu Dong Lee, D.A. Rudman, and J.C Garland. Observation of a new thermoelectric effect in superconducting thin films. *PRL*, 55(19), 1985.

[84] J.C. Garland and D.J. Van Harlingen. Theory of vortex interaction with thermoelectric fields in a thin-film superconductor. *PRL*, 55(19), 1985.

[85] B. Tomasello et al. Correlated quantum tunnelling of monopoles in spin ice. *arXiv*, 1810.11469, 2018.

[86] G. Kolland et al. Thermal conductivity and specific heat of the spin-ice compound $Dy_2Ti_2O_7$: Experimental evidence for monopole heat transport. *PRB*, 86(060402), 2012.

[87] SM Anton et al. Magnetic flux noise in dc SQUIDs: Temperature and geometry dependence. *PRL*, 110(147002), 2013.

[88] X. Ke et al. Spin-ice behavior in $Dy_2Sn_2xSb_xO_7 + x2$ and Dy_2NbScO_7. *PRB*, 76(214413), 2007.

[89] P. Henelius et al. Refrustration and competing orders in the prototypical $Dy_2Ti_2O_7$ spin ice material. *PRB*, 93(024402), 2016.

[90] J. Baere et al. Ac susceptibility measurements of the spin-ice materials $Dy_2Ti_2O_7$ and $Ho_2Ti_2O_7$: Measuring magnetic monopole transport. In *APS March Meeting*, volume E24.00006, 2018.

[91] J.A. Quilliam et al. Dynamics of the magnetic susceptibility deep in the coulomb phase of the dipolar spin ice material $Ho_2Ti_2O_7$. *PRB*, 83(094424), 2011.

[92] R. G. Melko and M. J. P. Gingras. Monte carlo studies of the dipolar spin ice model. *J. Phys. Condensed Matter*, 16(R1277), 2004.

[93] T. Fennell et al. Neutron scattering investigation of the spin ice state in dy2ti2o7. *PRB*, 70(134408), 2004.

[94] S. Mostame et al. Tunable nonequilibrium dynamics of field quenches in spin ice. *PNAS*, 111(2):640–645, 2014.

[95] C. Paulsen et al. Far-from-equilibrium monopole dynamics in spin ice. *Nature Physics*, 10:135–139, 2014.

[96] L. Savary and L. Balents. Disorder-induced quantum spin liquid in spin ice pyrochlores. *PRL*, 118(087203), 2017.

[97] P. A. McClarty, O. Sikora, R. Moessner, K. Penc, F. Pollmann, and N. Shannon. Chain-based order and quantum spin liquids in dipolar spin ice. *PRB*, 92(094418), 2015.

[98] J.-J. Wen et al. Disordered route to the coulomb quantum spin liquid: Random transverse fields on spin ice in $Pr_2Zr_2O_7$. *PRL*, 118(107206), 2017.

[99] Jian-Huang She, Choong H. Kim, Craig J. Fennie, Michael J. Lawler, and Eun-Ah Kim. Topological superconductivity in metal/quantum-spin-ice heterostructures. *npj Quantum Materials*, 2(64), 2017.

[100] Sho Nakosai and Shigeki Onoda. Magnetic monopole supercurrent through a quantum spin ice tunnel junction. *arXiv*, 1801.03117, 2018.

[101] D.I. Khomskii. Electric dipoles on magnetic monopoles in spin ice. *Nature Communications*, 3(904), 2012.

[102] L. D. C. Jaubert and R. Moessner. Multiferroicity in spin ice: Towards magnetic crystallography of $Tb_2Ti_2O_7$ in a field. *PRB*, 91(214422), 2015.

[103] Y.L. Xie, L. Lin, Z.B. Yan, and J.-M. Liu. Magnetic phase transitions and monopole excitations in spin ice under uniaxial pressure: A monte carlo simulation. *J Appl Phys*, 117(17), 2015.

[104] K. Matsuhira, Y. Hinatsu, and T. Sakakibara. Novel dynamical magnetic properties in the spin ice compound $Dy_2Ti_2O_7$. *J. Phys. Condensed Matter*, 13(L737), 2001.